UNIVERSITÀ
DEGLI STUDI
DI PADOVA

Sede Amministrativa: Università degli Studi di Padova
Sede Consorziata: Istituto Superiore di Sanità

Dipartimento di: Tecnologia e Salute

SCUOLA DI DOTTORATO DI RICERCA IN : Scienze tecnologie e misure spaziali
INDIRIZZO: Misure meccaniche per l'ingegneria e lo spazio (MMIS)
CICLO XXV

Fluid dynamics characterization of biomedical implantable devices: experimental measurements and numerical simulation

Direttore della Scuola : Ch.mo Prof. Giampiero Naletto
Coordinatore d'indirizzo: Ch.mo Prof. Stefano Debei
Supervisore : Ch.mo Prof. Mauro Grigioni
Co-Supervisore : Ch.mo Prof. Paolo Castellini

Dottorando : Guanglei Wang

Abstract

Mechanical heart valves, specifically bileaflet valves, are widely applied to take place of diseased native valves. These prosthetic valve replacements exhibit good long-term mechanical durability. However, mechanical loading of blood is associated to complications (hemolysis and thrombogenicity), which represent important safety requirements for this kind of valves.

In this thesis work, Particle Image Velocimetry (PIV) was applied as experimental tool for evaluating fluid dynamics characterization of biomedical implantable devices, especially for bileaflet mechanical heart valves (BMHVs). The procedures of PIV measurement of same target were repeatedly executed for multiple experimental validations of numerical data. The reproducibility of experimental data from PIV multiple measurements was proved reliable with the coefficients of variation for hemodynamic properties below 5%. These hemodynamic parameters such as velocity, turbulence shear stress (TSS) and hemolysis index (HI) did not only supply a good research basis for numerical simulation, but also directly analyze the potential risks for blood damages due to the artificial implantations. The maximum TSS captured in leakage jets of valve type 1 was around 40 Pa and that of valve type 2 was 20 Pa.

The simulations using computational fluid dynamics (CFD) were carried out based on the physical parameters of experimental conditions. Good agreements between PIV and CFD were observed according to the comparisons in near-hinge regions. Furthermore, CFD data were used to investigate the hemodynamic properties inside of hinge region, where PIV measurements cannot be carried out due to optical inaccessibility. The experimental work was carried out entirely at the Istituto Superiore di Sanità (ISS) in Rome, Italy, whereas the simulation work was based on the cooperation between ISS and the Technical University of Cluj-Napoca (TuCN) in Cluj-Napoca, Romania.

The final object of our cooperation is to take use of experimental and simulation methodologies to define a standard procedure for obtaining sufficient reliability in risk evaluation and mitigation of prosthetic heart valves.

Astratto

Le valvole cardiache di tipo meccanico, in particolare le valvole a doppia flangia (bileaflet), sono largamente applicate nella sostituzione di valvole native affette da diverse patologie. Queste protesi valvolari presentano una buona durata a lungo termine. Tuttavia, le sollecitazioni meccaniche a carico del sangue sono associate a complicanze (emolisi e trombogenicità), che pongono importanti requisiti di sicurezza per questo tipo di valvole.

In questo lavoro di tesi, la Particle Image Velocimetry (PIV) è stata applicata come strumento sperimentale per la caratterizzazione fluidodinamica dei dispositivi biomedici impiantabili, in particolare per le valvole cardiache meccaniche a doppia flangia (BMHV). Misure PIV della stessa posizione nel campo fluidodinamico sono state eseguite ripetutamente, per ottenere affidabili convalide sperimentali di dati numerici. La riproducibilità dei dati sperimentali da misure PIV è stata dimostrata affidabile, con un coefficiente di variazione per le proprietà emodinamiche inferiore al 5%. Questi parametri emodinamici come la velocità, turbulence shear stress (TSS) e indice di emolisi (HI) non hanno solo fornito una buona base di ricerca per la simulazione numerica, ma hanno anche consentito di analizzare direttamente i potenziali rischi per il danno ematico causato dell'impianto di dispositivo. Il massimo TSS misurato per i getti di rigurgito della valvola di tipo 1 è stato di circa 40 Pa e per I getti di rigurgito della valvola di tipo 2 è stato di 20 Pa.

Le simulazioni che utilizzano la fluidodinamica computazionale (CFD) sono state eseguite in base ai parametri fisici delle condizioni sperimentali. E' stato osservato un buon accordo tra risultati PIV e CFD, in base al confronto nella regione vicina alla cerniera della flange. Inoltre, i dati CFD sono stati utilizzati per studiare le proprietà emodinamiche all'interno della regione della cerniera, in cui le misure PIV non possono essere effettuate a causa dell'inaccessibilità ottica. Il lavoro sperimentale è stato condotto interamente presso l'Istituto Superiore di Sanità (ISS), Roma, mentre e gli studi di simulazione si basano sulla collaborazione tra l'ISS e l'Università Tecnica di Cluj-Napoca (TuCN) a Cluj-Napoca, Romania.

Lo scopo finale di tale collaborazione è quello di usare metodologie sperimentali e di simulazione per definire una procedura standard per ottenere una sufficiente affidabilità per la

valutazione e la mitigazione del rischio associato all'impianto di protesi valvolari cardiache.

Acknowledgements

Firstly, I would like to express my deepest thank and gratitude to my supervisor Mauro Grigioni, for being a strong source of motivation, guidance and patience during this thesis work. And my second supervisor Giuseppe D'Avenio, thank you for your many guides and help during my stay at Istituto Superiore di Sanità (ISS). I acknowledge and thank my co-supervisor Prof. Paolo Castellini for his support.

I am grateful to my colleagues in Biomedical Engineering Group in Technical University of Cluj-Napoca (TuCN), Romania. Professor Dan Rafiroiu, many thanks for helpful discussions and for providing me some simulations data used for validation with my experiment work. Other members of TuCN whom I would like to acknowledge include: Yan Li, Rajeev K. Nallamothu1 and Calin Neamtu.

Last but not least, highly appreciation to MeDDiCA (Medical Devices Design in Cardiovascular Applications) which has received funding from the European Union Seventh Framework Programme (FP7/2007-2013) under grant agreement n° 238113 to give me financial support.

A special thank goes to my wife Yan Li for contributing and sharing her knowledge, giving priceless advice for this thesis and moral supports. Without her support, it's impossible for me to finish the work.

Simple words can never express how much we owe to the people that have helped me. Best we could offer is an acknowledgement of their support during the course of the thesis. Thank you.

Contents

List of Tables

List of Figures

Chapter 1
Background and State-of-the-art

1.1 INTRODUCTION

Prosthetic heart valves are widely used to replace disease heart valves throughout the world and the most commonly implanted prosthetic valve design is bileaflet mechanical heart valves (BMHVs) owing to their good long-term durability and superior bulk flow properties. However, despite their widespread applications, the implantation of BMHVs is still not complication-free and may introduce potential damage for blood components such as hemolysis, platelet activation and thromboembolic events. All currently implanted mechanical valves generate significantly different flow patterns from those presenting in normal cardiovascular system. Typically, these flow patterns include regions of high velocity and high shear that are potentially damaging to blood elements, as well as recirculation regions with long flow residence times where clot formation may occur. Clinical reports acknowledge that these complications are associated with the fluid stressed imposed by non-physiologic nature of the flow induce by the valve, particularly in its hinge recess and near hinge region. In this section, we present a brief overview of past experimental methodologies aimed at elucidating the hemodynamics of prosthetic valves. This chapter is organized as three parts: firstly the links between hemodymics and clinical complications will be described by previous studies; secondly the experimental techniques will be reviewed chronically including:

(1) previous experimental investigations based on Laser Doppler Anemometer (LDA) technology; (2) previous study of flow visualizations for hemodynamics of BMHVs based on Particle Image Velocimetry (PIV) technology; and (3) other methodologies for fluid dynamics study of BMHVs.

At the end of this chapter, the aim of this thesis will be described.

1.2 THE LINKS BETWEEN HEMODYNAMICS AND CLINICAL COMPLICATIONS

Artificial organs, such as pumps, tubing and valves, started to be reported associated with blood degradation since the 1950's. Until the mid-1960's, more scientific attitudes changed to focus on the mechanisms responsible for blood trauma rather than the mere reporting of the

amount of trauma produced by particular devices or procedures [1].

Although a successful clinical practice, valve replacement is still not free from complications. Thromboembolic events and hemolysis are the major clinical problems that can occur, upon prosthesis valve implantation [2]. In this section, the previous studies concerning in these two clinical complications are reviewed.

1.2.1 HEMOLYSIS AND DAMAGE FOR RED BLOOD CELLS (RBCS)

Hemolysis is the rupturing of red blood cells and results in the release of hemoglobin in the blood stream. Red blood cells have the function to carry oxygen throughout the body and have a typical lifespan of about 120 days, the replacements of which are necessary at the average rate of 2 to 3 million cells per second. The short lifespan is due to the absence of the normal intracellular organelles such as the nucleus and mitochondria [3]. As cells age, results of cumulative or instantaneous damage could make the nonreparable lipid bilayer membrane become fragile. When the membrane is stretched, the cells have the inclination to rupturing. This often occurs naturally when the cells are squeezing through tight passages in the microcirculation, especially those in the spleen. Non-physiologic nature of the flow induced by implanted devices impose high shear stress in some regions, where are high risks region for hemolysis. Fig. 1.1 (a) shows normal RBCs and fig.1 (b) shows RBCs under hemolysis condition.

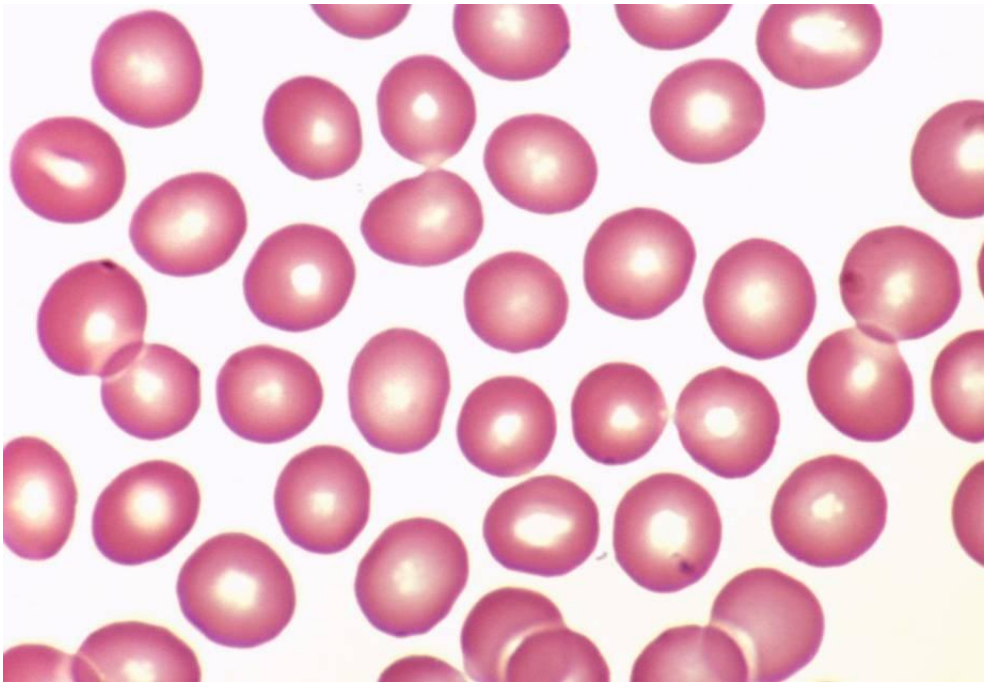

(a)

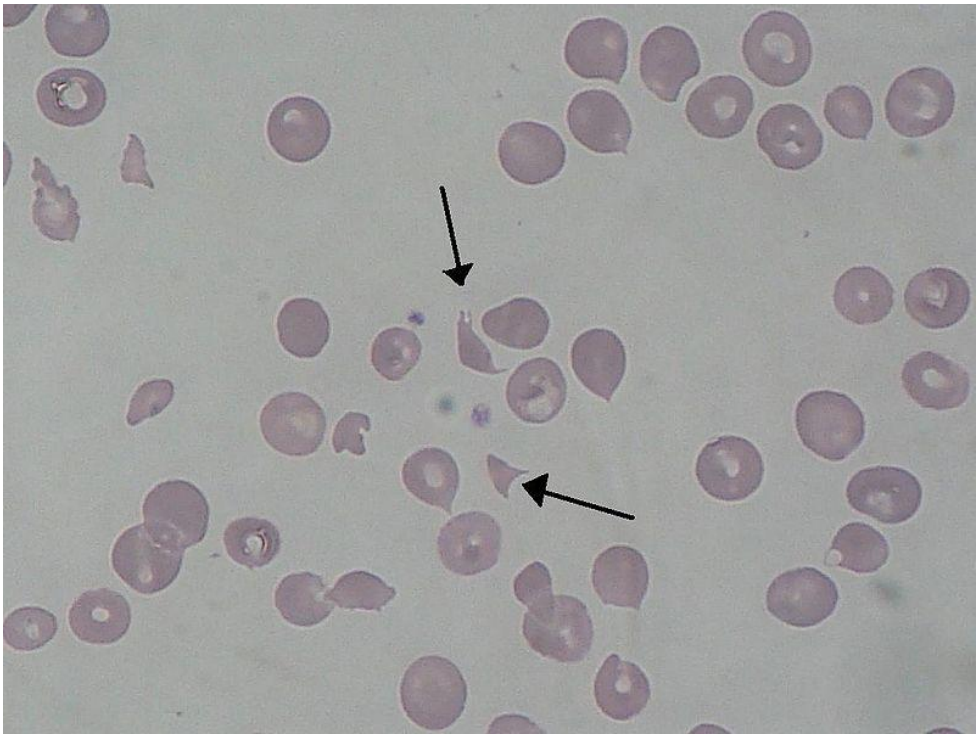

(b)

Figure 1.1: (a) normal RBCs (by Kristine Krafts, M.D, 2009); (b) Hemolysis (by Kenar D. J., 2011)

Significant hemolysis was firstly observed in certain patients who had artificial valves or other cardiovascular prostheses by Marsh in 1964 [4] and Sayed et al. in 1961 [5]. As early as 1970, Bacher et al. [6], Leverett et al. [7], Rooney [8] and Williams et al. [9] started to investigate the effect of shear stress on RBCs applying a number of devices including concentric-cylinder viscometers, capillary tubes, cone-and-plate viscometers, Couette cells, liquid jets, ultrasonically pulsating gas bubbles, and oscillating wires. Leverett et al. [7] show the results that there is a threshold shear stress, 1500 $dynes/cm^2$, above which extensive cell damage is directly due to shear stress, and the various secondary effects listed above are negligible. At the high stress regime, very high rates of hemolysis occur and RBCs damage could be attributed directly to shear stress and exposure time rather than solid surface interaction. Sutera et al. [10] reported similar studies and observations in 1975. They increased the shear stress gradually in range from 100 to 2500 $dynes/cm^2$ and observed that the deformed RBCs evolve toward a smooth ellipsoidal shape. Furthermore, the conclusion was given that fragmentation of the RBCs occurs at stresses above 2500 $dynes/cm^2$ with an increasing concentration of free hemoglobin in suspending fluid. In 1984, Sallam and Hwang investigated the effect of turbulent shear stress on RBC hemolysis with a laser Doppler anemometer and quantified the threshold lever for incipient hemolysis to be about 4000 $dynes/cm^2$ [11]. In 1999, Grigioni et al. [12] proposed a discussion based on the experiments of Sallam and Hwang. They reported that the threshold value of 4000 $dynes/cm^2$ could be considerably underestimated. With a suitable orientation of

the measurement axes, at least 6000 $dynes/cm^2$ should be the peak turbulent shear stress at the inception of hemolysis with a 3-D stress analysis. In 2001, Lu et al. confirmed that the threshold of 4000 $dynes/cm^2$ was underestimated without calculating from the major principal turbulent shear stress [13].

In 1986, Conti et al. identified 29 patients with the Beall 103 and 104 disc valves implanted after 4 to 10 years surgery to determine degree of hemolysis by cinefluoroscopy and echocardiography [14]. The observations over a mean of 2.8 years in patients with an isolated Beall valve showed increasing hemolysis frequently concomitant with onset of cardiac symptoms. In 1993, Skoularigis et al. evaluated hemolysis in 170 patients with St. Jude Medical (SJM) and 80 patients with Medtronic Hall (MH) prostheses, with normal mechanical function [15]. They reported that elevated concentrations of plasma lactate dehydrogenase (LDH), serum haptoglobin, blood hemoglobin and reticulocyte levels are due to the presence and severity of hemolysis and patients with SJM prostheses have greater frequency and severity than patients with MH prostheses. In 1996, Garcia et al. tried to define the hydrodynamic mechanisms involved in the occurrence of hemolysis in prosthetic mitral valve regurgitant utilizing transesophageal echocardiography and fluid dynamic simulation [16]. They evaluated 27 patients with reoperation for significant mitral prosthetic regurgitant and gave the conclusions that fast acceleration and deceleration or high peak shear stress are contributed to the distinct flow patterns produced by the prosthesis regurgitant lesion, the nature of which is more important than the site of origin of the flow pattern in producing clinical hemolysis. To analyze the severity of hemolysis of mechanical prosthesis and bioprosthesis, Mecozzi et al. [17] in 2002 summarized clinical conditions (such as serum lactic dehydrogenase) from 172 patients with mechanical implantations and 106 patients with bio-implantations in aortic position, mitral position, or both. They emphasized that subclinical hemolysis frequently occurs in normally functioning prosthetic heart valves and a high incidence of hemolysis is found in mechanical prosthesis. In 2004, hemolysis parameters of St. Jude valves in aortic position were analyzed by Suedkamp et al. [18]. They tested plasma lactate dehydrogenase (LDH) concentration in 102 patients with prostheses valve replacement to reflect hemolysis due to mechanical heart valve dysfunction. The conclusion was given that LDH values >400U/l indicate valvular dysfunction or leakage if non-cardiac caused for hemolysis are excluded in aortic position.

1.2.2 THROMBOEMBOLIC EVENTS AND PLATELET ACTIVATION

The platelets are the essential components and the smallest cells in human blood, being only fragments of megakaryocyte cytoplasm, with normal count in the range $150-350\times10^9.l^{-1}$ [19].

The life span of the platelet is approximately 8-10 days [20]. The platelets in rest are discoid and have a smooth, rippled surface [21] with diameter with averages 1-2 μm and a mean cell volume of around 5-6 fl [22]. The producing process of platelets is controlled by agents such as thrombopoietin [23]. Platelets are highly sensitive cells, which may aggregate, release their contents into the surrounding medium and even easily adhere to the surface of non-biological devices.

The activation of platelets is induced by the interaction of several agonists with receptors expressed on the platelet membrane. Platelet activation is a series of cascading responses which allow blood platelets to react to an injury. However, the over-activity of platelets plays a central role in the process of thrombus formation (thrombogenesis) [24] and the progression of atherosclerotic lesions [25]. This risk of platelet over-activity may be viewed as the result of an imbalance in the homeostatic system, due, in large part, to chronic blood damage and the destruction of formed blood elements [26].

Thrombus (blood clot) can be a very serious issue. This is because the clotted blood can block the flow of blood through the affected vessel. When blood flow is blocked, oxygen cannot flow to tissues that need it and a condition called *ischemia* can result. Without quick medical attention, these tissues can suffer irreparable damage and even die. Fig 1.2 shows the aggregation of platelets and thrombus in anatomical condition.

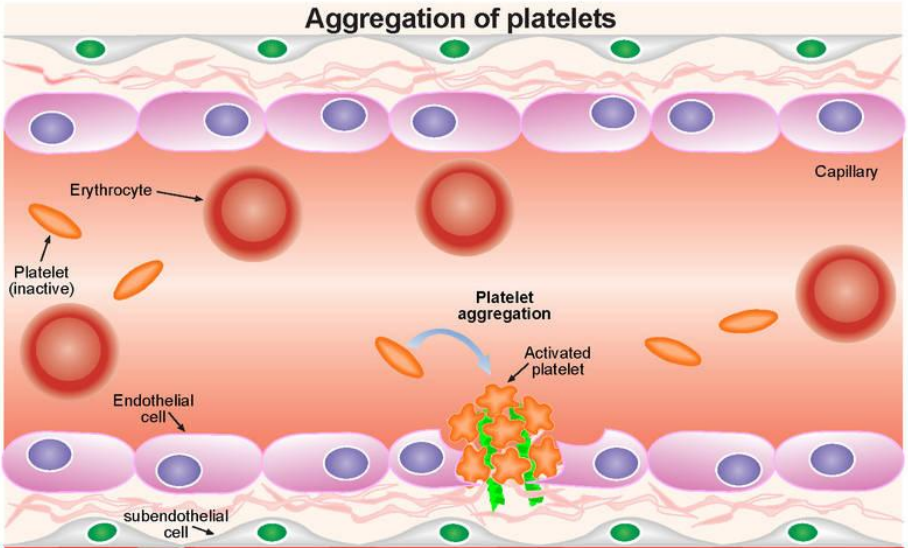

(a)

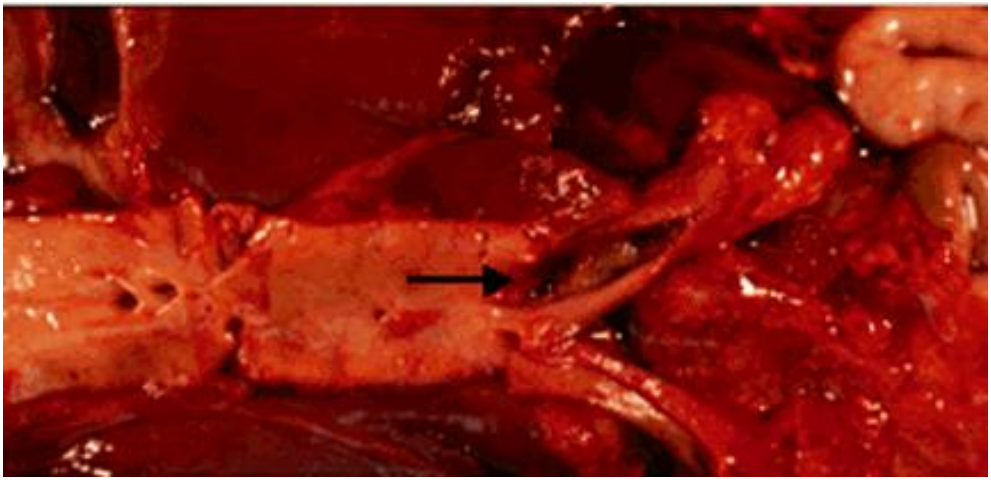

(b)

Figure 1.2: (a) platelet aggregation (by immunopaedia.org); (b) thrombus (by University of Connecticut Health Center)

In 1970, Harker and Slichter tested the first-generation mechanical valves such as the ball-and-cage and tilting-disc concerning in the aspect of platelet damage and found that patients had a shorten platelet half-life due to increased incidence of platelet destruction and activation [27]. The platelet destruction is due to two possible mechanical accountings: shearing stress and direct mechanical trauma induced by the valve structure. In 1975, Steele et al. analyzed platelets survival time following aortic valve replace [28]. They studied in 73 patients with aortic valve disease and proved a correlation between occurrence of thromboembolism after aortic valve replacement and shortened platelet survival time. A series of 76 mitral valve replacements with the Beall valves was reported by Salomom et al. [29] with 5.2% thromboembolism occurrence. In 1976, Dale evaluated arterial thromboembolic complications in 253 patients, who had a single aortic Starr-Edwards ball valve implanted [30]. In spite of intense anticoagulant therapy, arterial thromboembolic complications represent a key threat to patients with aortic ball valves even several years after operation. In 1977, Jon Dale et al. studied arterial thrombembolic complications in 196 patients with Björk-Shiley or Lillehei-Kaster aortic disc valve implanted and reported that thrombotic valve malfunction is particularly serious for aortic disc vale implantation, which may even limit the movements of the discs [31]. In 1981, Pumphrey et al. demonstrated that patients with mechanical valve replacements had the elevation of the plasma β-thromboglobulin (β-TG) concentration, which reflected platelet aggregation in vivo [32]. In 1987, Czer et al. followed 527 patients with St. Jude prostheses implanted up to 8 years from 1978-1986 and the valve thrombosis occurred in 0.4%/patient-year [33]. In 2011, Bourguignon et al. evaluated risk factors for valve-related complications after mechanical heart valve replacement in 505 patients with long-term follow

up and concluded that thromboembolic and bleeding complications perform the main causes for valve-related events or the need for repeat surgery [34].

In 1975, Brown et al. gradually increased shears lever to define the different physical effects to the activations of platelets [35]. Subsequent platelet aggregation was resulted by very low shear stress (50 $dynes/cm^2$). When stress up to 100 $dynes/cm^2$, the appearance in plasma of non-storage nucleotides indicate cell lysis. The fragmentation of platelets was observed at shear stresses of 250 $dynes/cm^2$. In 1977, Bernstein et al. applied the electron microscope to study human platelets injury and they found out that the shear injured platelets demonstrate substantial number of structural changes at shear level up to 10 $dynes/cm^2$ [36]. Apparently normal platelet aggregation could be observed with both functional and structural injury at higher shears. In 1978, Anderson et al. used a rotational viscometer to investigate the effects of shear stress on platelets in human platelet-rich plasma [37]. They reported two threshold level of shear stress for platelet lysis 160 $dynes/cm^2$ and 600 $dynes/cm^2$ corresponding to the exposure time 5-min and 30-s separately. The conclusion was given that platelets are much more sensitive to shear tress than RBCs for relatively long exposure times. In 1979, Ramstack et al. analyzed shear-induced activation of platelets [38]. They exposed platelet-rich plasma under the conditions of 300, 750 and 1000 $dynes/cm^2$ bulk-average shear stresses with the average residence times ranging 25 to 1650 ms and reported that these shears for these residence times did not induce cell lysis, but did activate the platelets. In 1986, Moake et al. modeled platelet-surface interactions with the information derived from other laboratories and determined that platelet aggregation is mainly attributed to an artifact of cell lysis at shear stresses below 12 $dynes/cm^2$, however, at shear stresses greater than 10 to 12 $dynes/cm^2$, platelet aggregation depends on the presence of plasma vWF and functional platelet receptor complexes GpIb/IX/V and GpIIb-IIIa [39].

1.2.3 COMPARISON OF SHEAR STRESS EFFECTS ON RBCS AND ON PLATELETS

Previous literatures demonstrated that shear stress has different mechanical effects on the RBCs and platelets. RBCs have much more resistance to mechanical damage, and experience less shear forces than platelets. The observations from Travis et al. [40] proved this judgment. Activation of platelets may only require the level of shear stresses one order of magnitude less than that for hemolysis occurrence. Because of smaller size of platelets, turbulence shear stress induced by leakage jets during regurgitant phase may cause direct threat to them. However, it seems to be reverse at very short exposure time that platelets are observed to be more

resistant at same level of shear stress than RBCs. Another difference reaction between RBCs and platelets is that the erythrocytes have the deformability properties, which platelet do not have because of different structures. The lack of these properties may increase the susceptibility of platelets to shear stress induced modifications. The research of Brown et al. [41] proved this point by demonstrating the significance of the leakage of ADP from sheared platelets compared to the leakage of hemoglobin from RBCs.

1.3 STATE-OF-THE-ART FOR EXPERIMENTAL WORKS

1.3.1 LASER DOPPLER ANEMOMETRY (LDA)

In 1975, Brown et al. [41] performed one of the first experiments to test a relationship between thrombus formation and a known shear stress. They found that platelets exposed to shear stresses in excess of 50 $\mathrm{dyne/cm^2}$ releases a significantly greater amount of the agonist ADP and tend to aggregate faster than platelets exposed to lower shear stresses. This showed that shear stress could induce platelet aggregation. Similar studies and observations were reported by Sallam and Hwang [11], Bluestein et al. [42], and Wurzinger et al [43].

In 1979, Yoganathan et al. started to measure in vitro velocity in the vicinity of aortic prostheses [44]. They reported that the experimentally observed wall-shear stresses could damage RBCs and platelets and lead to thrombus formation.

In 1984, Chandran et al. used qualitative flow visualization and quantitative laser-Doppler techniques to study pulsatile flow in a human aorta model with tissue valve prostheses [45]. Their works showed that the velocity profiles with pericardial valves are comparable to those measured natural aortic valves and the porcine valves produced a stronger jet with relatively larger turbulent stresses in the boundary of the jet due to a small valve opening area. In 1985, Chandran et al. continue their research works to define pulsatile flow patterns past a caged ball valve [46] and tilting disc valves [47] in a model human aorta with LDA.

In 1986, Yoganathan et al. evaluated the turbulent shear fields in the immediate downstream vicinity of both of mechanical and bioprosthetic and reported that all the aortic valves studied (mechanical and tissue) can cause sub-lethal and/or lethal damage to blood elements with the levels of turbulent shear stress [48]. They reported their work about using 2D LDV to conduct the first detailed investigations of the pulsatile forward flow fields of the SJM bileaflet valve in the aortic position and the Medtronic-Hall and Bjork–Shiley tilting-disc valves. They reported maximum turbulent shear stresses down- stream of the leaflets ranging from 1200 $\mathrm{dyne/cm^2}$ for the SJM valve to 2000 $\mathrm{dyne/cm^2}$ for the Medtronic-Hall valve.

In 1989, Hanle et al. used laser Doppler anemometry to examine the velocity fields downstream of four prosthetic heart valves (The Björk-Shiley 60° convexo-concave tilting disc valve, the Smeloff-Cutter caged ball valve, the St. Jude Medical bileaflet valve, and the Ionescu-Shiley standard bioprosthesis) under steady and pulsatile conditions [49]. Velocity profiles under steady flow had a good agreement with pulsatile profiles only during mid systole and variations in large scale flow structures of four valves were observed under pulsatile flow.

In 1991, Schoephoerster et al. did the experiments to measure velocity and turbulent shear stress past caged-ball, tilting disc, bileaflet, and polyurethane tri-leaflet mitral valves using LDA in vitro and gave the conclusions that turbulent shear stress magnitudes for all four valves did not exceed the threshold level for hemolytic damage, but did exceed that for platelet lysis [50].

In 1994, Nygaard et al. evaluated the spatial distribution and temporal development of turbulent shear stress downstream of three mechanical aortic valve prostheses including the St. Jude Medical, the CarboMedics and the Starr-Edwards silicone rubber ball [51]. The highest levers of turbulent shear stress for three mechanical prosthesis valves are 270 to 630 $\mathrm{dyne/cm^2}$ (the St. Jude valves), 190 to 720 $\mathrm{dyne/cm^2}$ (the CarboMedics valves) and 110 to 560 $\mathrm{dyne/cm^2}$ (the Starr-Edwards silicone rubber ball valves). They compared these two kinds of mechanical heart valves and emphasized that a flow reversal along the entire cross-section is observed in early diastole for the disc valves, which do not occur in caged ball valves.

In 1997, Maymir et al. applied a 2 component LDA system to study the effects of tilting disk hear t valve gap width on regurgitant flow through an artificial heart mitral valve [52]. They revealed that the minor orifice tends to generate stronger leakage jets during regurgitant flow than the major orifice and the hemolytic potential induced by the mitral valve decreases as the gap width increases. Similar research and conclusion were reported in 1998 by Travis et al. [53].

Using LDA techniques, Ellis et al. (2000) [54] investigated the hinge and near-field forward flow regions of the Regent™ valve. During forward flow, a recirculation region developed in the inflow pocket of the Regent™ hinge but was subsequently abolished by strong backflow during valve closure. Leakage velocities in the hinge region reached 0.72 m/s and Reynolds shear stresses reached 2,600dyn/cm2. Velocities in the near-field region were highest in the lateral orifice jet, reaching 2.1m/s. At same year, Eillis et al. published the results to evaluate the hinge-flow dynamics of two new variations of a 17-mm St Jude Medical bileaflet valve: the Hemodynamic Plus and the Regent (St Jude Medical, Inc, St Paul,Minn) [55]. During systole, velocities through the hinge pocket reached 0.70 m/s, and the turbulent shear stress reached 1000 $\mathrm{dyne/cm^2}$. In the thumbnail, forward flow velocities ranged from 1.4 m/s to 1.7 m/s. In

the 17-mm Regent hinge, velocities through the hinge pocket reached 0.75 m/s, and the turbulent shear stress reached 1300 $\mathrm{dyne/cm^2}$. In the thumbnail, forward flow velocities ranged from 1.0 m/s to 1.3 m/s.

In 2002, Hwa-Liang Leo et al. [56] used LDA to evaluate the hinge flow dynamics of a 23-mm Carbomedics bileaflet mechanical valve (Sulzer CarboMedics Inc, Austin, Tex). They obtained the phase-averaged forward velocity at the flat level and levels of 190 μm and 390 μm above flat level and 1 mm below flat level were 0.54 m/s, 0.77 m/s, 0.3 m/s, and 1.0 m/s, respectively. Corresponding values of the peak phase-averaged leakage velocities were 3.17 m/s, 2.91 m/s, 2.52 m/s, and 0.5 m/s, respectively. Corresponding turbulent shear stresses were 5510 $\mathrm{dyne/cm^2}$, 5640 $\mathrm{dyne/cm^2}$, 4380 $\mathrm{dyne/cm^2}$, and 4810 $\mathrm{dyne/cm^2}$, respectively.

In 2004, Simon et al. [57] compared the hinge flow fields of two bileaflet mechanical heart valves under aortic and mitral conditions using two components LDA. The results shown that both the SJM and CM hinge flow fields exhibited a strong forward flow pattern during systole (maximum velocities of 2.31 and 1.75 m/s, respectively) and two main leakage jets during diastole (maximum velocities of 3.08 and 2.27 m/s, respectively). In the same year, Simon et al. (2004) [58] used two and three-component LDA techniques to quantify the velocity and turbulent shear stress fields in both the hinge flow region and the upstream leakage flow field, which focused on the 23 mm St. Jude Medical Regent. The measured peak phase-average velocity of leakage were 0.72 m/s, 0.95 m/s, 1.52 m/s, 0.6 m/s, 0.4 m/s at flat level and levels of 195 μm above flat, 390 μm above flat, 585 μm above flat and 1mm below flat level, respectively. Corresponding turbulent shear stresses were 700 $\mathrm{dyne/cm^2}$, 700 $\mathrm{dyne/cm^2}$, 1000 $\mathrm{dyne/cm^2}$, 2600 $\mathrm{dyne/cm^2}$, and 600 $\mathrm{dyne/cm^2}$ respectively.

In 2008, Manning et al. applied laser Doppler velocimetry to investigate hemolysis and thrombosis complications in a tilting disk valve [59]. They revealed flow pattern in the region just upstream of the mitral valve occlude and observed an atrial vortex on the major orifice side of the valve shed off the tip of the leaflet.

1.3.2 PARTICLE IMAGE VELOCIMETRY (PIV)

Traditional interpretations of complicated turbulent phenomena like hot-wire and Laser Doppler Anemometer (LDA) are one-point measurement techniques, and therefore not able to reveal the instantaneous spatial structure of a flow.

In 1998, Lim et al. used PIV techniques to investigated steady flow dynamics of prosthetic aortic heart valves including a porcine bioprostheses, a caged ball valve, and two single leaflet

tilting disc valves with different opening angles [60]. This study only considered the valve performances at the systolic peak flow phase of the cardiac cycle.

In 2001, Lim et al. mapped the velocity fields and turbulent shear stresses in the immediate downstream vicinity of a porcine bioprosthetic heart valve under pulsatile flow conditions with 2D-PIV and emphasized the importance of employing PIV measurements in the studies of stress related blood cell damage in prosthesis heart valves [61].

In 2003, Keefe B.Manning et al. [62] studied the regurgitant flow field of the St.Jude Medical bilealet mechanical heart valve, which was assessed using PIV under physiologic pulsatile flow conditions. The results demonstrated the typical regurgitant jet flow patterns associated with the St. Jude valve, and indicated the formation of a strong regurgitant jet, in the B-datum plane, along with twin vortices near the leaflets.

In 2004, Lu et al. took use of DPIV to analyze the closing behavior of mechanical aortic heart valve prostheses including monoleaflet (Medtronic Hall 27), bileaflet (Carbo-Medics 27; St. Jude Medical 27; Duromedics 29) and trilealet valves [63]. Different leakage jet patterns were observed during acceleration phase and distinguished closing times for different valve were reported.

In 2005, Akutsu et al. compared the results from time resolved PIV system to LDA for studying of the turbulent flow field of Bi-leaflet mechanical mitral prostheses heart valves. The results demonstrated that the PIV system was comparable to LDA [64].

In 2007, Shi et al. constructed a digital PIV investigation to analyze the pulsatile flow field around the bi-leaflet mechanical heart valve (MHV) in a complete heart cycle. The results revealed different flow patterns of forward and backward flow during a heart cycle [65]. Kaminsky et al. (2007) used 2D-PIV to investigate the evolution of the flow field in a detailed time domain of a commercial bileaflet PHV in a mock-loop mimicking unsteady conditions [66]. The hemodynamic flow patterns at downstream of the PHV were reported including the non-homogeneity and unsteadiness of the phenomenon and the presence of large-scale vortices within the field, especially in the wake of the vale leaflets.

In 2009, David W. Murphy [67] investigated the fluid mechanics of the b-datum line jet model with flow visualization and particle image velocimetry. The results from these studies presented instantaneous detailing the flow field of the regurgitant jet covering 30 ms during the cardiac cycle and the maximum velocity magnitude was up to 0.4 m/s. Amatya et al. (2009) made three-dimensional three-component velocity measurements in the flows surrounding prototypes of a mechanical valve and a silicone polymer valve to identify primary

three-dimensional flow in the instantaneous and ensemble-averaged flows surrounding both valves [68].

In 2010, Li et al. estimated turbulent shear stresses and viscous dissipative stressed induced by a mechanical valve using PIV data [69]. Their results showed maximum turbulent shear stress up to 800 $\mathrm{dyne}/\mathrm{cm}^2$ throughout the cardiac cycle, and viscous dissipative stresses below 120 $\mathrm{dyne}/\mathrm{cm}^2$. The level of shear stresses remains far below the threshold of RBCs, but could potentially damage platelets. Akutsu et al. (2010) investigated the influence of three mechanical bileaflet prosthetic valve designs (the St. Jude Medical, the On-X, and the MIRA valves) on the three-dimensional flow field inside a simulate aorta using dynamic PIV [70]. The observations were that newer design of the MIRA valve with circumferentially curved leaflets generates a strong diffuse flow with higher turbulence. Hutchison et al. (2010) applied stereoscopic PIV to measure steady flow through a bileaflet mechanical heart valve [71]. Their results showed a four-cell streamwise vortex structure in the mean velocity field.

In 2011, Li et al. used v to measure new trileaflet (TRI) 27mm and the St. Jude Medical 27mm valves in the aortic position of pulsatile circulatory mock loop and showed the major principal turbulent shear stresses were less than 1000 $\mathrm{dyne}/\mathrm{cm}^2$ for both valves [72]. Since the levels of shear stresses were comparable, the closing velocity of valves was considered as a main factor and might reduce the risks of thrombosis. Hutchison et al. (2011) studied downstream of a model BMHV in an axisymmetric aortic sinus using stereoscopic particle image velocimetry. The inlet flow was steady and the Reynolds number based on the aortic diameter was 7600 [73]. Results showed the out-of-plane velocity was of similar magnitude as the transverse velocity. Stühle et al. (2011) conducted a 2D-PIV experiment to evaluate the hemodynamic performance of the Sapien transcatherter heart valve (THV) in the aorta, and its influence on the aortic wall in an in-vitro set-up [74] and reported that the peak flow, strain rate, shear stress and vorticity of the Sapien PHV are slightly higher than that of native aortic valve, which may also have influence on the aortic wall. Bellofiore (2011) et al. developed a scale-up approach to enhance effective spatial and temporal resolution of PIV measurements [75]. The significant part of their studies was the observation of eddies as small as 400 μm shed near the downstream tip of valve leaflet.

1.3.3 OTHER METHODOLOGIES

In 1985, Williams et al. used Doppler echocardiography to determine normal values for commonly used prosthetic valves, including peak calculated aortic transvalvular gradients, mild aortic regurgitant and the effective mitral valve orifice [76]. They concluded that Doppler

echocardiography is a valuable tool for assessment of prosthetic and bioprosthetic heart valves and could provide noninvasive information by hemodynamic measurements. In 1991, Reimold et al. applied the same technique to study porcine bioprosthetic heart valves in the aortic valve position and suggested that the Doppler echocardiography may be useful for identifying subclinical bioprostnetic valvular dysfunction [77]. In 1993, Chambers et al. added the information by describing the echocardiographic appearance of the normal CarboMedics prosthesis in the aortic and mitral position [78]. The CarboMedics prosthesis was demonstrated to offer relatively little resistance to forward flow except at small annulus diameters. Based on Doppler echocardiography, Cape et al. (1996) addressed that the pressure drops predicted by Doppler technique correlate with catheter pressure drops within a valve size and position [79]. Similar researches and observations were taken by Otto et al. (1986) [80], Flachskampf et al. (1991) [81], Baumgartner et al. (1992) [82], Bitar et al. (1995) [83], Bench-Hanssen et al. (2001) [84].

In 1988, Hasenkam et al. measured flow patterns of six mechanical aortic valves (Björk-Shiley Standard, Björk-Shiley Convex-Concave, Björk-Shiley Monostrut, Hall-Kaster (Medtronic-Hall), St. Jude Medical and Starr-Edwards Silastic Ball aortic valves) by a catheter mounted hot-film anemometer probe [85]. The researches demonstrated that all velocity profiles were flat in the acceleration phase of systole and individual characteristic of profiles appeared from peak systole and throughout the systolic deceleration phase. Similar techniques were applied by Nygaard et al. in 1992 to visualize 2D color-mapping of the turbulent shear stress distribution at different instants during one mean pump cycle for a Hancock Porcine (HAPO) and a Ionescu-Shiley Pericardial Standard (ISPS) aortic valve [86]. The maximum turbulent shear stressed observed for the HAPO valve was 1940 $\mathrm{dyne/cm^2}$ and for the ISPS valve 1540 $\mathrm{dyne/cm^2}$.

In 1996, Fontaine et al. employed short echo time magnetic resonance imaging (MRI) to make the non-invasice, in vivo assessments of prosthetic valve function and compares the MRI data with LDA results [87]. The results showed good overall agreements between the MRI velocity measurements and the LDA data and that MRI method could provide an adequate method to produce the spatial structure of the flow fields. In 1999, Ringgaard et al. introduced a magnetic resonance imaging (MRI) – based technique to supply high-resolution assessment of velocity fields and shear stresses distal to prosthetic heart valves [88]. They demonstrated that the measured velocity profiles are comparable to previous studies with a clearly better visualization for the velocities of the jet emanating from the split between the leaflets. Houlind et al. (2006) conducted similar research work by using MR velocity mapping to provide valuable

information on velocity fields around prosthetic bileaflet aortic valves [89]. In 2010, Kvitting et al. promoted the applications of generalized phase-contrast MRI in vitro assessment of flow patterns and turbulence intensity [90].

In 1998, Healy et al. [91] applied dye injection to visualize the retrograde hinge flow pattern of the Medtronic Parallel bileaflet heart valve. The detailed flow structures observed showed the hinge's inflow channel was the most suspect region for thrombus formation.

In 2002, Kleine et al. investigated the influence of valve orientation on coronary artery flow in an animal model and reported the apparent differences of coronary flow rates from several common used prosthesis valves [92]. They demonstrated that coronary blood flow was significantly influenced by mechanical aortic valve implantation and the orientation of prostheses. In 2006, Nyboe et al. implanted three bileaflet mechanical heart valves into 19 female pigs to measure turbulent stress downstream [93]. They reported that turbulent stress correlated with increasing cardiac outputs and the maximum instantaneous turbulent stress observed was 470 $\mathrm{dyne/cm^2}$.

In 2003, Grigioni et al. used the laser vibrometry technique to investigate the kinematics of three commonly implanted mechanical bileaflet heart valves (St. Jude HP, Sorin Bicarbon, Carbomedics, tissue annulus diameter 27 mm) [94]. The proposed method could furnish a typical "fingerprint" characterizing each valve behavior in repeatable experimental conditions.

1.4 THE AIM OF THIS PROJECT

The purpose of this present study was to improve the knowledge about near-hinge regurgitant flow dynamics of typical BMHVs. The methodologies applied in this thesis are including experimental measurement and numerical simulation. A Particle Image Velocimetry (PIV) investigation was carried out on currently marketed BMHVs, by measuring the 2D flow field at serial planes encompassing the plane of the two distal hinges. The properties of flow field of leakage were evaluated as average velocity field, Turbulent Shear Stress (TSS), hemolysis index (HI). To verify the repeatability of the results, multiple experiments were carried on at different times under same experimental conditions. Comparisons of multiple experimental results allowed us to perform a variation analysis, which is critical for simulation validation. The averaged experimental data from repeatability tests was used as research basis of models selection and mesh independence analysis for CFD simulation works. The data from numerical simulation could be used to analysis the insight hinge region where PIV measurements cannot obtain.

Take use of experimental and simulation methodologies, a standard procedure could be defined for sufficient confidence in risk evaluation and mitigation of prosthetic heart valves.

In chapter 2, the overview of PIV system will be described. The hardware and software will be demonstrated according to our measurement system. The methods for PIV image analysis will be described as well. In order to guarantee the quality of PIV measurement, the optimization rules for PIV analysis will be given and strictly followed throughout the experiments in the thesis.

In chapter 3, a standard nozzle is used to evaluate the limitations of the validation for computational fluid dynamics (CFD) as the first phase of our project in assessing blood flow parameters related to medical device safety. The standard nozzle, which mimicked the characteristics existing in common medical devices, is composed of a gradual flow constriction, a narrow throat pathway, and a sudden expansion region where a symmetrical jet is emitted to surrounding zones.

In chapter 4, two typical BMHVs will be investigated with PIV measurements. Repeatability tests will be executed for hemodynamic properties including velocity magnitude and turbulence shear stress through multiple experiments.

In chapter 5, the computational fluid dynamics (CFD) will be applied for numerical simulation of leakage jets existing in regagitant phase of BMHVs. The validations for numerical procedures will be accomplished with the help of averaged multiple experimental data. Furthermore, the flow patterns insight hinge region will be investigated using validated numerical data.

In chapter 6, the conclusions and the direction of future works will be given.

Chapter 2
Introduction to PIV

2.1 OVERVIEW

This chapter gives an overview of PIV system by describing a brief introduction to PIV technology and PIV system components. The lab environments and the PIV system are shown in Fig. 2.1.

Particle Image Velocity (PIV) is the simultaneous measurement of fluid or particle velocity vectors at matrix points, applying optical imaging techniques. Using PIV system, the flow field can be visualized in planar slices and can be measured over three-dimensional volumes, in principle. PIV is an ideal technology to capture unsteady flow fields with accuracy and spatial resolution comparable to LDA or thermal anemometry.

The velocity measurements in PIV system are taken by determining the distance of particles displacements in the flow in the certain time interval between pulses of laser light. When the laser is pulsed, the light sheet illuminates an image of particles, which is captured on the camera, shown as Fig.2.2. Double pulsing lights from laser generator provide the double-frame image with particle displacements. By measuring the distance of particle displacements and dividing by the certain time interval, the velocity of the particle can be determined. The velocity field of the whole measured domain can be produced by calculating particle velocities at many points. With determination of high accurate velocity, other parameters of fluid dynamics can be calculated, such as turbulence intensity, turbulent shear stress and turbulent kinemics energy.

In this section, the technology review is divided into two sections including the hardware part and software part. The table 2.1 shows the details of the main components assembled in PIV system.

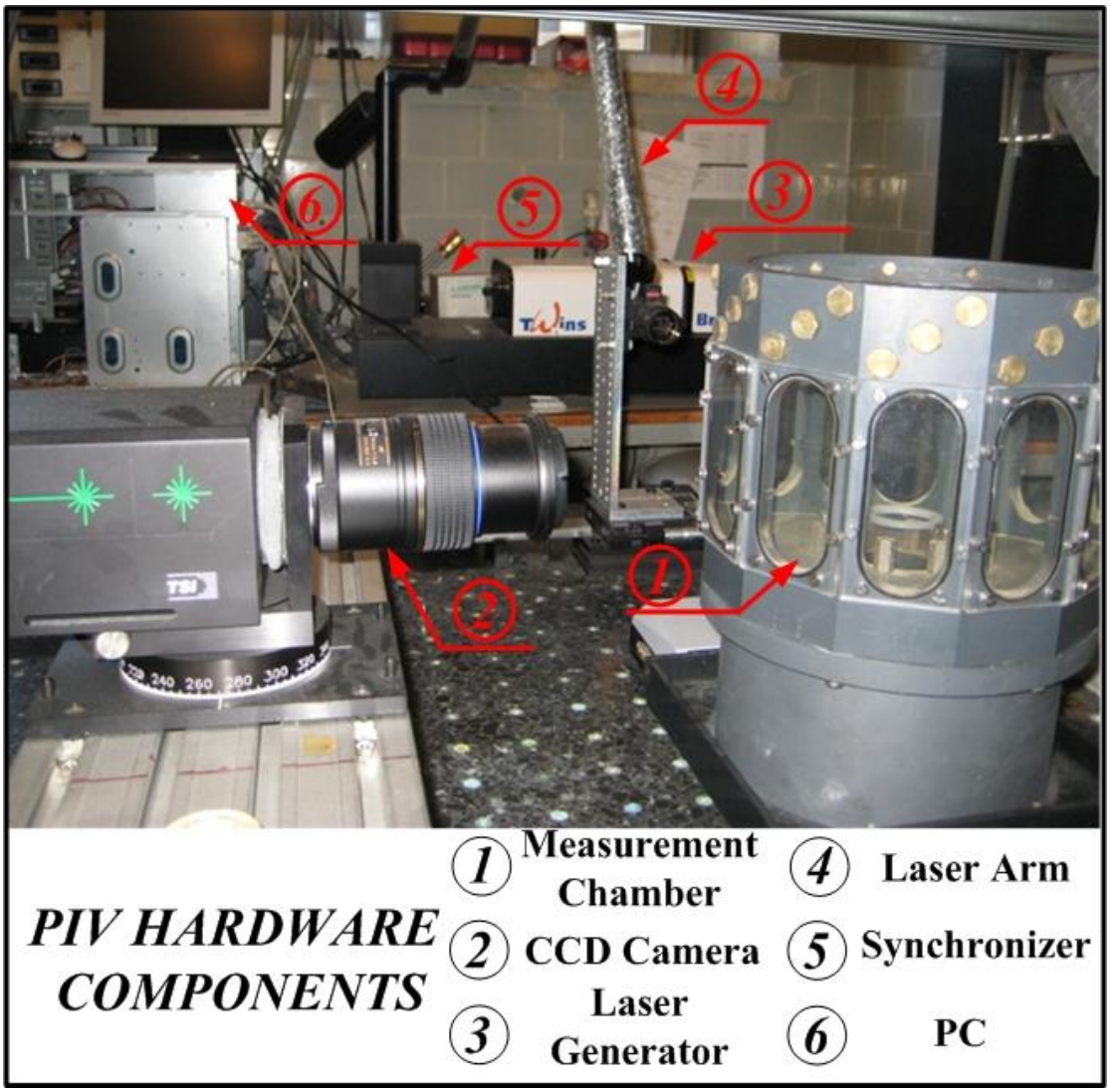

Figure 2.1: lab conditions and PIV components

Hardware	CCD Camera	PIVCAM 13-8
	Lens	Nikon AF Micro-Nikkor 60mm lens
	Synchronizer	TSI model 610034
	Laser Generator	Double_pulsed Nd:YAG laser
	Image Shift	Alph Getriebebau Gmbh
	System control	PC
Software	System control and cross-correlation analysis	INSIGHT 3G (TSI,Inc., Shoreview,MN)
	Image analysis and processing	MATLAB

Table 2.1: components in PIV system

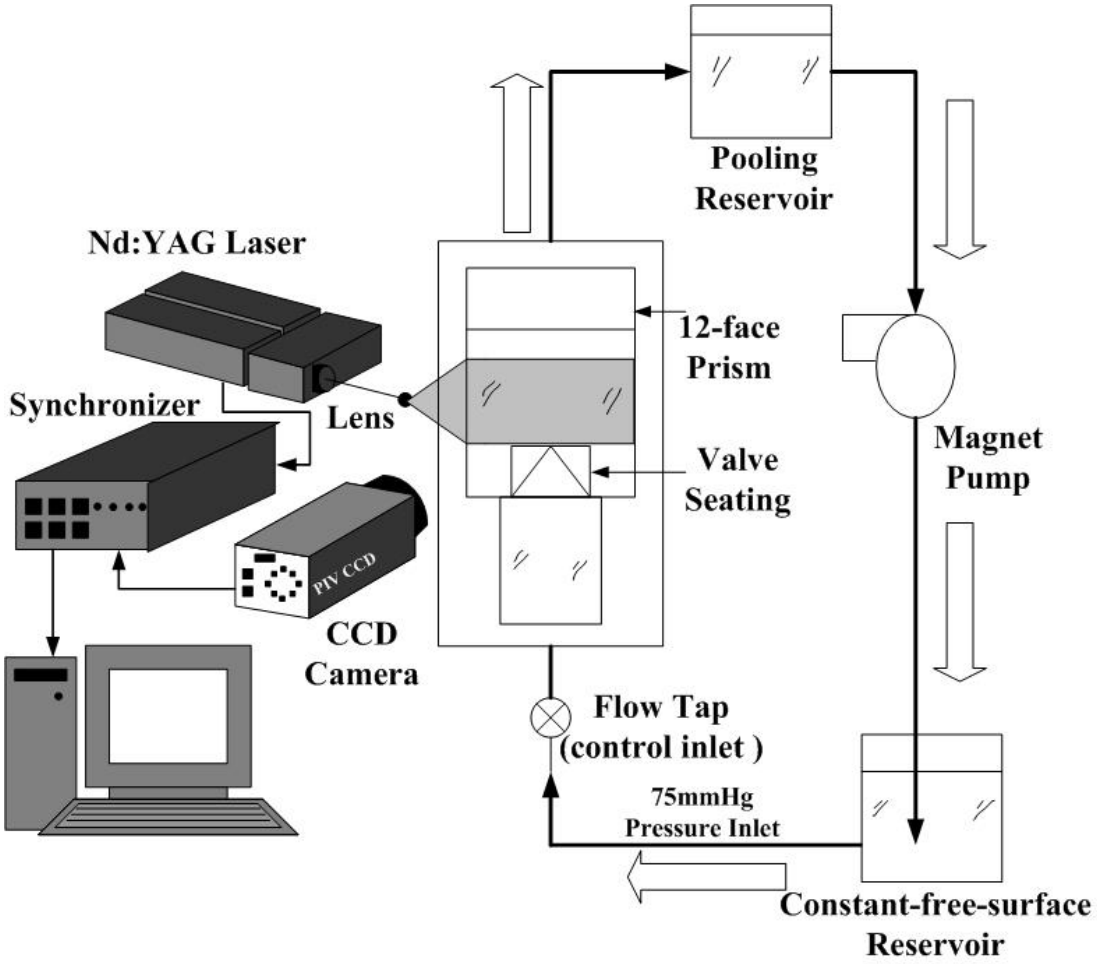

Figure 2.2: PIV Photography System

2.2 HARDWARE

2.2.1 SYNCHRONIZER

To produce a velocity flow field image with PIV system, the laser pulse and the camera must be connected and triggered with the correct sequence and adjustably timing according to the flow conditions. The synchronizer is used to make all the components work together, which is critical for taking PIV photography. Each of components requires a timing sequence to operate and guaranty a good photography. However, there are a couple cases where sequencing the operation of the equipment by a synchronizer is not really necessary, such as using an argon iron laser or measuring very low-speed flows using a video camera. In cases where the laser is being double pulsed or image shifting is being used, you have to ensure that all the parts are working together. Fig. 2.3 shows a typical timing sequence controlled by the synchronizer. Fig. 2.4 illustrates synchronizer system for PIV measurements.

The computer uses RS232 commands to control the synchronizer. Additionally, it is possible to

have a program communicate directly with synchronizer as well. The ability of direct communications could allow synchronizer to execute special functions like taking images in coordination with a traverse movement or other applications.

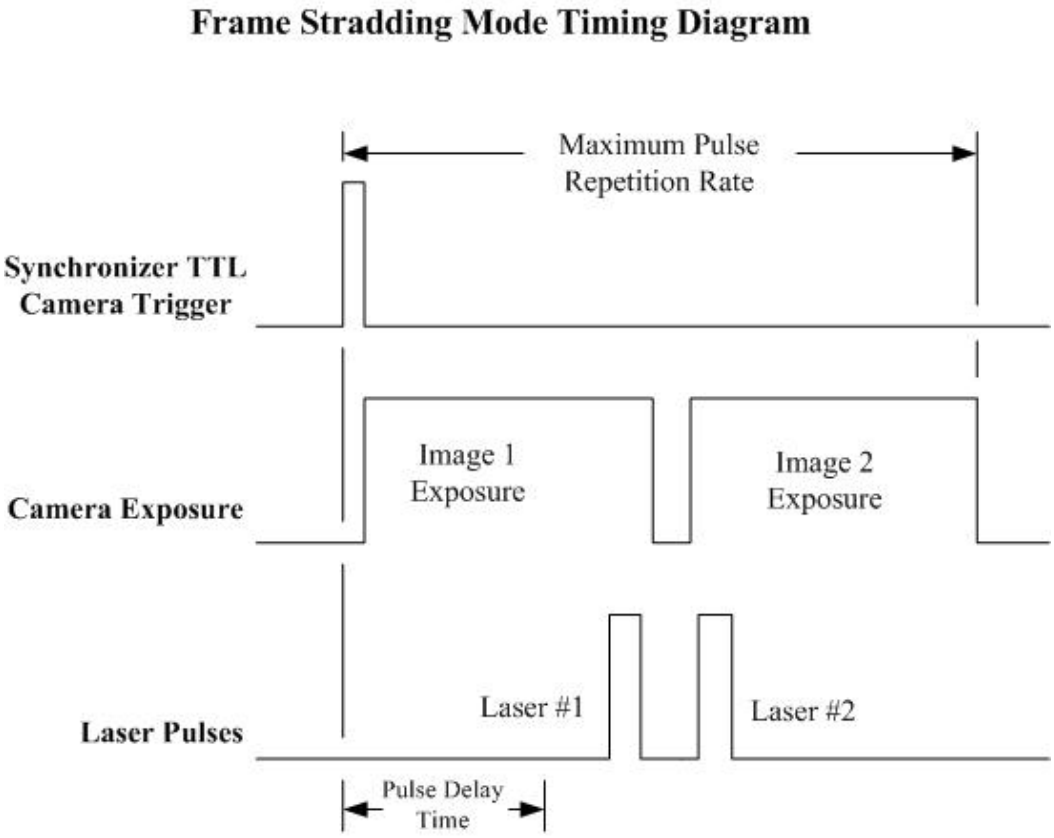

Figure 2.3: timing sequence diagram for different components

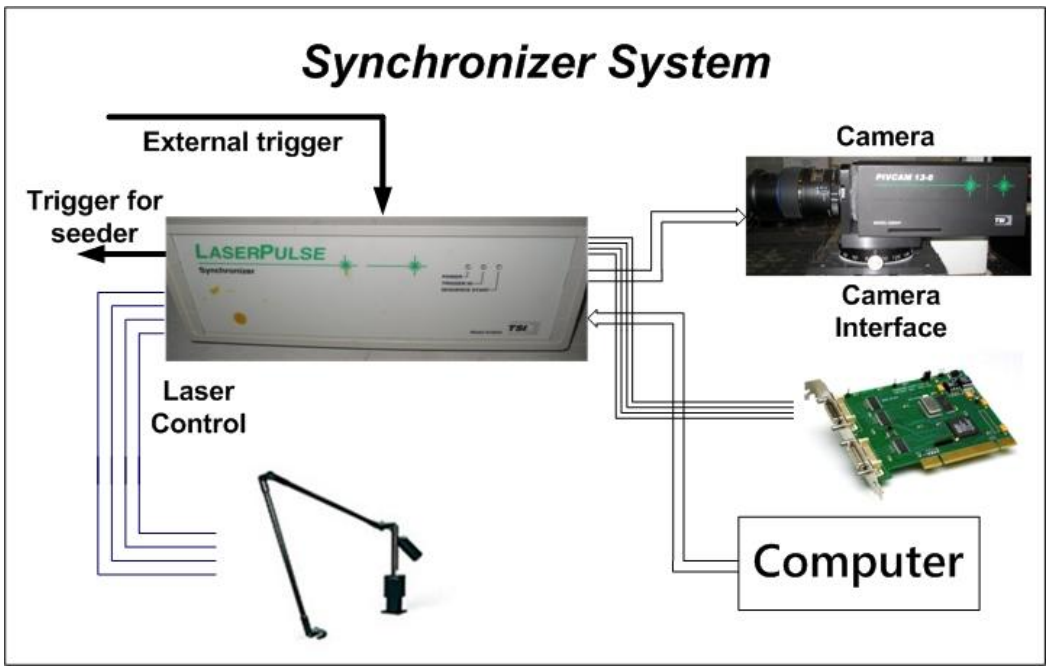

Figure 2.4: synchronizer connections

2.2.2 LASER

The PIV illumination system is composed of the pulsed laser and the lightsheet optics.

In PIV system, Double Pulsed Nd:YAG is selected as the type of lasers. Frequency doubled Q-Switched Nd:YAG lasers produce short duration (10 ns) high energy (50 mJ to 1000 mJ) pulses of light green (532 nm). The pulse energy is high enough to illuminate sub-micron particles in air. The pulse duration is short enough to freeze the motion of super-sonic flows. This make the Nd:YAG laser well suited for PIV applications. A flashlamp is used in the Nd:YAG laser to produce the energy that is converted into the laser beam. The fire frequency of the flashlamp can be at about 10 Hz, which supplies the required short times between pulses either two Nd:YAG lasers or a Double Pulsed Nd:YAG laser can be used.

Laser generator system has two complete Nd:YAG lasers cavities, Q-Switches and beam combination optics to create the collinear beams. For Double Pulsed Nd:YAG laser system, Q-switches is required to fire twice during a flashlamp to generate a pair of laser pulses. With the Double Pulsed Nd:YAG, the timing of the pulses needs to be adjusted to get two pulses with equal energy.

To design Nd:YAG laser for best performance, a specific flashlamp frequency and voltage need to be considered. The operation of the flashlamp generates heat that causes the YAG rod to expand. The end of the Nd:YAG are concave at room temperature so that when they expand with thermal lensing the rod ends become flat. In some case, if the frequency of laser and camera are not matching, the Q-Switch Divide parameter is applied to decrease the rate of laser pulsing and guaranty it working at the optimum frequency range.

To produce the laser sheet that illuminates the particle flow, a set of cylindrical and spherical lenses are equipped in each laser system. Fig. 2.5 shows a typical optical system for generating optimum laser sheet. The lightsheet height divergence angle is controlled by the cylindrical lens while the lightsheet thickness is controlled by the spherical lens. Since the cylindrical lens is much more powerful with a shorter focal length, the spherical lend has little effect on the light height.

To setup lightsheet optics, we need to pay attention to the beam divergence over the photograph area. For the PIV experiments, the requirement for the lightsheet thickness is less than 1-mm. The function of spherical lens is to reduce the lightsheet thickness. At the focus point, the lens creates a waist, on the side of which the beam diverges. The focus length of the optical system is inversely proportional to the lightsheet thickness divergence. Since the lightsheet intensity is proportional to the cross section area if the beam diverges too much

across, the properties might vary too much. To exposure the particle flow, the intensity of light sheet needs to be high enough. The double-frame images can be taken anywhere along the light sheet, but usually the optimum location is at the focal distance of the spherical lens near the light sheet thickness waist, where the light sheet is the thinnest.

The Nd:YAG laser power can controlled either by flashlamp energy control or by setting the Q-Switch Delay time. The best beam quality is obtained by running the flashlamps at full power.

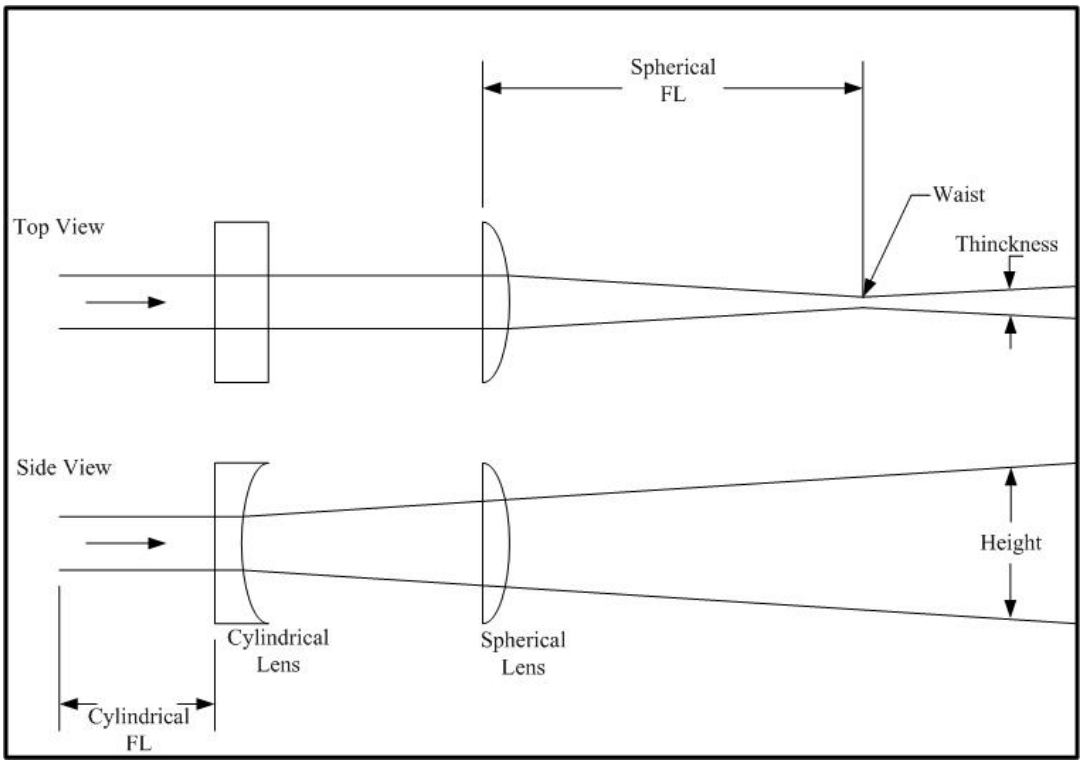

Figure 2.5: light sheet dimensions

2.2.3 IMAGE CAPTURE

In our PIV system, we choose a CCD camera instead of photographic film camera for the advantage of using CCD image capture is that the vector field is available on-line. The function of CCD camera is to convert light energy into electrical energy and send an electrical image to the frame grabber in the computer.

The properties of CCD camera can vary in the number of pixels per image, frame rate, time between exposure, and timing electronics. The model PIVCAM 13-8 has been selected for PIV measurements because of its several well designed features. An asynchronous double exposure mode in PIVCAM 13-8 model allows a frame straddle pair of images to be captured less than 300 μm after an external trigger signal. This fast reset allows to capture a crosscorrelation pair of image at an exact time is desired.

The parameters of digital output from CCD camera can be adjusted by the computer. These parameters are including gain, offset, gain balance and offset balance. The slope of the conversion between pixel change and pixel intensity is adjusted by the gain setting. The gain setting of 1 means the output intensity of digital pixel is 255 when the pixel has its maximum charge. The gain setting of 4 means the output intensity is 255 when the pixel only has 1/4 of the maximum charge. Thus, the gain setting of 2, 4 can be used to increase the image brightness. The offset valve is added or subtracted from each digital output pixel intensity value. The signal to noise ration can increase by subtracting the offset value from pixel intensity value. The setting of gain balance and offset balance keep the output of odd and even channels equal.

In double-frame capturing mode, the camera takes two images for cross-correlation when triggered by the synchronizer. The exposure time for the first frame is very short, 255 μm, only enough time to fire a Nd:YAG laser flashlamp and Q-Switch. The second exposure is longer with 32.4ms enough for the camera to transmit the first 255 μm exposure to the frame grabber before the second image can be moved into the readout registers.

The pixels of PIVCAM 13-8 model are 1280×1024 and the frame rate is 10Hz.

2.3 SOFTWARE

In PIV system, INSIGHT 3G is used for global image capture, analysis and display purposes. With the help of INSIGHT 3G's batch-mode capturing and processing feature, large number of image s in actual experiments can be captured and processed.

There are two main functions for INSIGHT 3G: an acquisition and processing function and a presentation function. For PIV measurement, an image is firstly captured and processed to obtain various properties such as velocity vectors, temperature or density information or spray geometry. The presentation function is used to guaranty these results to be enhances for optimal viewing. In our software system, MATLAB and TECPLOT are also applied as additional tools for data reduction and flow field representation. Fig 2.6. shows the flow chart for PIV image process and illustrates the functions for different software.

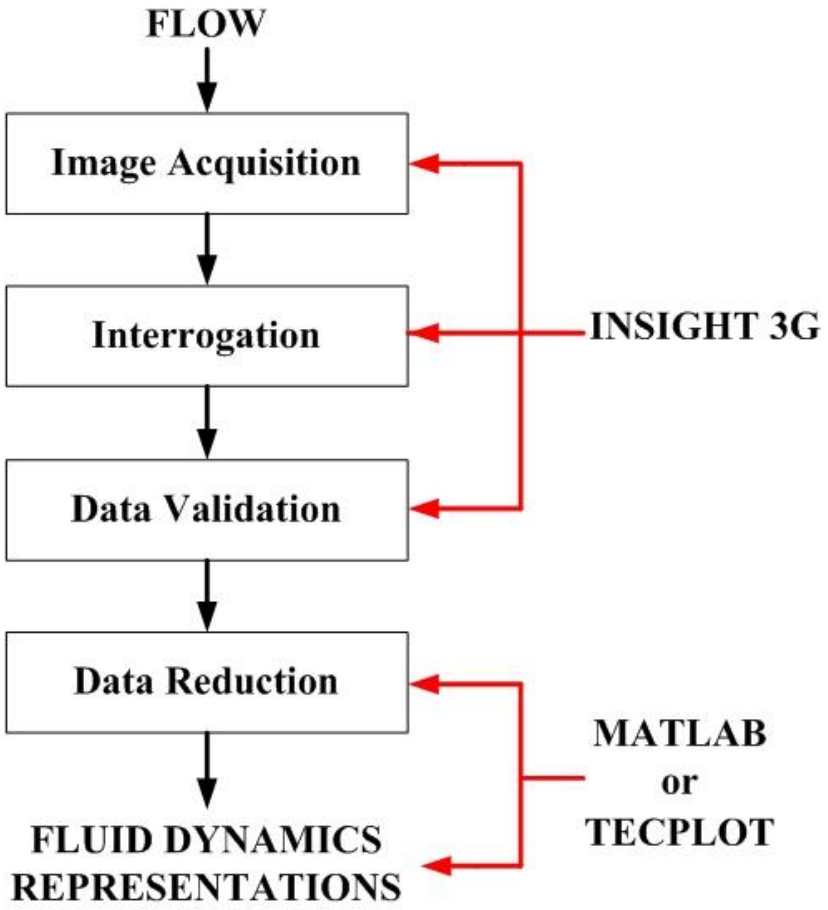

Figure 2.6: PIV image processing

2.3.1 IMAGE ACQUISITION

In our system, INSIGHT 3G offers options to capture numbers of images for PIV measurements. Before capturing images, the hardware components need to be set with suitable values and specified, which has been described in last section.

The PIV frame mode is 'straddle' model to continuously make camera acquire two consecutive single-exposure images. INSIGHT 3G uses 'Pulse Rep Rate (Hz)' to specify the timing from the start of one laser pulse sequence to the start of the next laser pulse sequence. 'Laser Pulse Delay' is used to adjust to pulse the laser precisely towards the end of the first frame. The pulse separation Delta T (μs) is a key parameter to properly measure the particle velocity field in PIV system. In YAG laser system, Delta T means the time delay between the firing of Q-Switch 1 and Q-Switch 2. Typically, the setting of this parameter needs to guaranty that the maximum displacement is less than a quarter of the spot window size to optimize the particle image displacement. 'PIV Exposure time (μs)' is the parameter to define the time that first frame on PIV camera is open.

The capture mode is selected as ‘sequence’ during the PIV experiments to acquire a sequence of double-frame images. In our case the maximum number of images is 1000 depends on our camera type and available storage space.

During the alignment, the setting of laser energy is ‘low’ or ‘medium’ to make laser generate a consistent green beam. To obtain the optimum image quality in our lab environments, the laser power and pulse energy are selected as ‘high’ option for both laser channel A and B during the capture of double-frame image.

2.3.2 INTERROGATION

PIV can be used to measure the velocity of a fluid field at many locations within a 2D plane. In the flow, the small tracer particles are seeded with proper density. The measured flow domain is illuminated by a thin light sheet. A camera makes it focus on the light sheet to record the images of the particles. With the light sheet pulsing twice, the double-frame image of the particle field is recorded and the flow velocity can be estimated by measuring the distance of the particles displacements in the time between the light sheet pulses. In this section, the methods of image analysis for the double-frame image are described. The Fig. 2.7 demonstrates the flow chat for the double-frame image analysis including image conditioning, image preprocessing, cross-correlation mapping, peak engine for particle displacement, vector storage and representations. The flow chat shows the processing steps and how a vector field is generated from the input images and the process data.

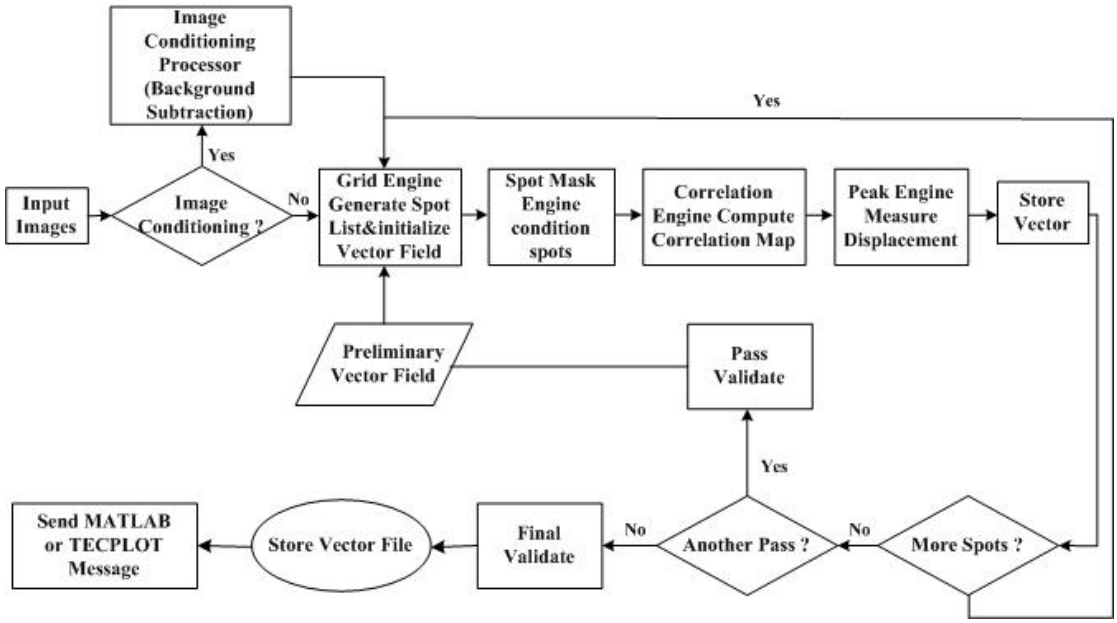

Figure 2.7: flow chat for double-frame image analysis

In the process of the image analysis, we used the Cross-Correlation algorithm to indentify the

displacement of particles. For cross-correlation analysis of image, a certain number of particles in one interrogation window are reasonably required. Normally, 4 to 6 particles in one interrogation window is a good solution for PIV techniques. To satisfy this requirement, a statistic method is supplied in this report, which takes a sliding window with the same size of interrogation area to count the number of particles at each sub-region of the original particle image. The moving size of each step was half size of interrogation window. The average intensity of particles in the interrogation was evaluated after the sliding window scanning the entire image field. According to the statistics, the size of interrogation window for cross correlation was determined.

The function of the GridEngine is to break the input images up into smaller spots for processing and initializes the vector field. The process for each grid point is that the pixels from the input images are coped into the spots and the spots are passed into the SpotMaskEngine. According to straddle image capture mode for double-frame image, spot A is from frame A and spot B is from frame B. In our case, the spot A and B are square and same size. The grid engines of PIV cross correlation are Nyquist Grid and Recursive Nyquist Grid. Nyquist Grid is selected for fast results and it was the classic PIV grid. It set vectors with the x spacing equal to half width of interrogation window and the y spacing equal to half height of interrogation window. No spot offsets are used and the processing uses only a single pass. This gave a vector grid with 50% spot overlap fitting the Nyquist sampling criteria. Recursive Nyquist Grid was used for increased accuracy or higher spatial resolution. Compared to the Nyquist Grid, it processed the images in two passes. The first processing pass computed the vector field at the starting spot sizes with Nyquist. The results of the first processing pass are used to optimize the spot offsets for the second processing pass. By offsetting the spots by the particle image displacement distance, lost pairs due to in-plane motion are eliminated increasing the correlation signal-to-noise ratio. As the final size of interrogation window decreasing by a factor of two, the resolution of vector field increased by a factor of two.

In INSIGHT 3G, the CorrelationEngine is used to compute the correlation function and return it as a correlation map. It calculates the correlation function between spot A and spot B. The correlation function is an algorithm that sums the particle image matches at all pixel displacements within the displacement range. The highest correlation map pixel is assumed to be the particle image displacement peak caused by the contributions of many particle pairs. Other peaks are assumed to be noise peaks caused by the random pairings of images of different particles. Correlation algorithms may generate peaks with different sizes, shapes, or slopes. The measurement accuracy may be improved by matching the peak algorithm to the

correlation algorithm. Fig. 2.8 illustrates the cross-correlation for two input signals.

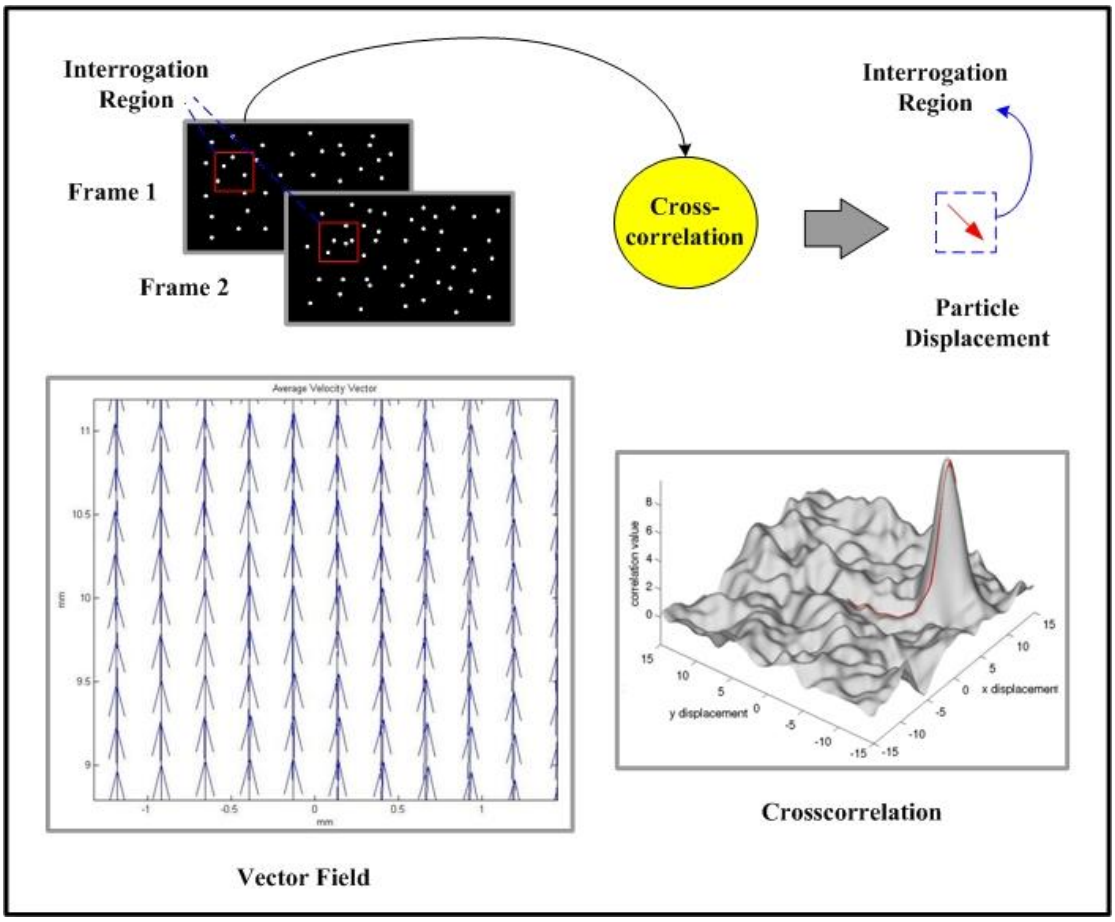

Figure 2.8: principle for cross-correlation function

In this report, we applied FFT-Correlator as the PIV cross CorrelationEngine. It computed the correlation using Fast Fourier Transform (FFT). This algorithm required the spots to be square powers of two and have same size.

For the Peak Engine algorithm, we select Gaussian Peak as plugin type. This algorithm locates the peak value of the correlation map with sub-pixel accuracy by fitting a Gaussian curve to the highest pixel and its four nearest neighbors. Two 3-points fitting are done: one in x direction with the peak value and two pixels from the left and right to the peak value and one in y direction with the peak value and two pixels from up and down to the peak value. The equations for determination of x pixel peak are as follow:

$$X\_sub = \frac{\log(I\_left) - \log(I\_right)}{2*\log(I\_left) - 2*\log(I\_center) + \log(I\_right)}$$

$$dX = X + X\_sub - X\_zero$$

$I\_left \longrightarrow$ pixel intensity value for the left of the peak

$I\_right \longrightarrow$ pixel intensity value for the right of the peak

$I\_center \longrightarrow$ pixel intensity value for the peak in x direction

$X\_sub \longrightarrow$ the sub-pixel peak location in x direction

$dX \longrightarrow$ particle image displacement in x direction

$X \longrightarrow$ x index of peak pixel

$X\_zero \longrightarrow$ x index of zero velocity pixel

The equations for determination of y pixel peak are as follow:

$$Y\_sub = \frac{\log(I\_up) - \log(I\_down)}{2*\log(I\_up) - 2*\log(I\_center) + \log(I\_down)}$$

$$dY = Y + Y\_sub - Y\_zero$$

$I\_up \longrightarrow$ pixel intensity value for the up of the peak

$I\_down \longrightarrow$ pixel intensity value for the down of the peak

$I\_center \longrightarrow$ pixel intensity value for the peak in y direction

$Y\_sub \longrightarrow$ the sub-pixel peak location in y direction

$dY \longrightarrow$ particle image displacement in y direction

$Y \longrightarrow$ y index of peak pixel

$Y\_zero \longrightarrow$ y index of zero velocity pixel

2.3.3 DATA VALIDATION

Validation macro was applied to the vector field after each processing pass. In recursive processing two validation macros were used for each pass. Validation macro had functions of spurious vectors removing and holes filling through interpolation. Spurious vectors could be induced by the results of correlation of random pairing of particle images. Holes on the velocity field were caused by in-plane and out-plane motion or low seeding density with low correlation signal strength. To processing the spurious vectors, vector editing is necessary by setting a proper thresholds value. During the image validation, the signal-to-noisy ratio at each spot must pass the threshold to be considered a valid vector.

2.3.4 DATA REDUCTION

In this section, the extracted data was applied to determine the fluid dynamics properties of the measured flow. Through taking average of 1000 velocity field measurements, mean value of

the velocity along x direction U_x and mean value of the velocity along y direction U_y were calculated in the first procedure. The root mean square values of the velocity fluctuation were determined as equation (1) along x direction and y direction.

$$u'_x = \sqrt{\overline{u_x^2}}, \quad u'_y = \sqrt{\overline{u_y^2}} \tag{1}$$

The turbulent intensity along x direction and y direction were evaluated according to equation (2).

$$I_x = \frac{u'_x}{\overline{U}_x}, \; I_y = \frac{u'_y}{\overline{U}_y} \tag{2}$$

The turbulence shear stress (TSS) is defined as the equation (3).

$$TSS = \rho\overline{u'_x u'_y} \tag{3}$$

ρ is density of fluid.

However, TSS was not qualified to estimate the maximum TSS, because it was related to a fixed (x, y) reference system. To solve this problem, it was helpful to refer to a suitable coordinate system (ξ, η, ζ), in which the TSS tensor was cast in a diagonal form:

$$T = \rho\overline{u'_i u'_j} = \begin{pmatrix} \sigma_1 & 0 \\ 0 & \sigma_2 \end{pmatrix} (i, j = \xi\eta\zeta),$$

where σ_1, σ_2 (in the conventional ordering scheme, $\sigma_1 > \sigma_2$) were the two principal in-plane normal stress (PNS). These two PNS were calculated as equation (4).

$$\sigma_1 = \rho \max_{2D}\left\{\overline{u^{*2}}\right\} \text{ and } \sigma_2 = \rho \min_{2D}\left\{\overline{u^{*2}}\right\} \tag{4}$$

Where u^{*2} was a squared velocity fluctuation component in an arbitrary direction in the (x,y) plane.

As it is known from stress analysis (Malvern, 1969 [95]), the maximum TSS is defined simply by the equation (5).

$$TSS_{\max} = \frac{\sigma_1 - \sigma_2}{2} = \frac{\rho}{2}\left(\max_{2D}\left\{ \overline{u^{*2}} \right\} - \min_{2D}\left\{ \overline{u^{*2}} \right\} \right) \quad (5)$$

The maximum TSS could be used to evaluate the possibility of hemolysis and thrombus events occurring in blood flow.

2.4 RULES-OF-THUMB FOR OPTIMIZATION OF PIV ANALYSIS

To get the best results from a PIV experiment, the image capture and the interrogation window must be optimized according to the flow conditions. Typically, the parameters that can be controlled for optimization are: interrogation window size, light sheet dimensions; seed particle and concentration; the time interval between the double-frame image; and photograph magnification. In this section, the common rules for PIV measurements are briefly described.

2.4.1 INTERROGATION WINDOW SIZE

The interrogation window size should be small enough to describe the flow with vector for that spot. In an interrogation spot there is a limitation on the velocity gradient. If the velocity gradient is too large then the displacement peak becomes larger in the area with a lower peak height, leading to the likelihood of measurement noise. Since the correlation produces the average velocity within one interrogation window, the more the averaging takes place with the larger size of window. To obtain finer resolution and more details, smaller size of window is required.

2.4.2 THE NUMBER OF PARTICLE IMAGE PAIRS PER INTERROGATION

The percentage of correct velocity measurements is a function of number of particle pairs per interrogation window [96].As the concentration of particle pairs in one interrogation window, the percentage of valid measurements increases. This is because many particle pairs are accounted for the displacement peak. The signal-to-noise ratio is enhanced by decreasing the noise peaks caused by the correlation of the image of different particles. The loss of some pairs is tolerable because many others pairs are still creating the displacement peak. Normally, the suitable number of particles per interrogation window is 4-6 for best results.

2.4.3 MAXIMUM IN-PLANE DISPLACEMENTS

This maximum displacement is considered as a compromise between two parameters: large displacements for the best percent of reading accuracy and small displacements to minimize lost pairs. The result of compromise is that the maximum in-pane displacements should be less than 1/4 interrogation window size.

2.4.4 MAXIMUM OUT-PLANE DISPLACEMENTS

This aspect is considered for keeping the lost of particle pairs to an acceptable level. Theoretically, the maximum out-of-plane displacement should be less than 1/4 of light sheet thickness.

2.4.5 MINIMUM IN-PLANE DISPLACEMENTS

The minimum displacement need to be restricted to avoid the overlapping of two particle images. The autocorrelation zero peak and displacement peaks must be separated to accurately measure the centroid of the displacement peak. If the peaks overlap, the centroid will include some of the zero peaks and bias the measurement towards zero displacement. Thus, the minimum in-plane displacement should be two particle image diameters.

2.4.6 EXPOSURE REQUIREMENT

The requirement for exposure is that particles should be shown clearly for image capture. The factors that may influent the exposure are: laser energy; light sheet dimensions; the length of camera focus, photograph magnification; particle size and material; film speed and resolution.

Regarding particle scattering, particle size and material determine the scattered light power in the image of each particle. Generally, a Nd:YAG laser is used for high speed flows with micron-sized seed particles.

Chapter 3

PIV Analysis of a Standard Nozzle and Validation of Computational Fluid Dynamics Simulation

In this chapter, a standard nozzle is used to evaluate the limitations of the validation for computational fluid dynamics (CFD) as the first phase of our project in assessing blood flow parameters related to medical device safety. The standard nozzle, which mimicked the characteristics existing in common medical devices, is composed of a gradual flow constriction, a narrow throat pathway, and a sudden expansion region where a symmetrical jet is emitted to surrounding zones. Measurements of average velocity and turbulent flow quantities are made and the results are proved reproductively in our laboratory using particle image velocimetry (PIV).

The performances of flow condition are conducted over a rage of nozzle throat Reynolds number (Re_{throat}) from 1800 to 8000, covering the laminar, transitional, and turbulent flow regimes.

We defined laminar flow when a fluid passes through parallel layers, with no disruption between the layers [97]. The structure of laminar flow is illustrated by Figure 3.1 (a). Laminar flow tends to generate at low velocity regimes without lateral mixing and adjacent flow layers pass each other slide and smoothly. Thus, there are no cross currents perpendicular to the direction of flow, nor eddies or swirls of fluids [98]. When particle flow passes a pipe in laminar regime, the motion of particles in the flow is orderly in straight line parallel to the pipe walls. The characteristics of laminar flow in fluid dynamics are high momentum diffusion and low momentum convection. Turbulent flow, in contrast to laminar flow, undergoes fluid irregular fluctuations or mixing.

Turbulent flow in fluid dynamics is a flow regime characterized by chaotic and stochastic property changes. Other properties of turbulent flow are including low momentum diffusion, high momentum convection, and rapid variation of pressure and velocity in space and time. Most kinds of nature flow are turbulent, except for laminar flow at the leading edge of solids moving relative to fluids or extremely close to solid surfaces, such as the inside wall of a pipe, or

in cases of fluids of high viscosity flowing slowly through small channels. We can give common examples for turbulent flow as blood flow in arteries, oil transport in pipelines, lava flow, atmosphere and ocean currents, the flow through pumps and turbines, and the flow in boat wakes and around aircraft-wing tips. Turbulence was described as the most important unsolved problem of classical physics by Noble Laureate Richard Feyman [99]. The typical structure of turbulent is illustrated in Figure 3.1 (c).

Transition flow is mixture of laminar flow and turbulent flow. When transition flow passes pipe, turbulent flow regime is observed at the center of pipe and laminar flow regime reserves near the edges. The transition flow is demonstrated in Figure 3.1 (b).

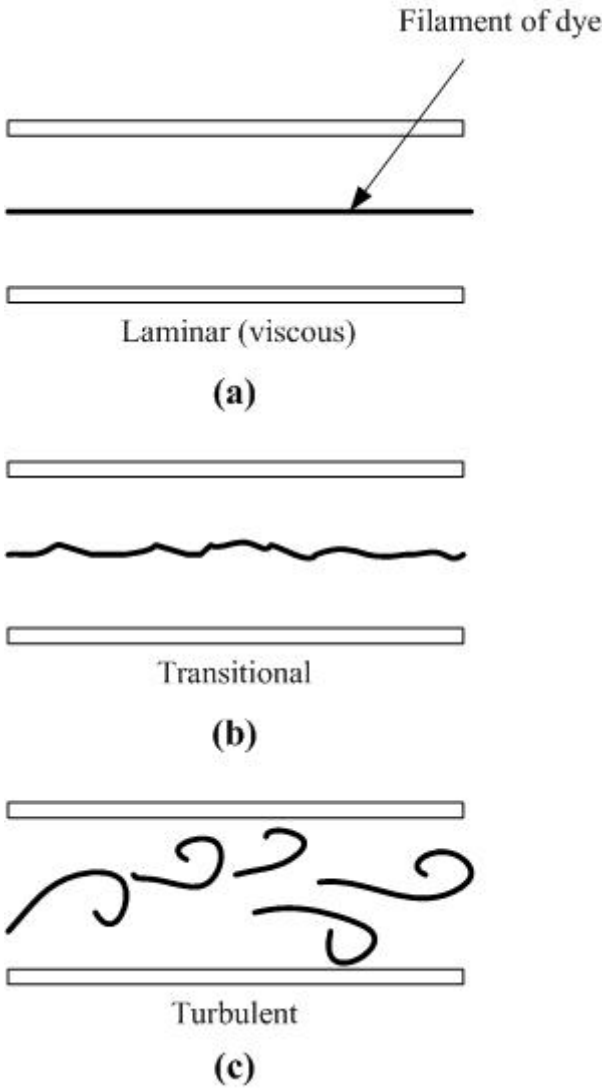

Figure 3.1: flow structure for different flow regimes

The different properties for laminar, transition, and turbulent flow regimes are illustrated in table 3.1.

Flow Regime	Laminar Flow	Transition Flow	Turbulent Flow
Reynolds Number	Re<2000	2000<Re<4000	Re>4000
Velocity Range	Low	Medium	High
Dye Behavior	Do not mix with water	Mix slightly	Mix rapidly and completely
Particle Flow	Straight lines	irregular	Completely irregular
Velocity Fluctuation	Low	Medium	High
Vortex	Rare	Common	Frequent
Turbulent Shear Stress	Low	Medium	High
Mathematical Analysis	Simple	Difficult	Difficult
Practice in nature	Rare	Common	Most common type of flow

Table 3.1: properties of flow regimes

3.1METHODS AND MATERIALS

In this section, the experimental setups and flow loop conditions are described in detail for suitable PIV measurements. Additionally, calibration method and measurement coordinates are demonstrated and represented. To classify different flow regimes, Reynolds number is introduced to define flow properties according to distinguished flow rates.

3.1.1 EXPERIMENTAL SETUPS AND FLOW LOOP

The experiments were conducted in the steady-flow experimental in vitro chamber. During the 2D slices acquisition, the pump was kept to work in order to study the same flow field throughout the series of measurement. A large chamber (upstream chamber) with optimized optical access for PIV measurement was employed in the steady-flow loop for mimicking inlet and outlet of measured targets, such as ventricle and atrium for mitral valve. A mechanical

structure was placed between the chambers and securely held the nozzle under study. The flow loop is composed of an above reservoir, pooling reservoir, downstream chamber, upstream chamber and hydraulic pump, where are connected through pipes. Figure 3.2 shows the flow loop system used in PIV measurements. The circulation fluid was forced by hydraulic pump supplied to a reservoir placed above the rest of system and connected to the sealed measurement downstream chamber to supply constant pressure drop. The incoming flow from downstream chamber was kept during the whole serial 2D planes capturing and leakage jet of nozzle passed into measurement upstream chamber, which was illuminated by laser sheet. Measurement upstream chamber remained exposed to the atmosphere and the outflow of it, as well as the outflow from the constant-head tank was conducted into a pooling reservoir. At last, the pooling reservoir was connected to the inlet of the pump to achieve a close hydraulic circuit. Since the tubes connection the reservoirs to chambers had a small hydraulic resistance, a negligible value of the pressure head was lost across those connections. The isolation of the outflow section of the reservoir from the incoming fluid, as provide by the baffles arrangement, guaranteed that the height of the fluid column driving the flow was constant during the measurements, thereby assuring the stationary flow. Finally, a contribution of the flow-generating system to the observed effects of valve was excluded.

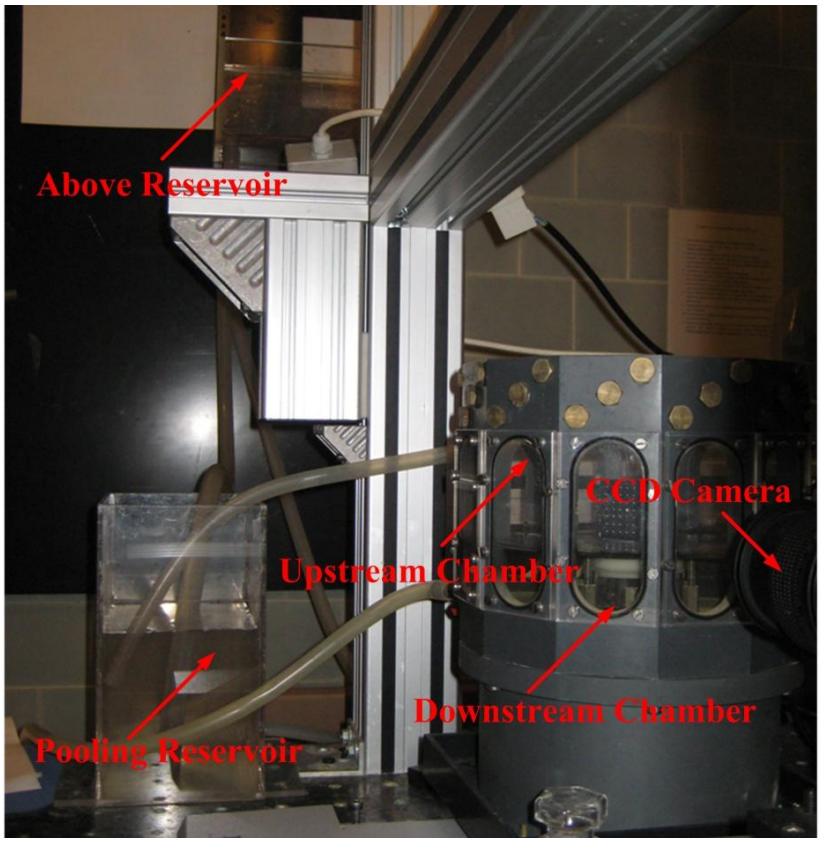

Figure 3.2: experimental flow loop system

The constant pressure head is supplied by the above reservoir. Figure 3.3 shows the structure of the reservoir with black lines representing the flow direction in the structure and red lines representing the flow direction outside of the reservoir. The flow from hydraulic pump is driven in the first section with fixed height. The flow continuously gets in the second section, with is used as constant pressure head to the target chambers. The excess fluid falls into the third section and channels to the pooling reservoir. The pooling reservoir is used as the excess fluid storage.

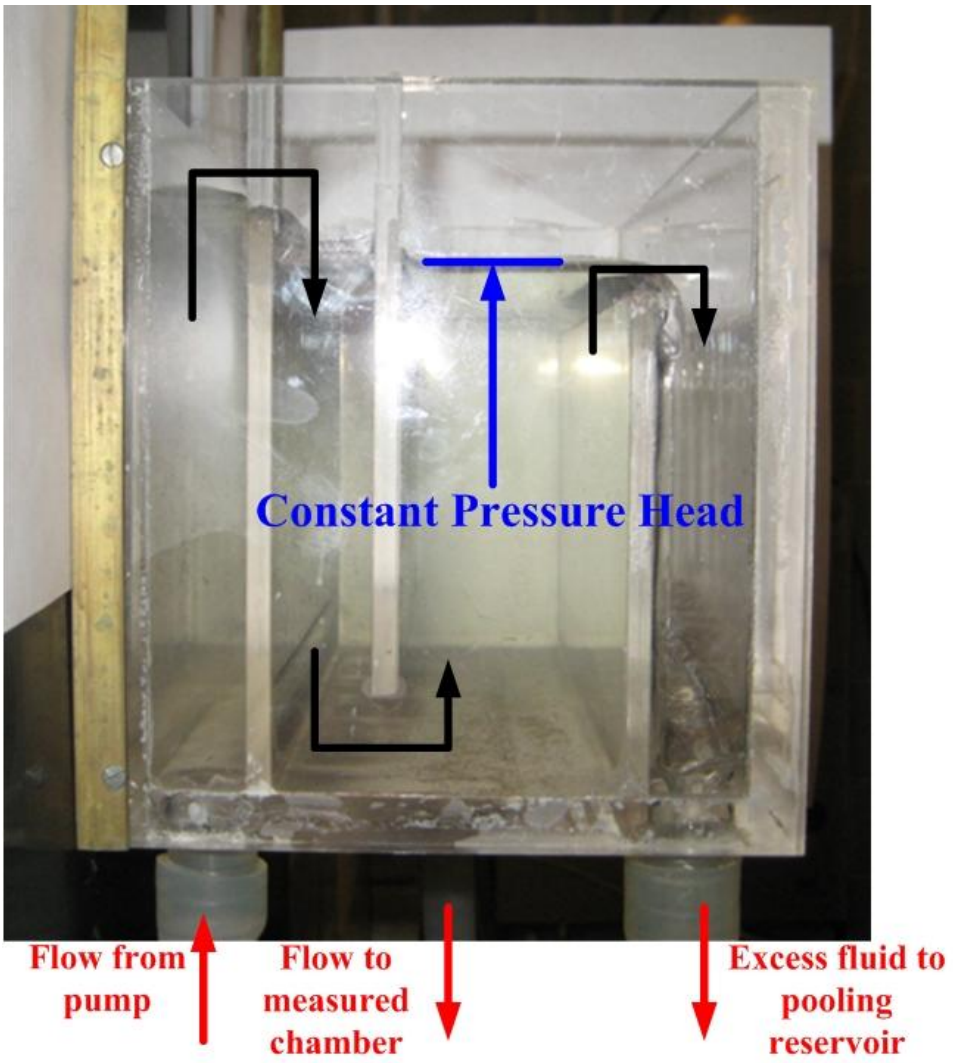

Figure 3.3: structure of above reservoir

The blood analog fluid was silicon water with a measured viscosity of 3.5cP and a density of 1.0 g/cm^3 at room temperature. To accommodate PIV measurement, the fluid was seeded with neutrally buoyant silver-coated 10 μm diameter ($\rho = 1.1 g/cm^3$) hollow glass spheres. Each flow measurement was captured by a high speed camera. A synchronizer was applied to control the laser pulses and frame acquisition of camera. In this experiment, a double frame images are

needed to be recorded for each PIV analysis to determine to displacement of particles.

The laser pulses were obtained with a commercially available dual laser pulsed PIV system. To illuminate double frame images, two Nd: YAG lasers were composed of. Each laser generated a light beam in the infrared at a 1064nm wavelength. This beam was subsequently passed through a frequency doubler that produced light at 532nm in the green region of the spectrum. The INSIGHT 3G PIV software controlled the two lasers triggered with the dual-frame image acquisition through the synchronizer. The shutter delay of camera could vary from 10 to 500 μs to provide double-frame images corresponding to each laser pulse. Beam combination optics combined with light sheet optics (cylindrical lens with a spherical focusing lens) was used to convert the two pulsed beams into pulsed light sheets with an average thickness of roughly 1 mm.

Applying a PIVCAM CCD camera, the PIV images were acquired with a resolution of 1,024*1,018 pixels and a sample frequency of 10 frames/s. A region of interest of 10mm*20mm was focused using a Nikon AF Micro-Nikkor 60mm lens.

3.1.2 CALIBRATION METHOD

To calculate average velocity field of flow, the calibration for visualized scale was required to be taken out before each measurement cycle. For calibration, the perspective of the CCD camera is supposed to correlate to the real distance on the calibration target, which is shown in figure 3.4 (a). The calibration target is composed of a serial of orderly placed calibration spots. Every two spots are separated by fixed distance 5mm. During calibration, the calibration target is placed parallel to the laser sheet on the focus of the illuminated field, which is shown as figure 3.4 (b). CCD camera captures digital images of spots on the calibration laser sheet and transmits them to PC. Figure 3.4 (c) demonstrates a single shot image of the target was saved into PC. An area of interest with laser focus on the calibration image was cut out from the whole image and this sub-image was turn into binary image through image threshold, which is shown in the Figure 3.4 (d). Further step of calibration is to determine the coordinates of the centre in the two circles and calculate the distance of y axis in pixels. In the case shown in Figure 3, the calibration of measured field is determined as below:

$$\gamma\_calibration = \frac{D_{IS}}{D_T} = \frac{5mm}{380\,pixels} = 13.2\mu m / pixel$$

The calibration scale was saved and input to Insight 3G. The PIV flow field was further calculated depending on this value.

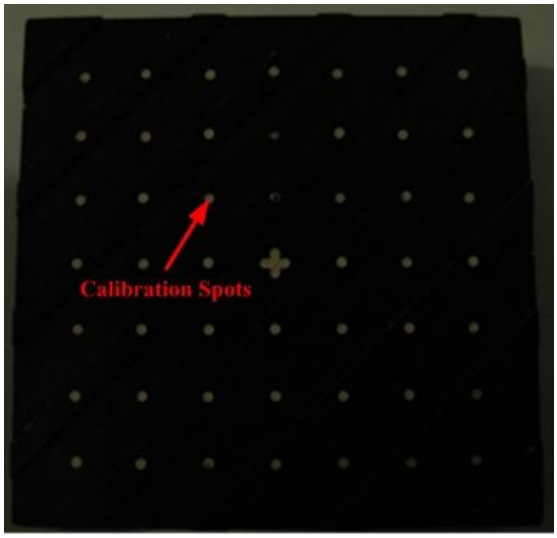

(a)

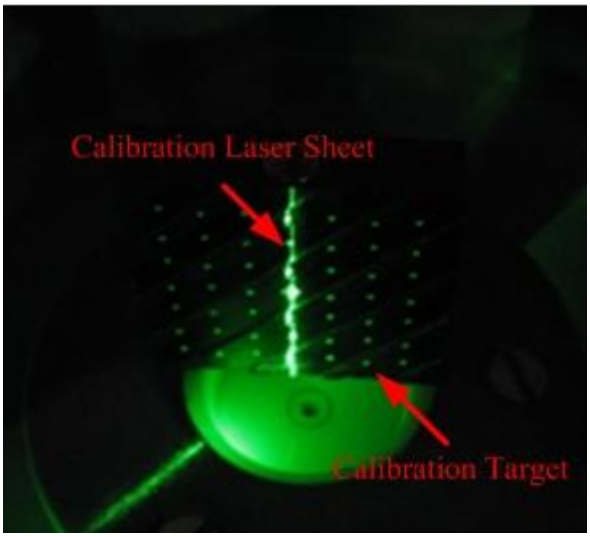

(b)

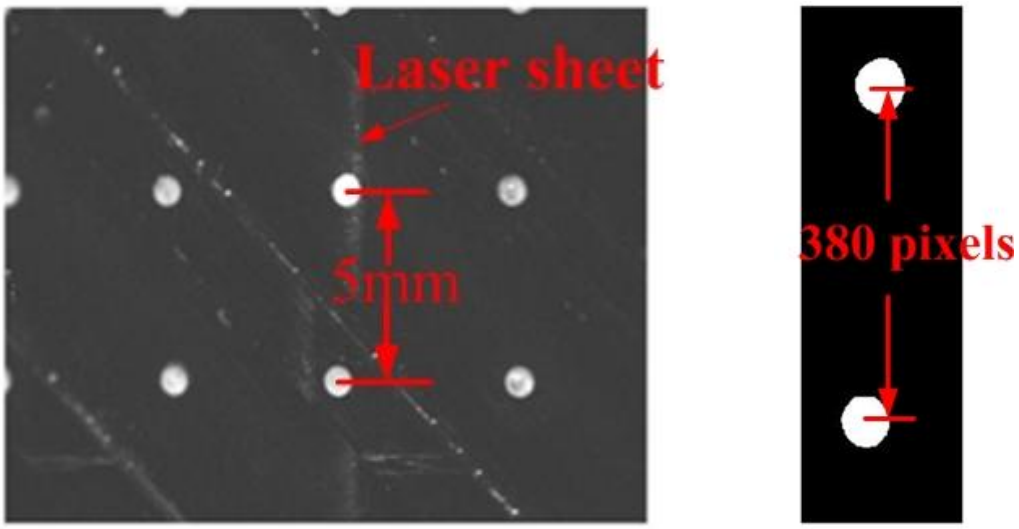

(c) (d)

Figure 3.4: Calibration of visualized field

3.1.3 NOZZLE GEOMETRY AND MEASUREMENT COORDINATES

The geometry of test nozzle is illustrated by figure 3.5 with hydraulic diameter 2mm in the throat region. The flow direction is represented by vector a. The nozzle incorporates on an incoming end with an arc chamfering in 3mm radium that gradually reduces the throat hydraulic diameter form 8mm to 2mm. The opposite end is characterized in a sudden increase of the diameter. With flow in a direction, the nozzle resembles a conical concentration and a sudden expansion.

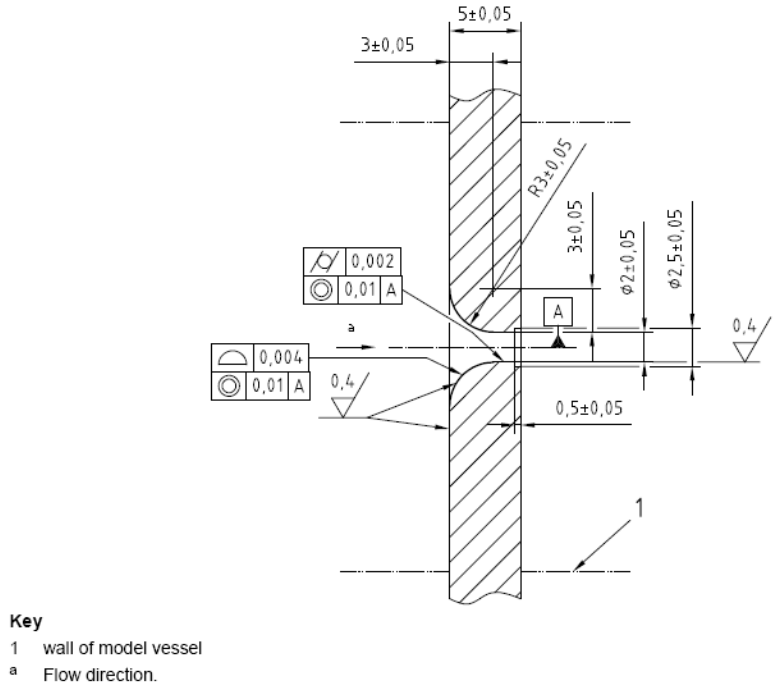

Figure 3.5: geometry of test nozzle

To obtain fully developed structure of leakage jets, the experiments in this chapter concentrate in the flow field 11mm away from the nozzle sudden expansion. The axes for the experiments are illustrated in figure 3.6 (a). The central plane of valve defined as z=0. The positive y was identified in the edge of 11mm away from nozzle expansion and into the downstream chamber. The positive x axis was defined from centre of nozzle to right side of nozzle. The scale of target x_y plane is from z=0mm to z=2mm with 0.5mm resolution. The target plane for measurements is given in figure 3.6 (b).

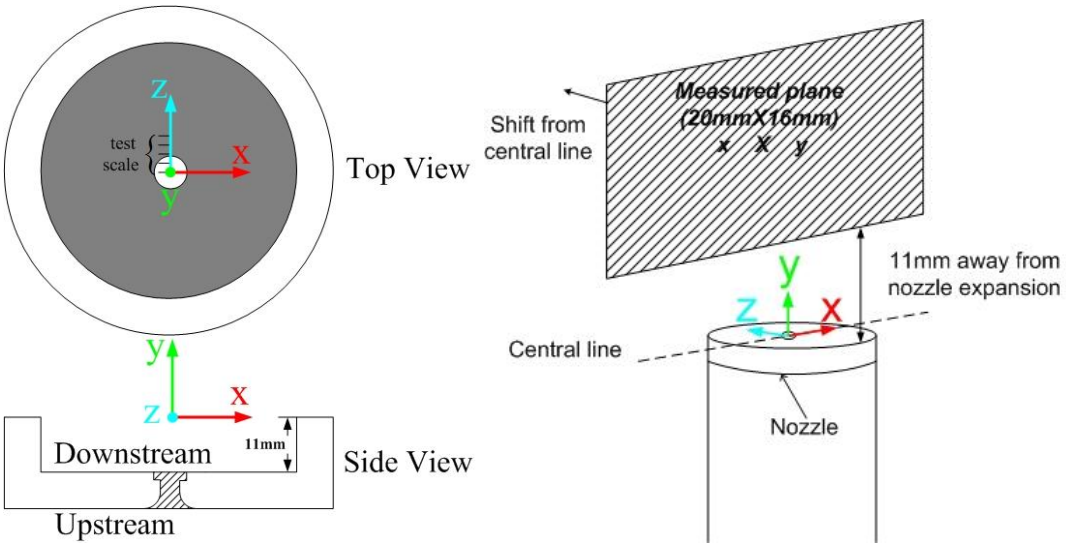

(a) (b)

Figure 3.6: (a) axis for measurement; (b) location for target plane

3.1.4 REYNOLDS NUMBER

The Reynolds number is characterized by the relative importance of inertial and viscous forces in a flow. The parameter is essential in fluid dynamics to determine the state of the flow, whether it is laminar, transition of turbulent. The momentum calculation is given as equation 2:

$$\frac{\partial}{\partial t}(\rho u_i) + \frac{\partial}{\partial x_j}\left[\rho u_i u_j + p\delta_{ij}\right] = \frac{\partial}{\partial x_j}\tau_{ij} \qquad (2)$$

The terms on the right are the inertial forces and those on the left correspond to viscous forces. If we use U, L, ρ and μ to represent the reference values for velocity, hydraulic length, density and dynamic viscosity, then the inertial force can be given as equation 3:

$$inertial\ \ force \sim \frac{\rho U^2}{L} \qquad (3)$$

And viscous force can be given as equation 4:

$$viscous\ \ force \sim \frac{\mu U}{L^2} \qquad (4)$$

The Reynolds number is usually denoted as Re and defined as the ratio of inertial force and viscous force, shown as equation 5:

$$\mathrm{Re} = \frac{inertial\ \ force}{viscous\ \ force} = \frac{\rho UL}{\mu} \qquad (5)$$

The terms of the kinematic viscosity are given as equation 6:

$$\nu = \frac{\mu}{\rho} \tag{6}$$

The Reynolds number can be finally given as equation 7:

$$\mathrm{Re} = \frac{UL}{\nu} \tag{7}$$

In this chapter, the Reynolds number is mathematically determined by controlled flow rates. The formula used in this chapter is given as equation 8:

$$\mathrm{Re} = \frac{QL}{\nu A} \tag{8}$$

Where L is hydraulic diameter (m), Q is the volumetric flow rate (m^3/s), A is the pipe cross-section area (m^2), and ν is the kinematic viscosity (m^2/s). The Reynolds number in throat area and corresponding flow rates are shown in table 3.2.

	Experiment 1	Experiment 2	Experiment 3	Experiment 4
Flow rates	3.2mL/s	5.5mL/s	8.3mL/s	11.6mL/s
Reynolds number at throat region	1600	2800	4200	5900
Flow regime	Laminar flow	Transition flow	Turbulent flow	Turbulent flow

Table 3.2: flow rates for PIV experiments with Reynolds number and flow regimes

3.2 RESULTS

In this section, the results of measurement will be presented including flow rates, the mean velocity vectors, turbulent intensity, and turbulent shear stress (TSS) at different measurement locations.

3.2.1 VELOCTY PROFILES WITH SUDDEN EXPANSION AND REPEATABILITY ANALYSIS

Laminar, transition and turbulent flow regimes ($\mathrm{Re}_{throat} = 1600, 2800, 4200, 5900$) were measured by PIV and repeatability analysis was taken in 3 different measured test. Figure 3.7 shows variations in different test locations. All velocity data were normalized with respect to the average velocity at the inlet,

$$\overline{u_{inlet}} = \frac{Q}{\pi r_{inlet}^2} \tag{9}$$

$$u_{normalized} = \frac{u}{\overline{u_{inlet}}} \tag{10}$$

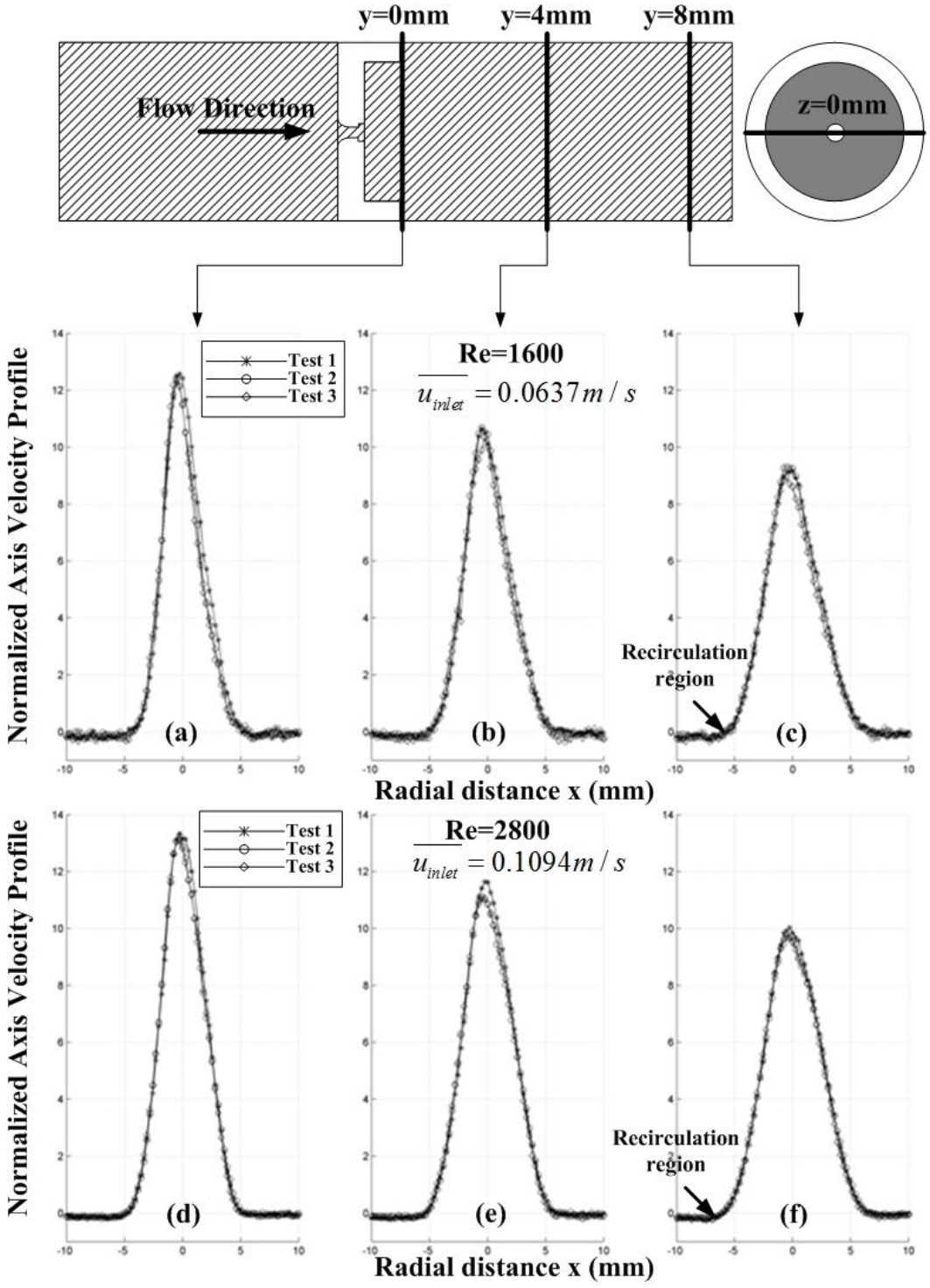

Figure 3.7: (a)-(f) velocity profiles at different downstream locations under Reynolds number 1600 and 2800

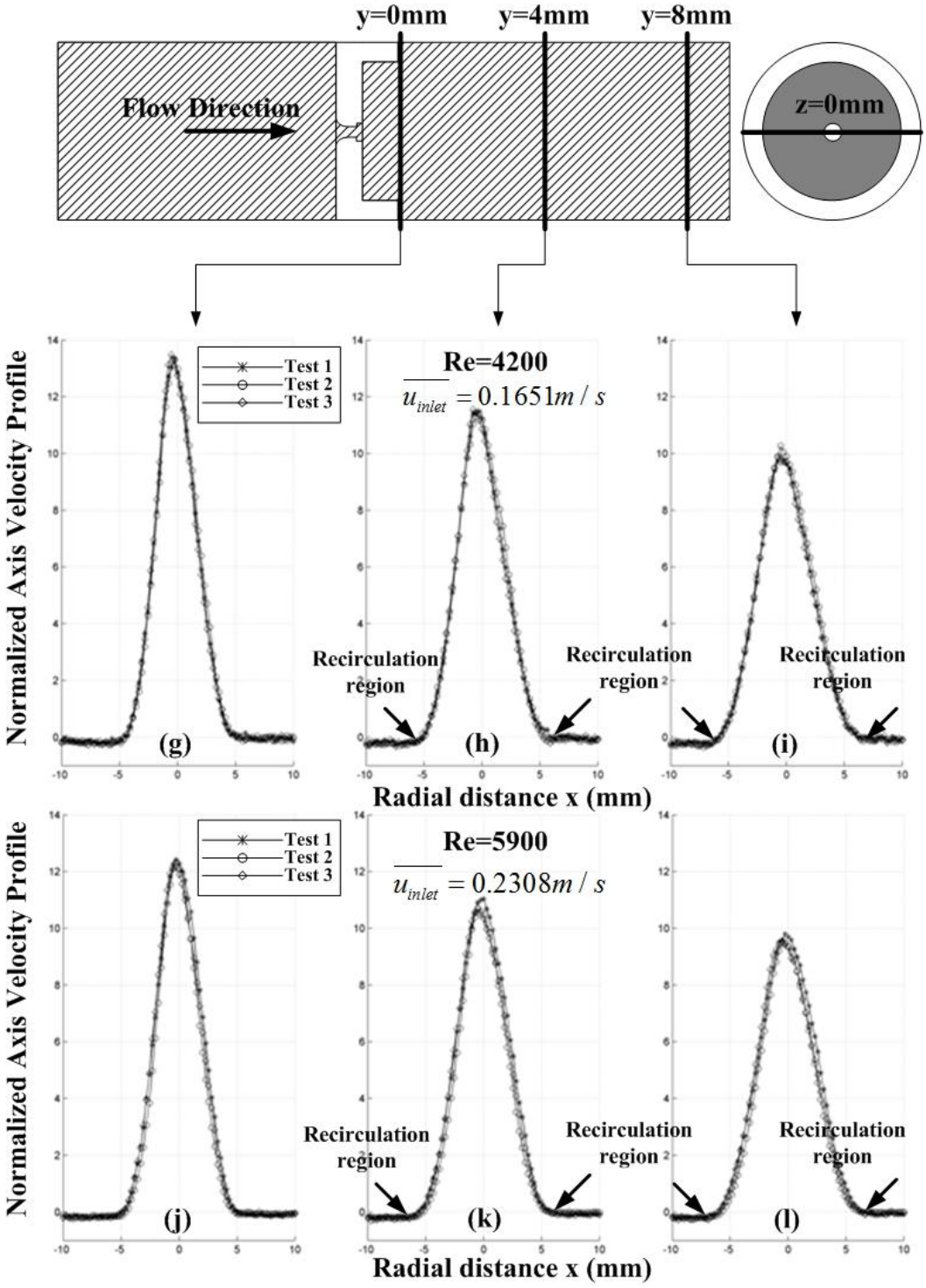

Figure 3.8: (g)-(l) velocity profiles at different downstream locations under Reynolds number 4200 and 5900

When the leakage jets exited the sudden expansion, the structure of jests formed a high speed region in the core with a low-flow recirculation zone near the wall region, which is shown in figure 3.8. In the downstream location close to sudden expansion (y=0mm), good agreements were observed with three tests throughout all flow regimes and maximum variation was less

than 1%. In contrast, maximum variations increased around 5% at distant downstream locations (y=4, 8mm). The peak velocity in the reverse eddies region was less than one-tenth of the peak velocity in the core region. Although symmetrical structure of jets was apparently observed, slightly asymmetry in the strength of the recirculation eddies still existed in figure 6 (c), (f), (h), (i), (k), (l). This is in agreement with results reported in previous study [100].

For all flow conditions, the reattached flow to the wall was observed within 20H, where H (=5 mm) is the different between the exit pipe radius and the throat radius. For the laminar and transition condition (Re=1600, 2800), the reverse flow was measured at distant downstream locations (y>8mm) with small quantities. For the turbulent conditions (Re=4200, 5900), the reverse circulation eddies were measured at locations close to the sudden expansion (y=4mm) and the values of reverse velocity were relatively large. However, the recirculation length kept in similar lever with increasing Reynolds number as the flow became fully turbulent.

To some extent, the self-similarity in our experiments was presented at same measured downstream locations for each flow regime such as the normalized velocity profiles in figure 6 (a), (d), (g), (j). Similar observations were reported by previous studies [101]-[104].

Even though the flow regimes tested were under laminar, transition and turbulent condition, the velocities measured for repeatability analysis were similar and varied less than 10%. Figure 3.9 shows the variation in centerline velocity along the axis directions.

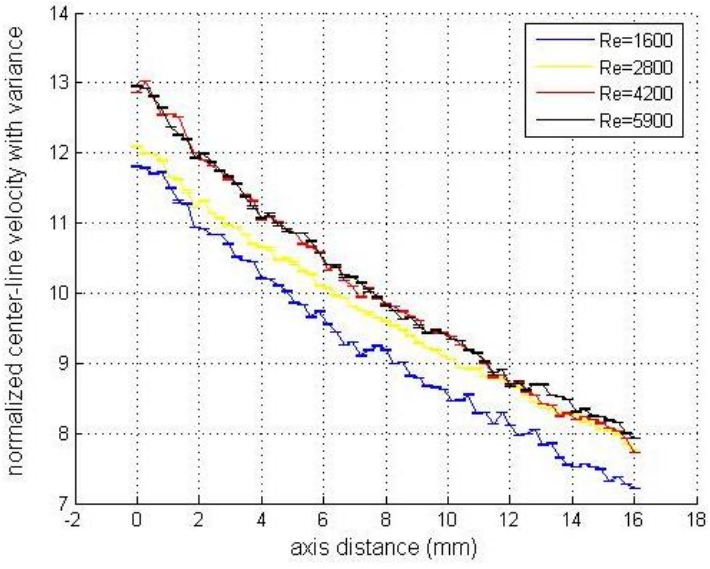

Figure 3.9: variations for three tests along axis distance

3.2.2 REPEATABILITY ANALYSIS FOR TURBULENT SHEAR STRESS

To investigate different shear stress levels corresponding to flow regimes, turbulent shear stress (TSS) calculated based on eq. 5 in chapter 2 with the unit 'Pa' was presented (figure 3.10)

under distinct throat Reynolds numbers with three tests.

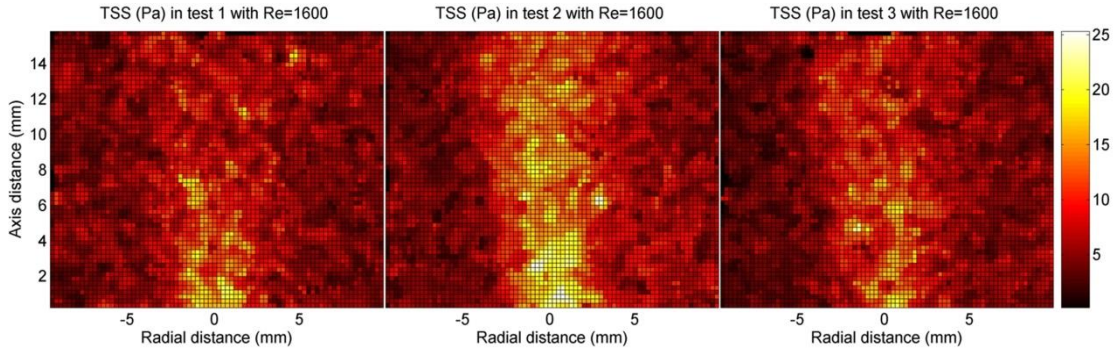

(a)

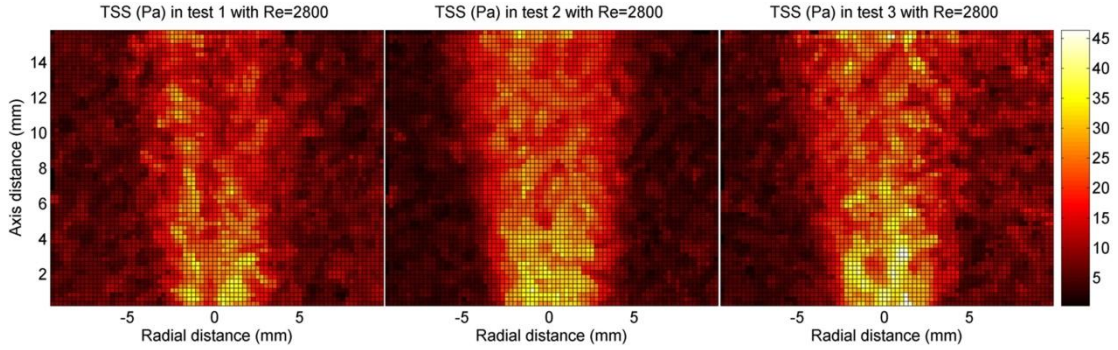

(b)

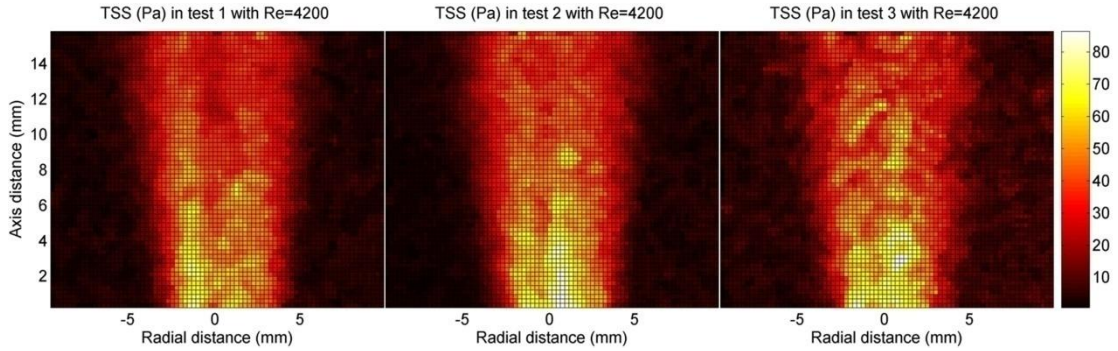

(c)

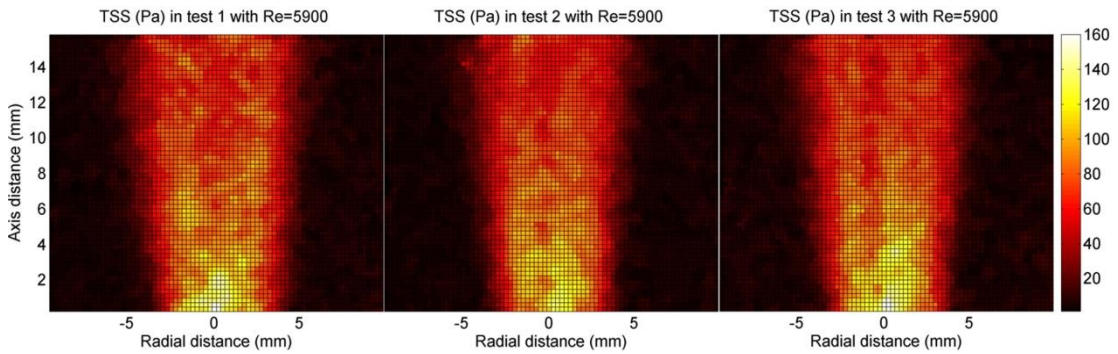

(d)

Figure 3.10: TSS distributions from PIV three tests under different Reynolds number

In figure 3.10, TSS values in 2D PIV measured planes were illustrated throughout different flow regimes. The property of TSS map distributions can be described as high values relating to the regions of high velocity gradient. Two high strength regions of TSS were observed on each

boundary of the leakage jet. This observation gave a good agreement with Boussinesq approximation theory, which is used to compute the turbulent stress tensor as the product of the kinematic eddy-viscosity and the mean strain-rate tensor. For laminar flow regime, the maximum value of TSS was around 25 Pa and the shape of the strong TSS structure did not form apparently. The structure becomes more visible with transition and turbulent flow conditions. As the strength of incoming flow increases, the magnitudes of TSS dramatically increase, especially after the turbulent flow fully developing. The peak magnitude of TSS under turbulent condition (Re=5900) reaches about 160 Pa. Additionally, slight asymmetry was observed from TSS distribution maps.

The repeatability analysis for peak magnitude of TSS was given in table 3.3. The variance for peak magnitude of TSS is much higher than that of velocity with 2%. The variance of peak magnitude decreases to 5% as the flow fully develops into turbulent regime.

	Peak TSS with Re=1600	Peak TSS with Re=2800	Peak TSS with Re=4200	Peak TSS with Re=5900
Test 1 (Pa)	21.5	40.7	82.5	158.1
Test 2 (Pa)	25.5	42.3	87.1	161.3
Test 3 (Pa)	22.2	46.7	86.9	164.6
Mean (Pa)	23.1	43.2	85.5	161.3
Variance	13.3%	15.0%	5.2%	4.4%

Table 3.3: variation analysis for TSS

3.2.3 TURNULENT SHEAR STRESSES VS. VISCOUS STRESSES

The major objective in this section is to investigate the differences between TSS and viscous stress (VS). All the magnitudes of two stress values were calculated based on 2D PIV measurements. Both of TSS and VS are second-order tensors. Thus , coordinate-independence is required to establish for comparing the magnitude according to the previous reports [105], [106].

In the figure 3.11, we presented the spatial distributions for TSS and VS under different Reynolds numbers. TSS and VS values were calculates from the average of three tests.

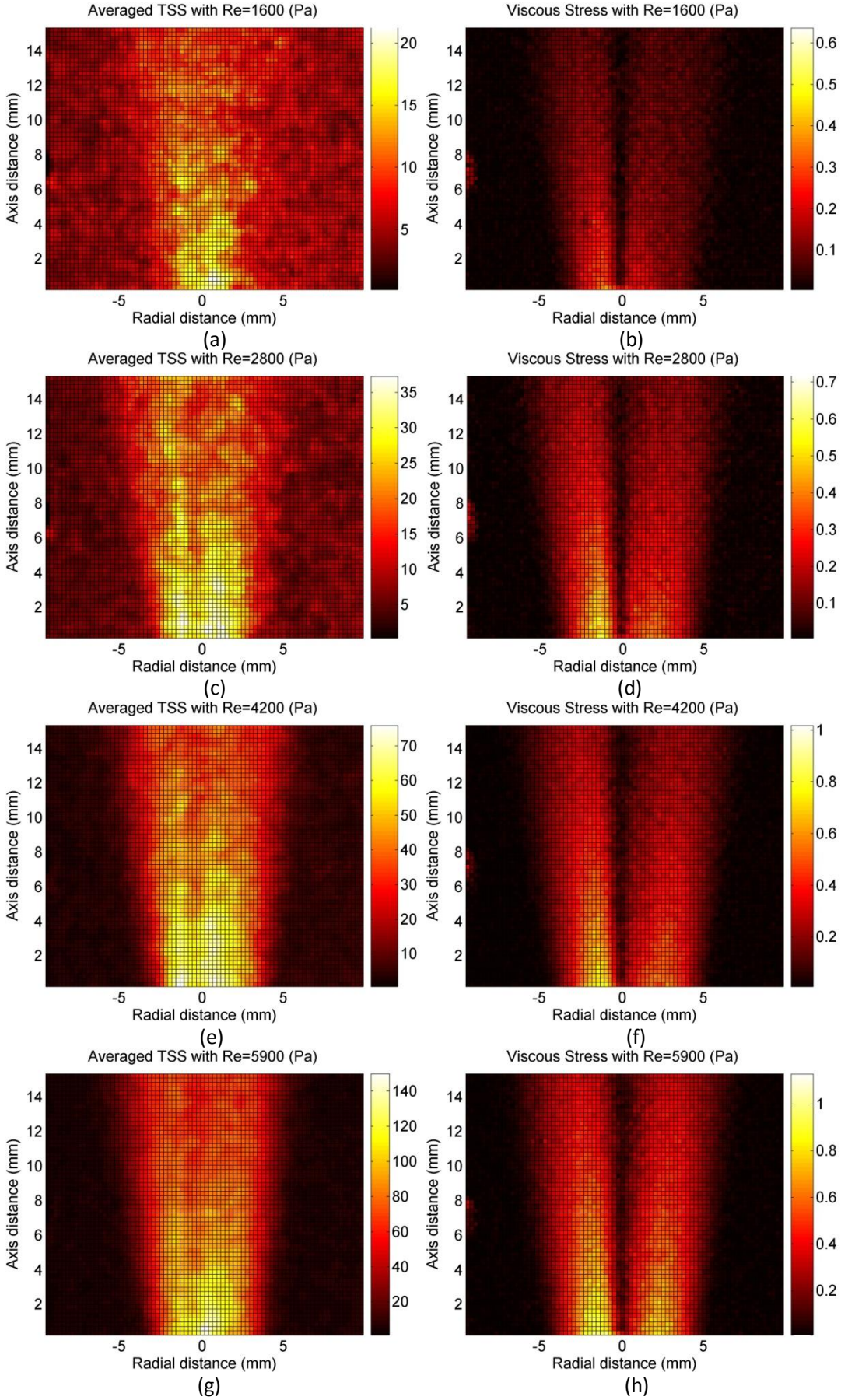

Figure 3.11: TSS vs. VS under different Reynolds number

The left column in figure 3.11 presents the TSS distribution and right column is VS distribution under same flow condition. There are drastic differences between TSS and VS distributions. The most obvious feature to describe the figure is the distinct contrast between the overall levels of TSS and VS with the former being about two orders of magnitude higher than the latter. On the contrary, the structures of high magnitude region for TSS and VS are close to each other.

Under laminar flow condition (Re=1600), the magnitude of VS is uniformly small VS< 0.5Pa and the peak value measured is about 0.6 Pa. The magnitude of TSS, on the other hand, is relatively large with peak value reaching at about 23 Pa. As the strength of incoming flow increases, the magnitude of both TSS and VS increases. However, the growth of TSS is much larger in magnitude than that of VS coursing the differences between tress metric of TSS and VS for the further growth. For the transition flow regime, the peak value of TSS magnitude increases from last flow regime by about 50%, while the peak value of VS only increases by 16%. The increase rate for TSS, in the turbulent flow regime, goes to about 100%, comparing to 40% for the increase rate of VS.

The comparison between distributions of TSS and VS is following the standard argument in the literature that TSS contributes toward cell damage.

3.3 VALIDATIONS FOR CFD

In this section, evaluations of experimental and simulation works will be made based on the comparisons of velocity profiles obtained by two methodologies under different Reynolds number accordingly.

The simulation investigation of the nozzle throat region is presented with the experimental validations. The simulation was conducted as same physical conditions as the PIV experiments. The inlet boundary condition was set as the flow rates from experimental tests relating to different flow regimes.

3.3.1 2D VELOCITY DISTRIBUTION COMPARISONS BETWEEN SIMULATION AND EXPERIMENT

The velocity distributions of PIV measurements and the CFD simulations, obtained by the same boundary conditions were evaluated and quantitatively compared to each other. Figure 3.12 shows the results of 2D measured planes under different flow regimes and we focus on the flow dynamics investigation in the mid-plane of the leakage jets.

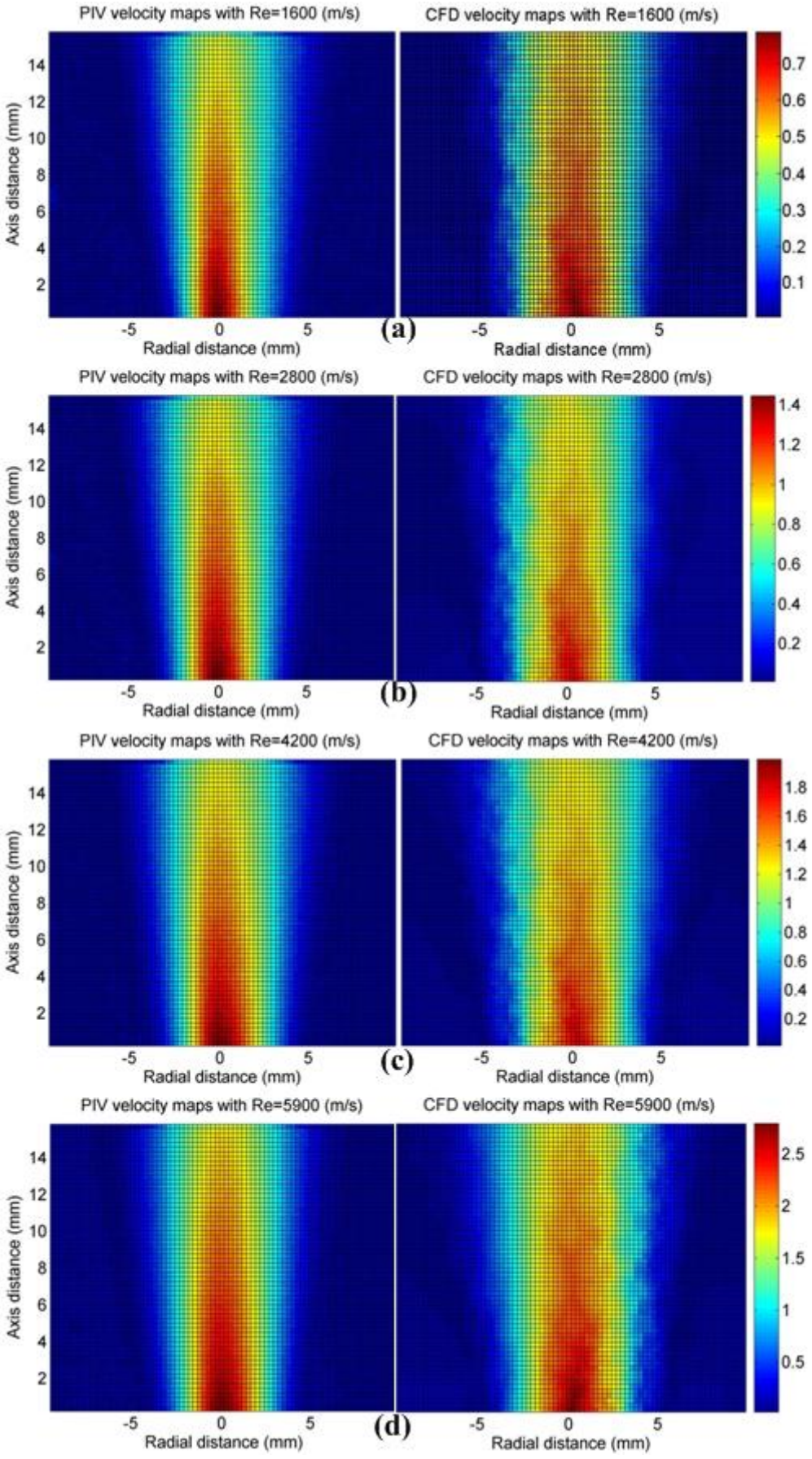

Figure 3.12: Velocity distributions comparisons between PIV and CFD

The left column in figure 10 presents the velocity distribution from PIV and the right column is from CFD simulation. The results show the in plane 2D velocity magnitude ranging from blue to red corresponding low and high velocities.

Throughout all the flow regimes, it can be noticed that the velocity magnitude of leakage jets obtained by PIV maintains a higher value than that of the CFD results. This might be due to the used simulation model laminar and k-omega, which use standard settings for turbulence intensity and turbulence length for incompressible flow. Figure 3.12 (a) shows velocity distributions obtained by two methodologies under laminar flow regime. The peak value was observed about 0.75m/s for both results. However, the structure of leakage jet obtained from CFD is boarder than that of PIV results. This might be due to the insufficient mesh solutions in CFD simulations. As the flow regime goes to transition and turbulent flow regimes, both of levels of velocity magnitude from PIV and CFD dramatically increases. As the flow develops fully turbulent, the peak value reaches about 3m/s, shown in figure 3.12 (d).

Figure 3.13 shows the variances of velocity magnitude between PIV and CFD along axis distance at multiple distances with different Reynolds number.

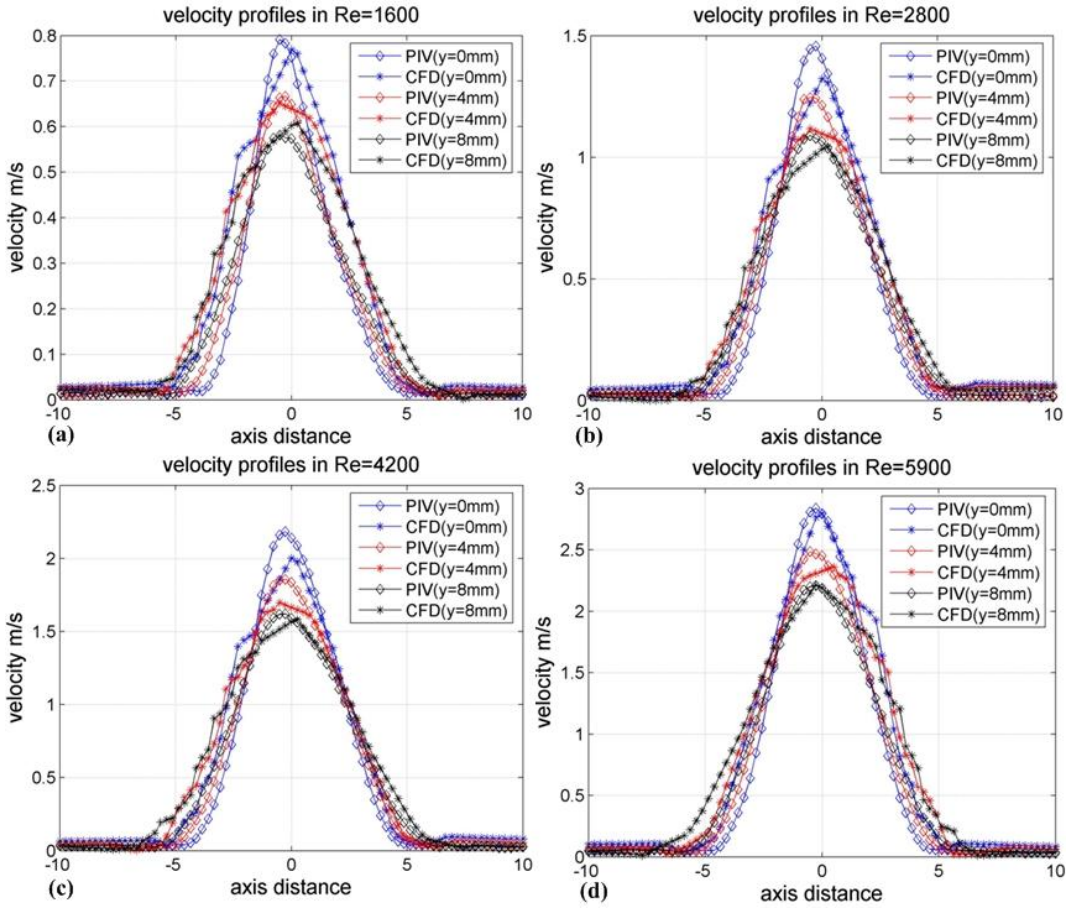

Figure 3.13: velocity profiles from PIV and CFD at multiple locations with different Reynolds number

It is noticed that the disagreement between PIV and CFD velocity profiles decreases as the flow regime goes to turbulence. In summary, the variations of peak magnitude of velocity are less than 5% for all detected locations throughout all flow regimes. Since the results from CFD have a good agreement with experimental basis, it is a possible to use the simulation results to continuously investigate the throat region of nozzle mode, where is hard to be measured with PIV. Figure 3.14 shows the velocity distribution obtained by CFD simulation with different Reynolds number.

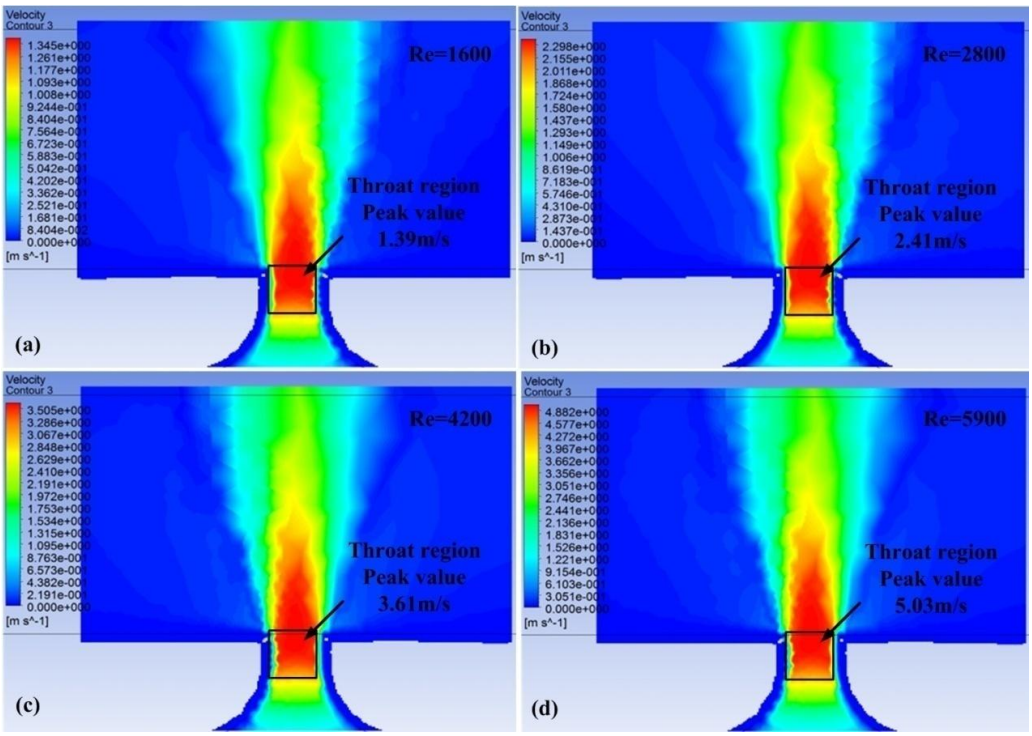

Figure 3.14: Nozzle throat regions from CFD

The Reynolds number in the throat region can be calculated by simulation data to verify the values determined by the experimental flow rates. We make hypothesis that the throat region of nozzle model is fully developed pipe. Thus, the mean velocity can be viewed as half of the peak values. The table 3.4 gives the Reynolds number from CFD comparing to the values from PIV experiments.

	Flow regime 1	Flow regime 2	Flow regime 3	Flow regime 4
Flow rates (PIV)	3.2mL/s	5.5mL/s	8.3mL/s	11.6mL/s
Re_{throat} (PIV)	1600	2800	4200	5900
V_{mean_throat} (CFD)	0.7m/s	1.2m/s	1.8m/s	2.5m/s
Re_{throat} (CFD)	1551	2696	4044	5632

Table 3.4: Reynolds number in throat region by CFD and PIV

The results show the good relationship between CFD and PIV for determination of Reynolds number.

3.4 CONCLUTIONS

In this chapter, PIV experiments were conducted with optimum setups for nozzle tests. The fluid dynamics from four flow regimes with laminar, transition and turbulence were investigated. From repeatability tests, the experimental data was proved to be reliable as an experimental basis for CFD simulations. CFD simulations were conducted with same geometry with experimental nozzle model and same physical boundary conditions. The results of CFD simulation were verified with experimental data and good agreements were observed. On the other hand, CFD data was used to investigate the velocity distributions at throat region, where is not transparent for PIV measurements. Furthermore, the Reynolds number at throat region had good correlations between two menologies.

The analysis of fluid dynamics of nozzle gives a good solution to investigate the complex flow domain in medical devices by combining experimental and simulation methodologies.

Chapter 4

PIV Multiple-Experimental Analysis of Prosthetic Heart Valves

Prosthetic heart valves are widely used to replace disease heart valves throughout the world and the most commonly implanted prosthetic valve design is bileaflet mechanical heart valves (BMHVs) owing to their good long-term durability and superior bulk flow properties. However, despite their widespread applications, the implantation of BMHVs is still not complication-free and may introduce potential damage for blood components such as hemolysis, platelet activation and thromboembolic events. Clinical reports acknowledge that these complications are associated with the fluid stressed imposed by non-physiologic nature of the flow induce by the valve, particularly in its hinge recess and near hinge region. The earliest research focusing on red blood cells (RBCs) and platelets damages derived from 1960s. When blood cells transported through BMHV s, they were impacted by pressure and shear stress as well as friction forces from their interaction with solid surfaces. The shear stress has been reported as a major source of mechanically induced RBC damage [107].

In order to test in silicon in vitro BMHVs, several equipments/computational methods are used. In particular, pulse duplicators (PDs) for testing heart valves have been designed and built according to different concepts [108][109]. Actually, PDs have been usually developed in order to allow more visibility to the forward phase with respect to the backward phase; nevertheless, the latter phase has been recognized as very important in the inception of thrombogenic phenomena. In mechanical heart valves a certain amount of regurgitant flow is a desirable option, since it provides washout of the hinges: it must be underlined that if blood particles are trapped in low-velocity regions, aggregation phenomena could be started, ultimately leading to thrombosis of the valve. Thus, regurgitation in mechanical valves is meant to maintain the valve surfaces clean of blood deposits; on the other hand, regurgitant-flow jets can have detrimental effects on blood, due to flow-related stresses in mechanical valve' hinge wash out as well as in the malapposition during TAVI procedure.

The purpose of this chapter was to improve the knowledge about near-hinge regurgitant flow dynamics of typical BMHVs. A Particle Image Velocimetry (PIV) investigation was carried out on currently marketed BMHVs, by measuring the 2D flow field at serial planes encompassing the

plane of the two distal hinges. The properties of flow field of leakage were evaluated as average velocity field, Turbulent Intensity (TI), Turbulent Shear Stress (TSS). To verify the repeatability of the results, multiple experiments were carried on at different times under same experimental conditions. Comparisons of multiple experimental results allowed us to perform an error analysis, which is critical for CFD validation. Furthermore, the blood damage predictions from the CFD simulations will be performed in TuCN [110] and the results as well as the PIV validation of the CFD results will be presented in next chapter.

4.1 EXPERIMENTAL TARGETS

4.1.1 VALVE TYPE 1

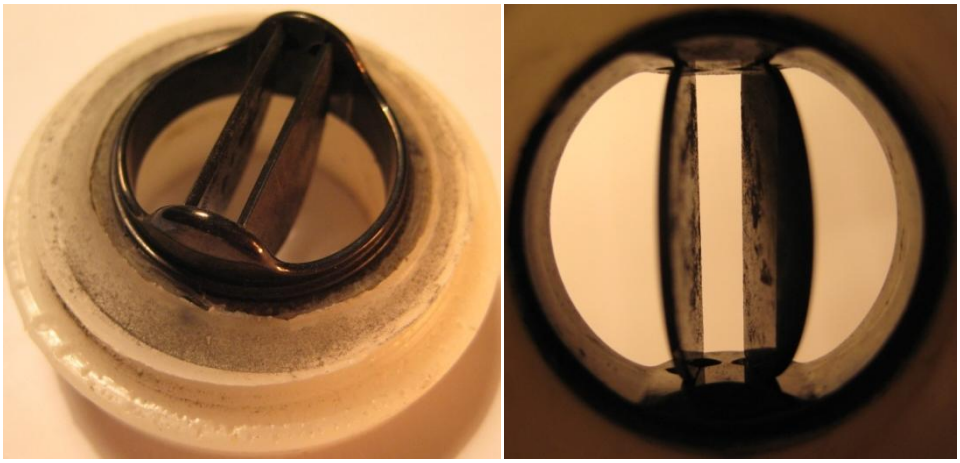

(a) (b)

Figure 4.1: target valve type 1

Type: Bileaflet; aortic, mitral and tricuspid. The valve type 1 (Fig. 4.1 a–b) was introduced clinically in 1977 [111], while the Expanded series was introduced in March 1996 (USA). The type 1 of valve is available with mounting diameters of 17–31 (aortic), 17–31 (mitral) and corresponding orifice diameters of 14.7–26 mm (aortic and mitral) [111]. Overall open height is 8.4–12.2 mm for all aortic and mitral SJM bileaflet valves [112].

Symmetric and relatively nonturbulent flow properties are concluded in vitro experimental studies for valve type 1 [111]. In vivo tests for valve type 1 mean pressure gradients range from 3.0 to 5.2 mm Hg in the aortic position and from 1.4 to 7.0 mm Hg in the mitral position [113]. Regurgitant volume ranges from 7.6 to 10.6 cm^3/stroke for aortic valves and 4.3 to 6.4 cm^3 /stroke for mitral valves [113].

The valve housing and leaflets are constructed of graphite coated with pyrolytic carbon. Leaflet hinge configuration is a butterfly-like depression and pivot guards are upright. The sewing cuff is made of polyester PET or PTFE [112].

The valve housing is made of pyrolytic carbon and is radiolucent in the standard model. The leaflets are visible in the fully open position as radiopaque lines.

A small number of valve type 1 (15- 20 out of 9514) were reported with a loss of structure integrity, including one incident of post-operative leaflet dislodgment [114]. Thromboembolism was reported as the most common nonstructural of the valve type 1 with rate of 2.0 events per pty for aortic valves and 2.5 events per pty for mitral valves [114]. Rates of anticoagulation-related complications in patients with SJM valves were reported as 2.2/pty (n = 14,845) for aortic valves and 1.7/pty (n = 16,679) for mitral valves [114]. For bileaflet valves obstruction of valves is not a critical threat with a rare rate for thrombus or pannus but life-threatening complication should be regarded for artificial implantation. The rate of pannus formation on valve type 1 has been quoted as 0.03–0.14%, and pannus is more likely to be seen on valves in the mitral or tricuspid position (n = 18,523 pty) [115]. Acute prosthesis thrombosis is mostly a complication of inadequate anticoagulation, more specifically poor patient compliance, but has been related to pannus formation [116]. Infective endocarditis is a risk for all types of prosthetic valves, and rates for target valve type 1 are reported as 0.2–0.4 cases per patient year [114].

4.1.2 VALVE TYPE 2

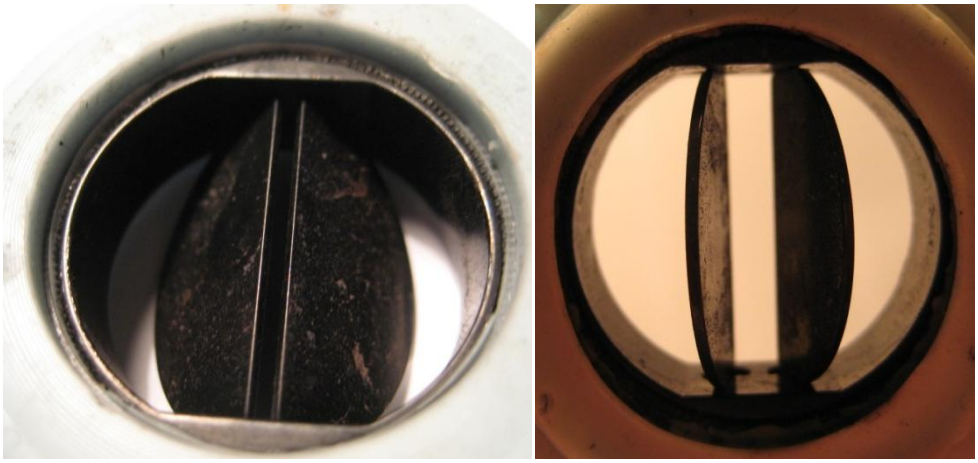

(a) (b)

Figure 4.2: target valve type 2

Figure 4.2 shows the models of target valve type 2 (bileaflet valves with aortic and mitral models). This type of valves was firstly introduced in 1986. The leaflet pivot is designed to allow thorough washing of the hinge mechanism but incomplete ‘‘wiping’’ of the hinge surfaces [115]. According to the design, the valve type 2 is intra-annularly implanted. The typical size for mitral

valve is designed 21mm for intra-annular or intra-atrial implant. Its small size and placement position makes it possible for the surgeon to use a prosthesis that is one size larger than would be permissible with an intra-annular valve [117]. This advantage of valve type 2 is especially is useful for patients with a small aortic root. Based on its ‘‘one size-up’’ feature this model is believed to provide a potential increase in valve flow area along with a reduction in pressure gradients [118].

The all available sizes and dimensions for valve type 2 are: 19-31mm for aortic valves and 23-33mm for mitral valves. Pediatric-Small Adult aortic valve sizes range from 16 to 19 mm and mitral from 16 to 21 mm.

Pyrolite is chosen as martial for valve type 2. A titanium ring surrounds the valve housing and allows rotation of the valve for optimal orientation after implantation [115]. In open state, the angle of the two leaflets is 78^{o} from the horizontal axis. Compared to other valves, the valve discs of the target valve type 2 seats closer to the edge of the housing. In the aortic position both discs of the valve type 2 open uniformly and remain in the open position during systole [119].

Higher rates of static leak have reported for valve type 2 when compared to other valves [114]. Early mortality rates for valve type 2 were reported approximately 5% [119] [120]. Linearized rates of complications reported by Fiane et al. [119] (n = 4040 pty) and Dalrymple-Hay et al. [121] (n = 4342 pty) were major thromboembolism at 0.9%/pty and 2%/pty, valve thrombosis at 0.2%/pty and 0.14%/pty, and prosthetic valve endocarditis at 0.1%/pty and 0.18%/pty, respectively. The incidence of paravalvular leak needing reoperation was reported as 0.5%/pty by Fiane et al [119].

4.2 EXPERIMENTAL SETUPS

In this section, the details of experiments concerning in leakage jets of heart valve will be described. Fluid analog used in flow system was stilled-water for the worst situation analysis. Figure 4.3 shows the structure of measurement chamber and axis for measuring. In order to supply insight into the performances of valve regurgitation, a custom-built physical model of the regurgitant phase was designed to standardize the test. The design of the model aimed at obtaining a free optical access to the regurgitant jets exiting the valve, in order to apply several 2D and 3D anemometric techniques (LDA, PIV). This model (see Fig.4.3 a) can be regarded as a 12-face prism. The optical glass window minimized optical distortion of the laser sheet and prevented damage induced by the transmission of the high-energy light sheet. To eliminate the

boundary influences on the regurgitant jets, the design of the 12-face prism model was given a relatively large diameter 195mm (shown in Fig.4.3 b) and resembled a sudden expansion to the exit of the prosthetic valves, which were seated coaxially with the model. The height of the prism model was 85mm. The valve seat was sealed with an upstream chamber, the diameter of which was 45mm (see in Fig.4.3 b). The axes used for measurements as well as results presentation are illustrated in Fig. 4.3 (c). The hinge recess plane of valve was defined as Z=0mm and the acquisitions of PIV measured planes were a serial of parallel planes from Z=0mm to Z= 6mm, results of which were presented in subsequent analysis. The positive x-axis was measured from the central plane between leaflets (B-datum plane) into right side of valve. The y-axis was measured from the top of valve housing with the direction along the regurgitant flow. Optical access provided flow field measurements on the upstream side as close as 4 mm from the actual valve seat or the top of valve housing.

Table 4.1 shows the experimental setups in detail. Table 4.2 illustrates the laboratory conditions. The details of parameters of PIV components and flow loop system were demonstrated in chapter 2 and chapter 3.

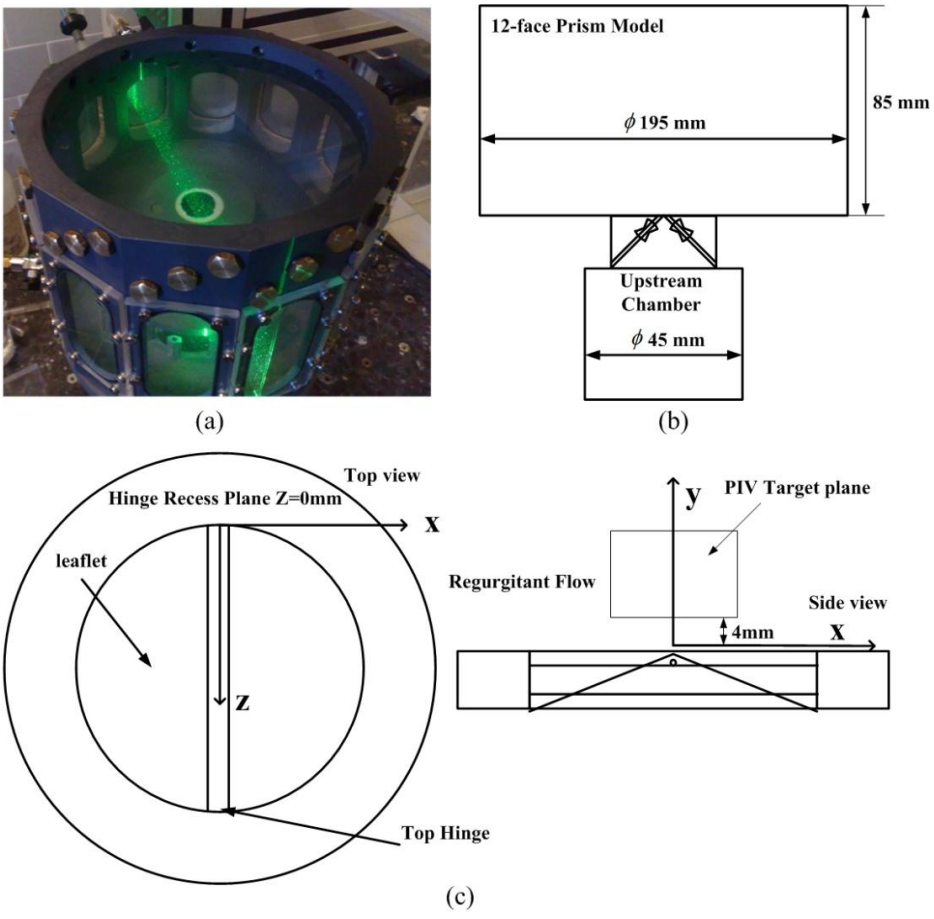

Figure 4.3: (a) 12-face prism model (b) geometry of the model (c) axis definition of measurements

Constant pressure drop	Flow density	Flow dynamics viscosity	Experimental temperature
75 mmHg	1.0 g/cm3	1cp	25 $^{\circ}C$

Laser sheet thickness	Pixel resolution	Interrogation window size	PIV resolution
<1mm	16.2 μm	32by32	0.25mm

Δt between images	Maximum particle displacement	Particle density	Number of image pairs
100 μs	<5 pixels	10 particles /interrogation	1000

Table 4.1: Experimental parameters

PIV system	PIV processing software	CCD Camera	CCD pixels
Lab conditions	INSIGHT 3G (TSI,Inc., Shoreview,MN)	PIVCAM 13-8	1024*1018

PIV system	Lens	Synchronizer	Laser generator
Lab conditions	Nikon AF Micro-Nikkor 60mm lens	TSI model 610034	Double_pulsed Nd:YAG laser

Table 4.2: Specifications for PIV system used by laboratory

4.3 RESULTS AND DISCUSSIONS

4.3.1 FLOW RATE TESTS

To supply the experimental condition for inlet flow, flow rates for two types of valves in five tests were measured under 75mmHg pressure drop. The table 4.3 shows the flow rates in five tests and the average flow rate was 3.29mL/s for type 1 and 9.44mL/s for type 2.

	Test 1	Test 2	Test 3	Test 4	Test 5	Average
Flow rate (type 1)	3.29mL/s	3.28mL/s	3.31mL/s	3.26mL/s	3.33mL/s	3.29mL/s
Flow rate (type 2)	9.47 mL/s	9.34mL/s	9.53mL/s	9.48mL/s	9.40mL/s	9.44mL/s

Table 4.3: flow rate tests under 75mmHg pressure drop

4.3.2 VELOCITY DISTRIBUTIONS OF LEAKAGE JETS AND REPEATABILITY TESTS

4.3.2.1 PIV RESULTS FOR VALVE TYPE 1

The velocity visualizations were presented as two-dimensional color maps with magnitude values of velocity. For clarity, leaflets and hinges were illustrated on the plots. Four leakage jets were observed from corresponding hinge corners. The figure 4.4 presents the velocity maps on the peak value plane (z = 2mm) from five tests and the last figure was taken from the average of five tests. The structures of velocity distribution were comparable from five repeatability tests. The B-datum plane was relatively free of leakage because of the closure and seal together of the leaflets. The figure 4.4 shows the geometry of the bileaflet valve on the bottom that the pressure gradient drove both leaflets to the valve seat and along the periphery between the leaflets and valve housing. The geometry of the bileaflet valve caused the seal to be tight near the B-datum plane region, and no significant leakage could be observed. The weakening seals between hinge and leaflets were demonstrated and four separate leakage jets were observed in figure 4.4. The critical regions were reserved close to downstream corners and captured peak velocity magnitude of strong leakage jets was around 0.7m/s. The other two weaker leakage jets with peak velocity magnitude 0.3m/s were observed from upstream corners.

Figure 4.5 shows the velocity profiles at downstream locations y=0mm, 2mm, 4mm, 6mm from multiple experiments on the measured plane z=2mm, where the peak value was captured. The red line represented average velocity profile, which will be used to validate the results from simulation works. The areas of high velocity were symmetrically located at x= -3, 3mm, where the fluid reached a peak velocity of approximately 0.7 m/s at downstream location y=4mm. The peak velocity near the upstream corners of hinge was relatively low, in the range of 0.3 to 0.5 m/s and was observed at downstream location y=2mm. Good agreements between multiple experiments were illustrated at downstream location y= 0, 2, 4mm in figure 4.5 (a) - (c) and misalignments were observed at y= 6mm in figure 4.5 (d) due to the gradually decreased SNR.

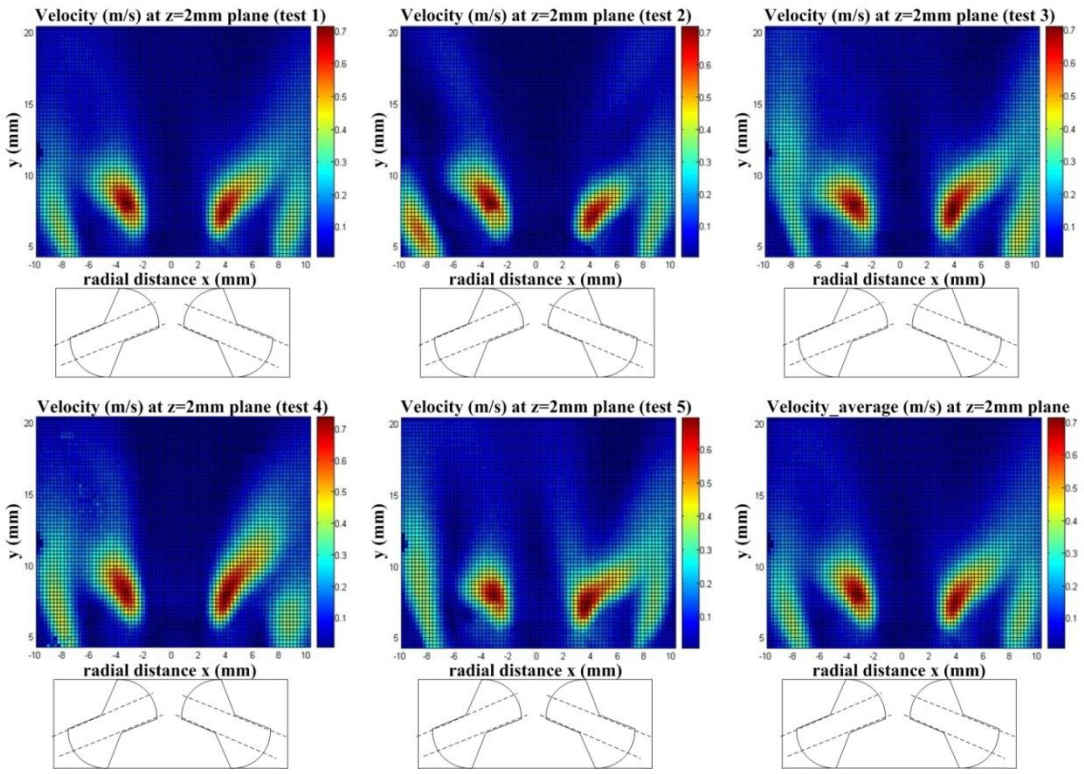

Figure 4.4: velocity maps on peak value plane from 5 tests and average velocity distribution

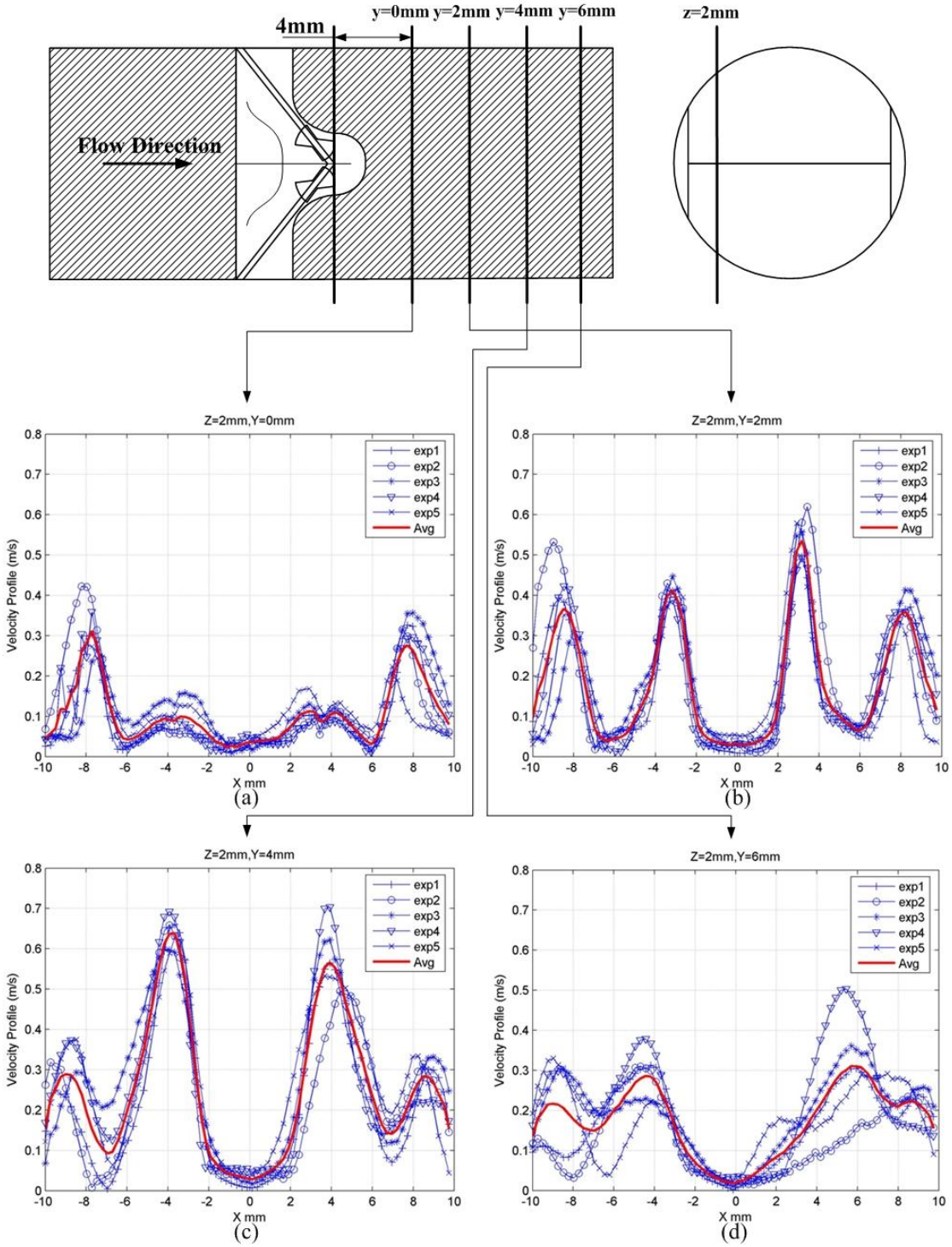

Figure 4.5: Peak velocity profile from repeatability tests and average peak velocity profile based on 5 tests for valve type 1

To verify the results of experimental measurements, five tests were taken under same experimental conditions and the repeatability analysis was carried out. The velocity distribution maps for each 2D scanned plane were displaced for five repeated tests in Appendix 1.1.1, 1.2.1 1.3.1, 1.4.1. The profiles for different downstream locations with seven tests were plotted in Appendix 1.1.2, 1.2.2, 1.3.2, 1.4.2 and the red line represented average velocity profile, which will be used to validate the results from simulation works. The values of peak velocity from multiple experiments were demonstrated in table 4.4. The measured planes Z=3, 4 mm gave a high velocity region with magnitude value about 0.66m/s. In contrast, velocity magnitude was relatively low at plane z= 2, 5mm with value about 0.55m/s. The maximum variations were around 10% due to slight differences of leaflet displacements during each close behavior. The repeatability tests were proved that PIV could supply a reliable experimental basis for simulation verifications.

	Z=2mm	***Z=3mm***	***Z=4mm***	***Z=5mm***
Test 1 (maximum velocity m/s)	0.5378	0.6784	0.6449	0.6211
Test 2 (maximum velocity m/s)	0.5365	0.6591	0.7107	0.5724
Test 3 (maximum velocity m/s)	0.5309	0.6518	0.6430	0.5453
Test 4 (maximum velocity m/s)	0.4808	0.6833	0.6906	0.6232
Test 5 (maximum velocity m/s)	0.5694	0.6510	0.6496	0.6274
Mean velocity (m/s)	0.5311	0.6647	0.6678	0.5979
Coefficient of variation	6.01%	2.28%	4.63%	6.18%

Table 4.4: repeatability analysis of peak velocity for valve type 1

4.3.2.2 PIV RESULTS FOR VALVE TYPE 2

The same repeatability tests are presented in the form of color pictures in Figure 4.6, which illustrate the flow fields on the measured plane Z=3mm from five tests and the averaged velocity distributions in the last figure. The peak value of velocity magnitude is about 0.7m/s on the measured plane Z=3mm. Only one emerged leakage jet can be observed from each side of hinge. The leakage jet from B-datum plane is much weaker than the leakage jets from hinges.

The captured peak values of velocity magnitude are 0.56m/s, 0.68m/s, 0.67m/s, 0.61m/s corresponding to the target plane Z=2, 3, 4, 5mm.

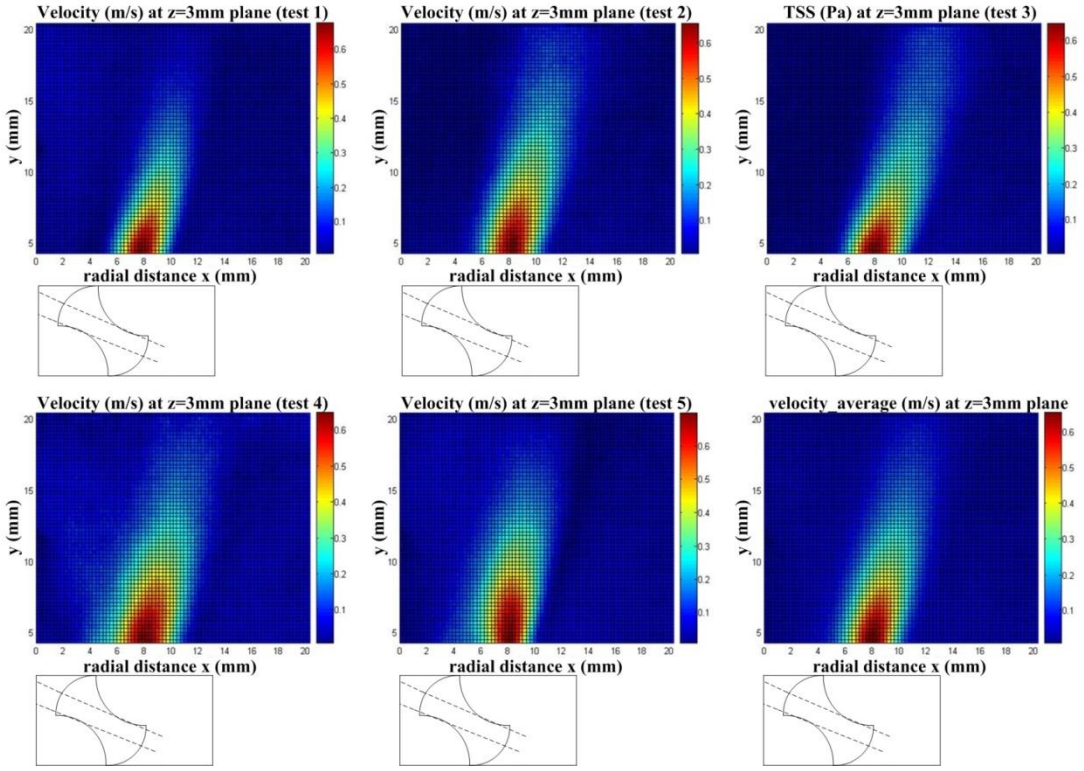

Figure 4.6: velocity maps on peak value plane from 5 tests and average velocity distribution

Figure 4.7 shows the velocity profiles for valve type 2 at downstream locations y=0mm, 2mm, 4mm, 6mm from multiple experiments on the measured plane z=3mm, where the peak value was captured. The red line represented average velocity profile, which will be used to validate the results from simulation works in the next chapter. The areas of high velocity were located at x= 8mm on each side of valve, where the fluid reached a peak velocity of approximately 0.7 m/s at downstream location y=0mm. The peak magnitude of velocity decreased from 0.7m/s to 0.4m/s from downstream location y=0mm to y=6mm. Good agreements between multiple experiments were illustrated at downstream location y= 0, 2, 4, 6mm in figure 4.7 (a) - (d).

To verify the results of experimental measurements, five tests were taken under same experimental conditions and the repeatability analysis was carried out. The values and locations of peak velocity from five tests were demonstrated in table 4.5. The variation was around 5%. The repeatability tests were proved that PIV could supply a reliable experimental basis for simulation verifications.

The velocity distribution maps for each 2D scanned plane were displaced for five repeated tests in Appendix 2.1.1, 2.2.1 2.3.1, 2.4.1. The profiles for different downstream locations with

seven tests were plotted in Appendix 2.1.2, 2.2.2, 2.3.2, 2.4.2 and the red line represented average velocity profile, which will be used to validate the results from simulation works.

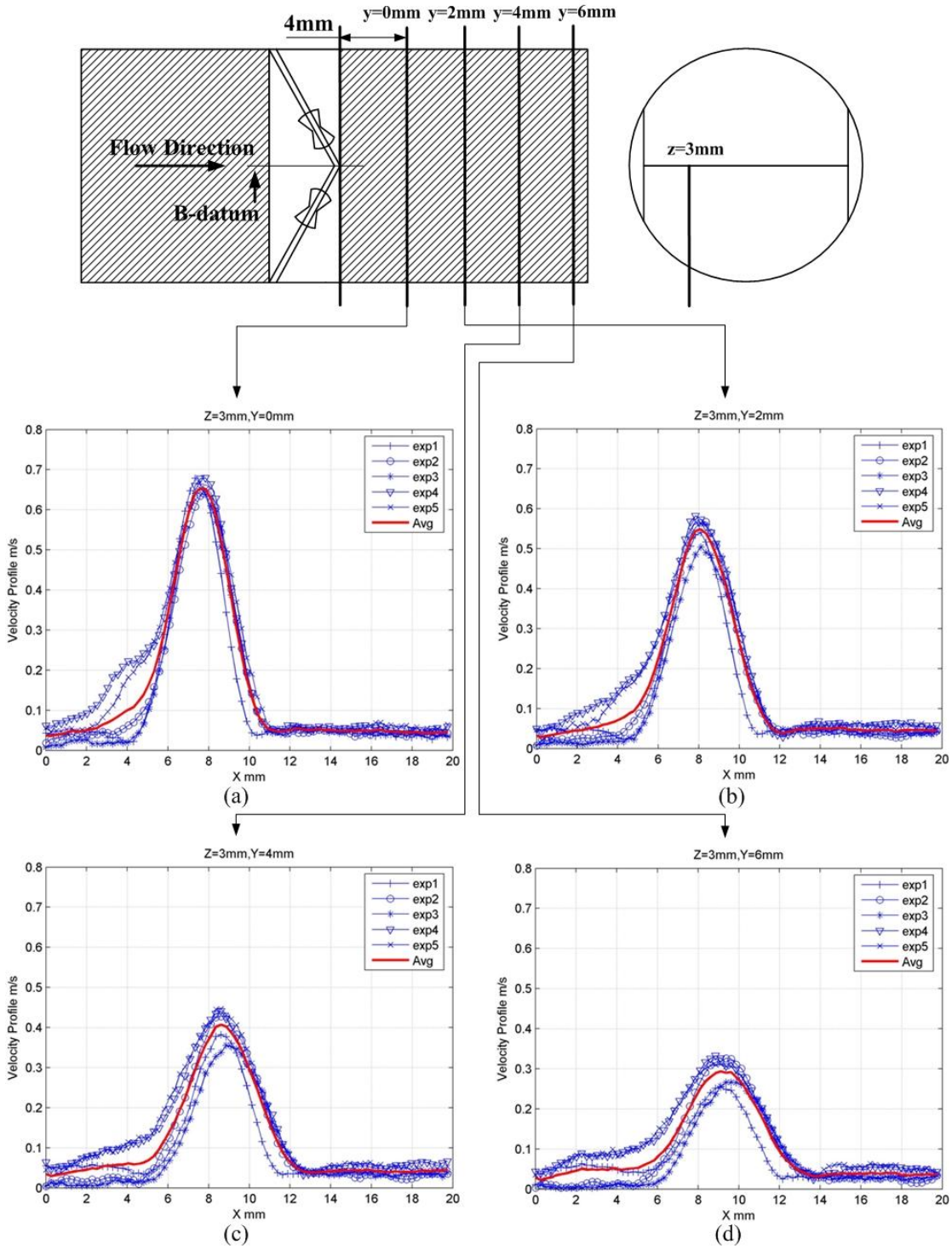

Figure 4.7: Peak velocity profile from repeatability tests and average peak velocity profile based on 5 tests for valve type 2

	Z=2mm	*Z=3mm*	*Z=4mm*	*Z=5mm*
Test 1 (maximum velocity m/s)	0.5378	0.6784	0.6449	0.6211
Test 2 (maximum velocity m/s)	0.5309	0.6518	0.6430	0.5453
Test 3 (maximum velocity m/s)	0.5694	0.6510	0.6496	0.6274
Test 4 (maximum velocity m/s)	0.5788	0.7024	0.7122	0.6322
Test 5. (maximum velocity m/s)	0.5669	0.7018	0.6958	0.6380
Mean velocity (m/s)	0.5568	0.6771	0.6691	0.6128
Coefficient of variation	3.79%	3.75%	4.85%	6.24%

Table 4.5: repeatability analysis of peak velocity for valve type 2

4.3.2.3 3D REGURGITANT FLOW PATTERN FOR TWO VALVE TYPES

Three-dimensional visualized leakage jets based on serial two-dimensional measurements were illustrated in figure 4.8-4.9 Velocity maps on different measured planes revealed similar flow patterns and good correlations. The peak values of velocity for valve type 1 were located on z=2mm plane and the peak values of velocity for valve type 2 were located on z=3mm plane.

In the bileaflet valves, central regurgitation along the B-datum plane is much less than that occurring from the hinge points of the leaflets, as illustrated in figure 4.8-4.9 The typical normal pattern features multiple jets arising from the leaflet hinge points, which generate a converging pattern when viewed in planes parallel to the leaflet axes; in the plane orthogonal to the leaflets axis, these normal jets appear to diverge. Depending on the orientation of the plane, either these jets arise peripherally and converge or their origin is projected on the center of the valve and they exhibit a diverging V pattern.

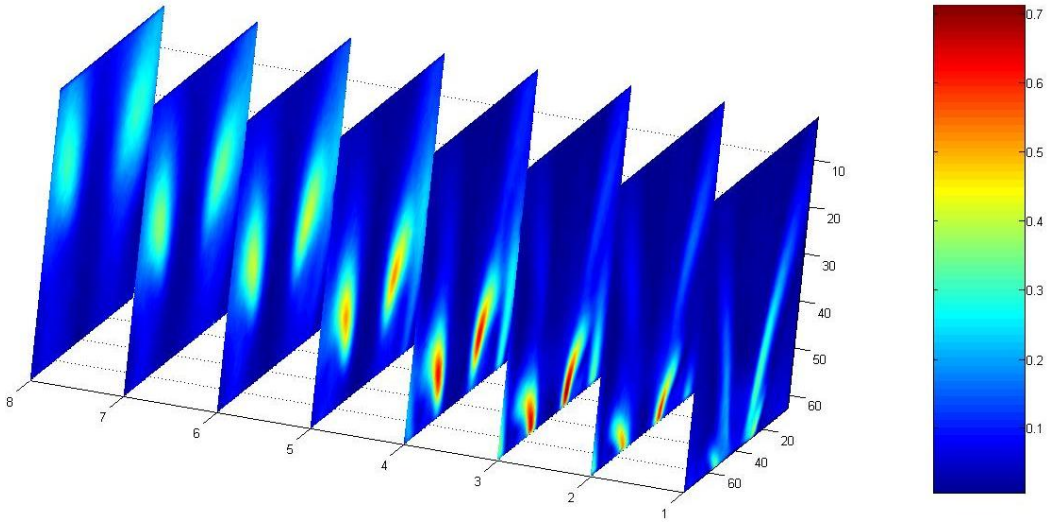

Figure 4.8: 3D Regurgitant flow field reconstruction by means of 2D measurement for valve type 1

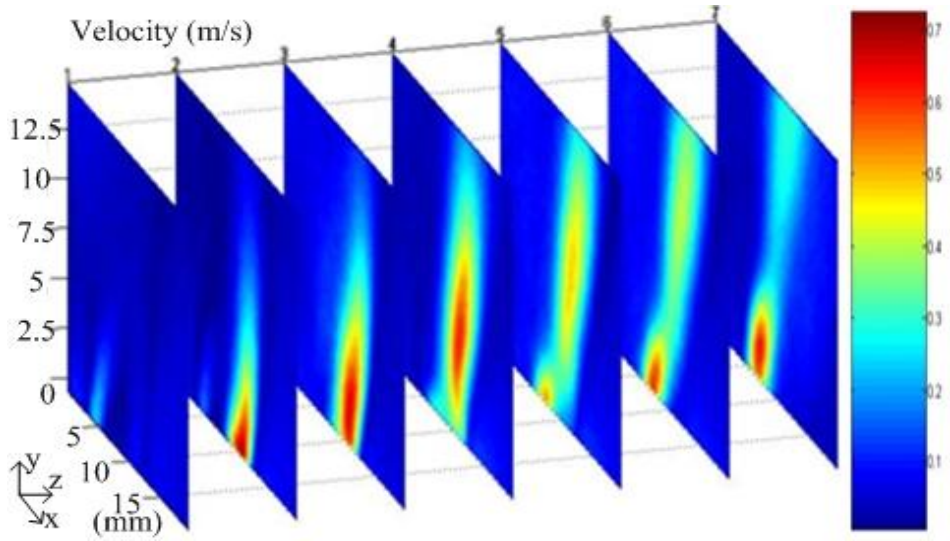

Figure 4.9: 3D Regurgitant flow field reconstruction by means of 2D measurement for valve type 2

4.3.3 TSS_MAXIMUM DISTRIBUTIONS OF LEAKAGE JETS AND REPEATABILITY TESTS

4.3.3.1 MAXIMUM TURBULENCE SHEAR STRESS (VALVE TYPE 1)

The maximum TSS existing in leakage jets were calculated according to equation (5) in chapter 2. The peak values were observed on measured plane z=2mm and these results had a consistency in five tests. Figure 4.10 shows TSS results at same location in five tests and the last figure was average TSS distributions extracted from five tests. The results from five tests had well correlations. The captured peak value for TSS was approximately 40 Pa and high risk regions were located in leakage jets from the corners of hinges.

Fig. 4.11 illustrates averaged TSS distributions on different measured planes from z=1mm to z=4mm. The peak values of maximum TSS were 35 Pa, 39 Pa, 17 Pa and 15 Pa respectively on

each measured plane. The high risk regions were consistently observed in leakage jets of hinge corners on different planes.

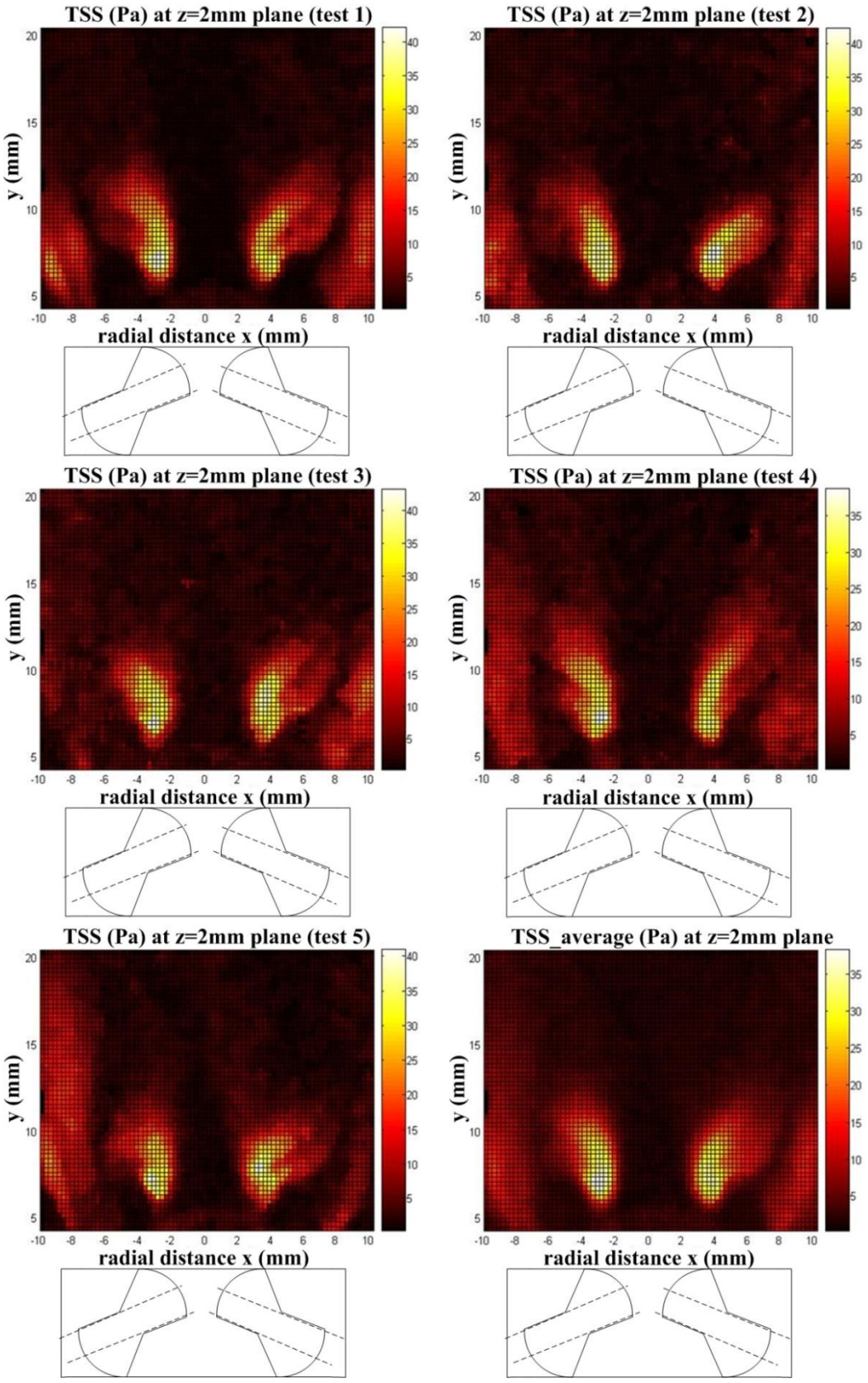

Figure 4.10: maximum TSS from 5 tests and average TSS distribution on plane z=2mm

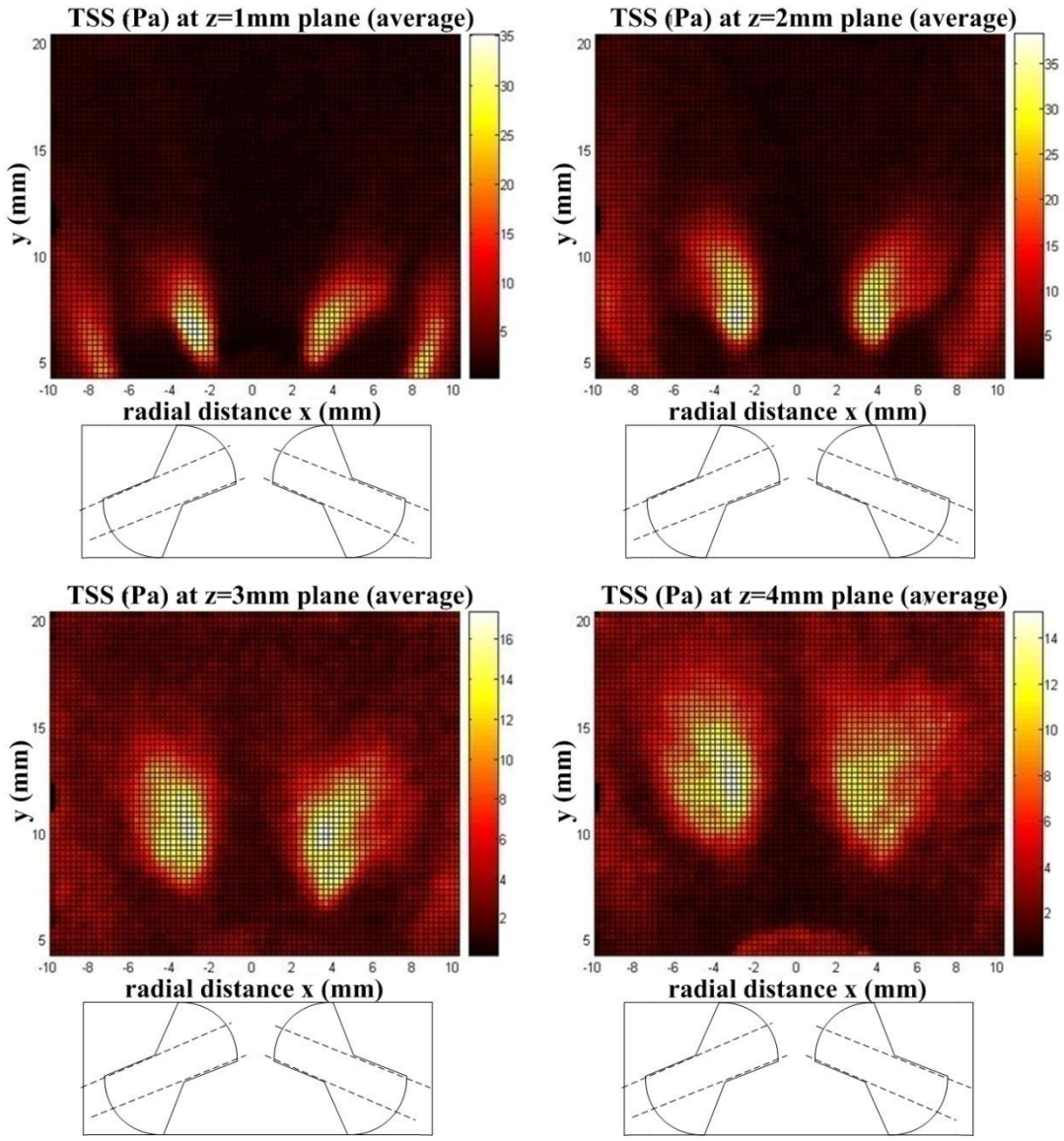

Figure 4.11: Averaged maximum TSS distributions on a serial of planes

The maximum TSS profiles calculated from five tests were illustrated in figure 4.12 and red line was the average profile based on five tests. The peak values in five tests were listed in table 5.6 and the coefficient of variation was 4.26%. The repeatability analysis verified a reliable experimental basis for numerical simulations and the simulation works will cooperated with TuCN in Romania, the results of which will provide data in the regions where experiments cannot measure. The multiple experimental results (valve type 1) for TSS distributions on serial planes were illustrated in Appendix 1.1.3, 1.2.3, 1.3.3 and 1.4.3.

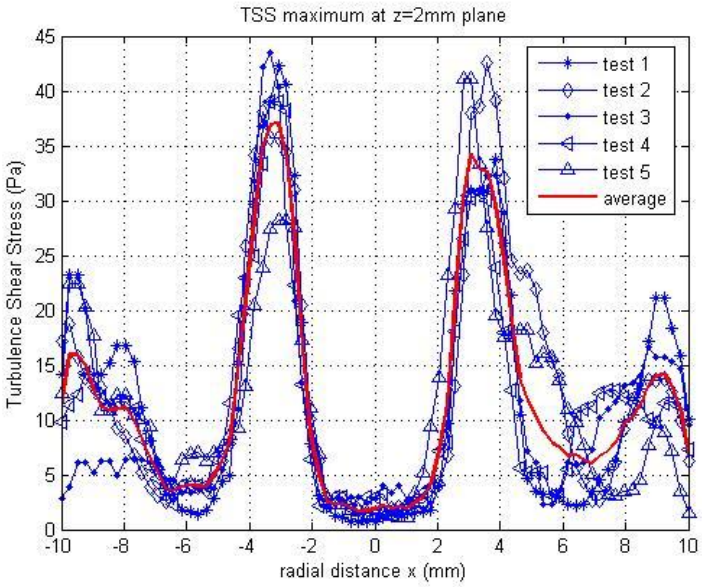

Figure 4.12: Peak TSS profiles from repeatability tests and average peak TSS profile based on 5 tests

	Peak TSS (Pa)	Location Coordinates (x y z) (mm)
Test 1	42.3	(-3.0,7.4,2)
Test 2	42.6	(3.8,7.4,2)
Test 3	43.5	(-3.3,7.1,2)
Test 4	38.9	(3.0,7.2,2)
Test 5	41.1	(3.3,8.2,2)
Average	41.7	
Coefficient of variation	4.26%	

Table 4.6: peak TSS values from five tests and repeatability analysis

4.3.3.2 MAXIMUM TURBULENCE SHEAR STRESS (VALVE TYPE 2)

Figure 4.13 shows TSS results of target valve type 2 at same location in five tests and the last figure was average TSS distributions extracted from five tests. The TSS 2D distribution was proved repeatable through multiple experimental tests. The captured peak value for TSS was approximately 20 Pa and high risk regions were located in leakage jets from the corners of hinges.

Figure 4.14 illustrates averaged TSS distributions on different measured planes from z=2mm to z=5mm. The peak values of maximum TSS were 18 Pa, 20 Pa, 14 Pa and 12 Pa respectively on each measured plane. The high risk regions were consistently observed in leakage jets of hinge corners on different planes.

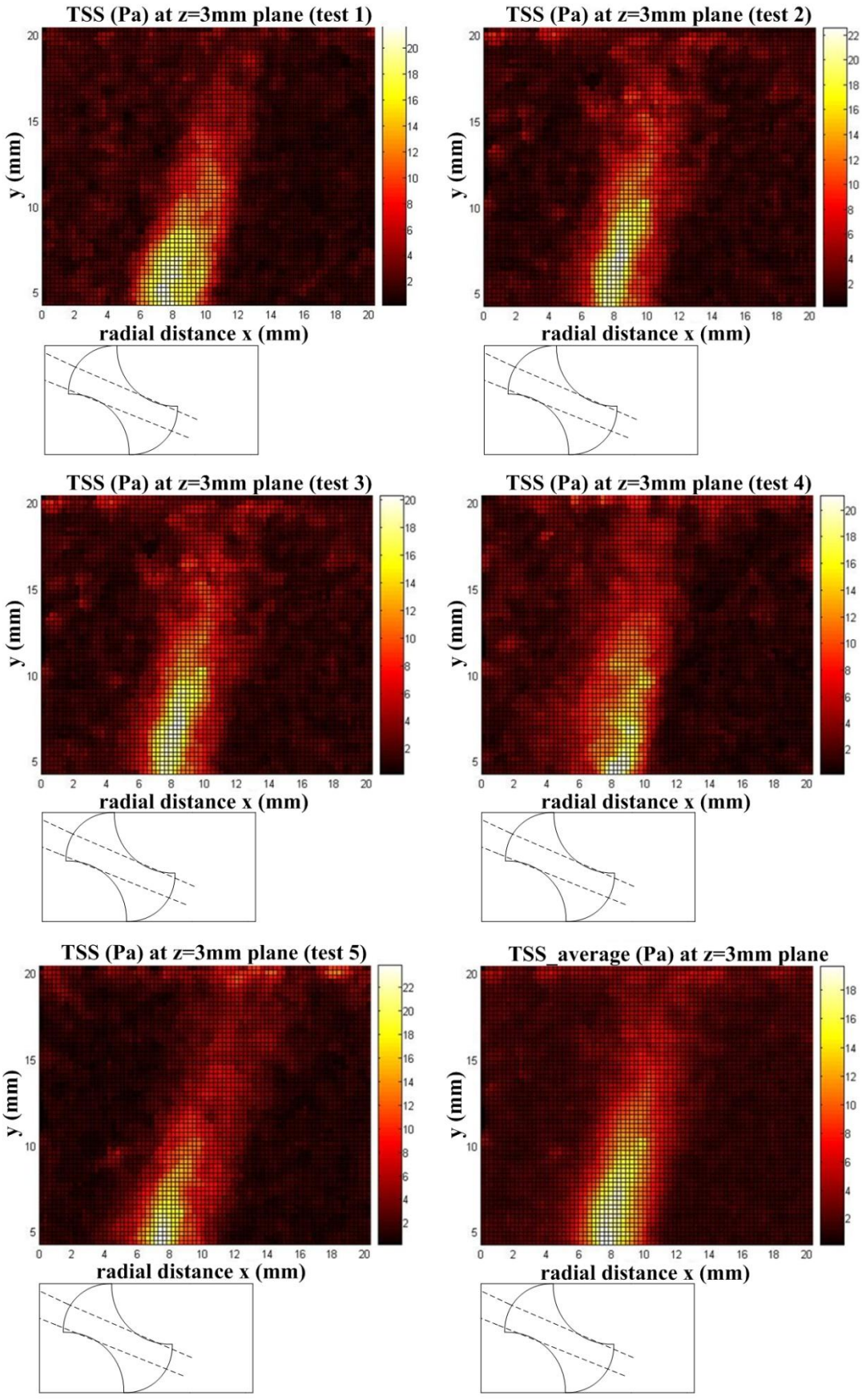

Figure 4.13: peak TSS from 5 tests and average TSS distribution on plane z=3mm (valve type 2)

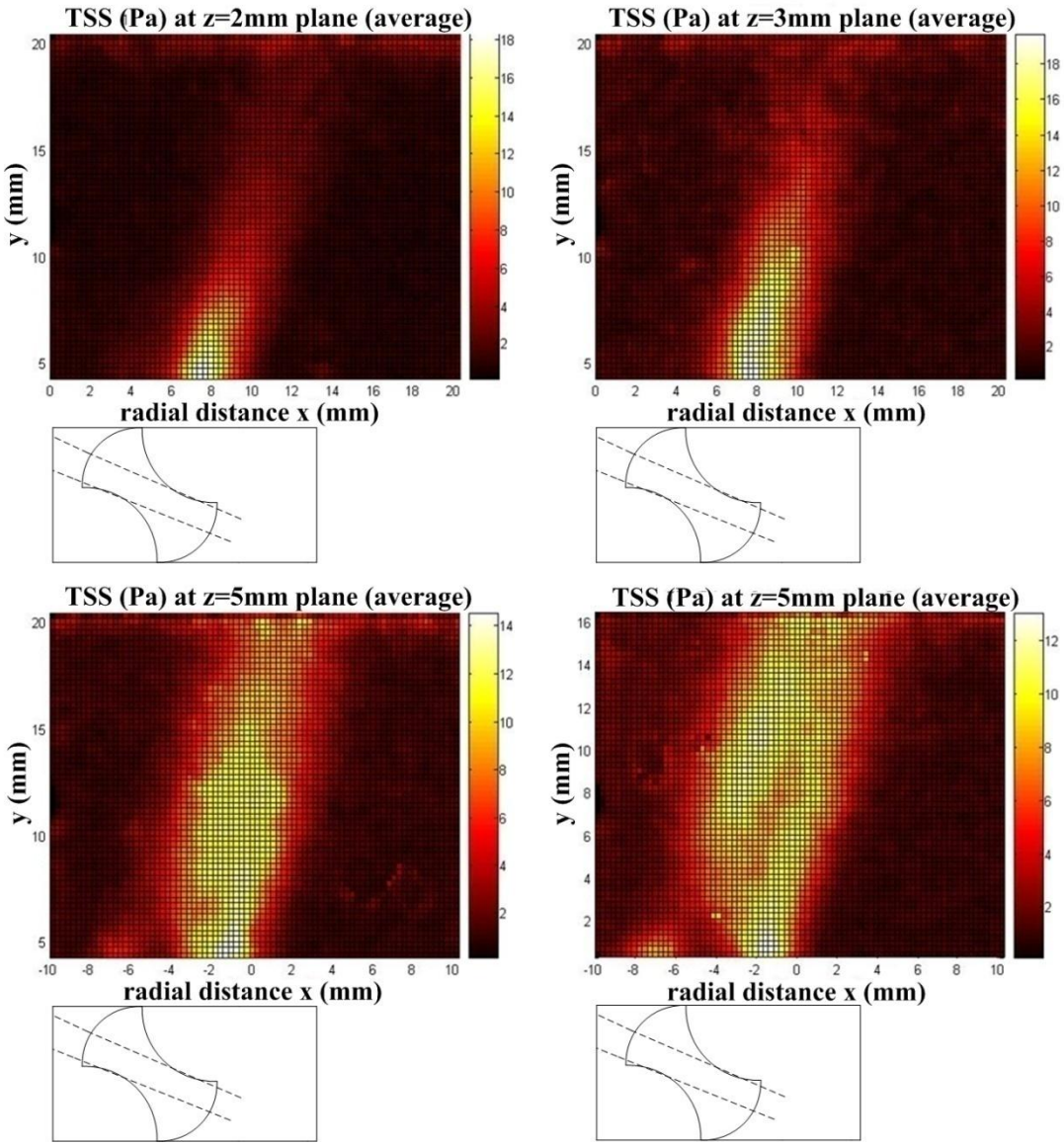

Figure 4.14: Averaged maximum TSS distributions on a serial of planes (valve type 2)

The repeatability test for TSS profiles of valve type 2 is illustrated in figure 4.15 and the red line represents the average profile based on the five multiple experiments. The peak values in five tests were listed in table 4.7 and the variation was 5.8%. The repeatability analysis verified a reliable experimental basis for numerical simulations and the simulation works will cooperated with TuCN in Romania. The average peak value for valve type 2 is 22.2 Pa, which is less critical for blood damage than that of valve type 1. Although the measured values of peak velocity magnitude for two valve types kept in the similar levels, the experimental results of valve type 1 apparently produced a higher regional gradient of velocity, the value of which the shear stress was dependent on. Thus, a relative high TSS was observed in results of valve type 1.

The multiple experimental results (valve type 2) for TSS distributions on serial planes were illustrated in Appendix 2.1.3, 2.2.3, 2.3.3 and 2.4.3.

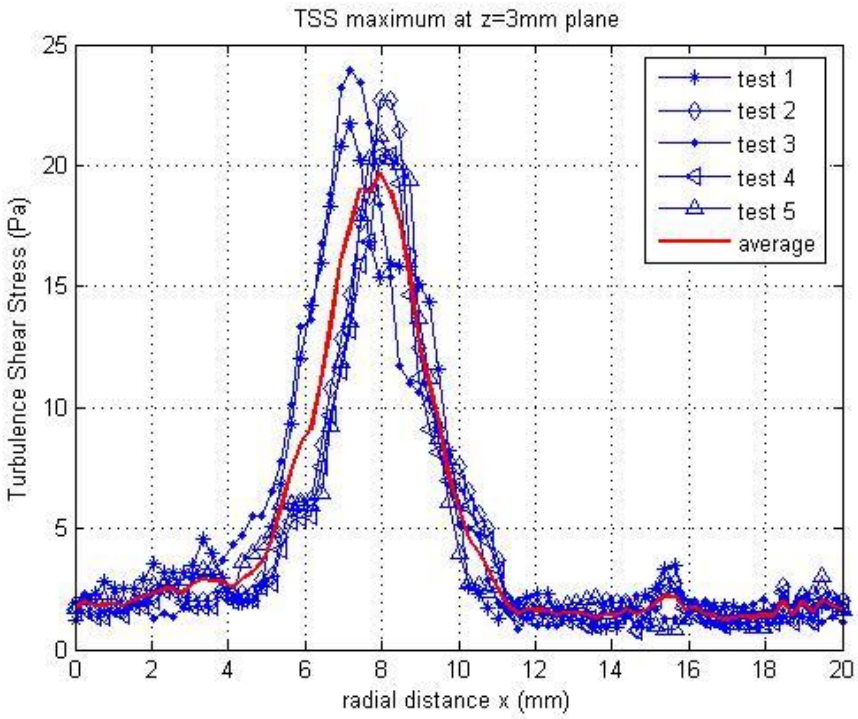

Figure 4.15: Peak TSS profiles from repeatability tests and average peak TSS profile based on 5 tests (valve type 2)

	Peak TSS (Pa)	Location Coordinates (x y z) (mm)
Test 1	21.7	(7.3,1.6,3)
Test 2	22.7	(8.0,3.4,3)
Test 3	23.9	(7.3,0.8,3)
Test 4	22.1	(8.0,1.6,3)
Test 5	20.4	(8.0,3.4,3)
Average	22.2	
Coefficient of variation	5.81%	

Table 4.7: repeatability results of peak TSS for five tests (type 2)

4.3.4 DISCUSSIONS

Particle image velocimetry (PIV) was applied to investigate leakage flow fields associated with two typical BMHVs. To obtain Repeatability analysis, 5 tests under same experimental conditions were taken. The variations for both peak velocity and peak TSS were around 5%, which will give a good experimental basis for simulation works. The maximum TSS of valve type 1 captured in leakage jets of BMHV was 41 Pa, while 22Pa of valve type 2. The values are reasonably low, especially with regard to the threshold for RBC membrane lysis proposed in the literature (TSS_max, threshold > 600 Pa [122]). However, the TSS may bring risks to platelet

activation and blood clotting events because the sensitive value for platelet lysis is 10 Pa [113] [124].

The numerical simulations to detect the potential risks in the same BMHV and under same boundary conditions will be carried out in TuCN and the results will be validated by our experimental data. Furthermore, we will use numerical data to study the orientation of the leakage jets in the region in which experiments cannot measure. The cooperation between ISS and TuCN will take use of experimental and simulation methodologies to define a standard procedure for sufficient confidence in risk evaluation and mitigation of prosthetic heart valves.

4.4 ANALYSIS OF LOCAL AND GLOBAL HEMOLYSIS INDEX IN 2D VELOCITY FIELD OF REGURGITANT FLOW IN MECHANICAL HEART VALVE

Previous works presented Hemolysis Index (HI) to access the damage to blood cells in artificial organs [125] [126]. HI evaluates the concentration of plasma free hemoglobin, which leaks from red blood cells due to the holes in membrane [109] because of the mechanical stresses in the fluid caused by artificial conditions. This reduces the ability to transport oxygen through body and results in hemolysis anemia. The RBCs deforms to become more elliptic with increase of shear stress and eventually elongated in efforts to reduce flow resistance. If the RBC maintains its elongated shape for an extended period of time it becomes less elastic and becomes what is known as mechanically damaged [127].

In 1965, Blackshear et al. [128] originally proposed the relationship between the amount of plasma-free hemoglobin $pfHb$ and time t with shear stress τ by the equation 1.

$$pfHb \sim \tau^2 t \tag{1}$$

The limitation of equation 1 was only examined in the range $1 < \tau < 10Pa$ for $t = 1h$. A power-law of the expression for HI is more often used as equation 2.

$$\frac{\Delta Hb}{Hb} = Ct^a \tau^b \tag{2}$$

where a, b and C are constant and $\frac{\Delta Hb}{Hb}$ is the ratio of plasma-free hemoglobin to the total hemoglobin.

Table 4.8 illustrates different values for the set of parameters from previous experiments. The experiments 1-3 were done by Giersiepen et al. [129], Heuser et al. [130], and Taskin et al.

[131].

	a	b	C
Experiment 1	0.785	2.416	3.62×10^{-7}
Experiment 2	0.765	1.991	1.8×10^{-8}
Experiment3	0.747	2.004	1.21×10^{-7}

Table 4.8: parameters of HI analysis from three groups

The purpose of this section is to investigate local and global quantities related to blood cells damage (HI) induced by bileaflet mechanical valve using PIV experimental approach. Properties of fluid dynamics, such as velocity and turbulent shear stress, are measured in 2D by PIV, which were taken averaged value from multiple experiments.

4.4.1 MATERIALS AND METHODS

In order to evaluate blood damage in the flow immediately downstream of the valve, it is important to trace the movement of individual particles as they pass through the elevated shear stress zone. The study of this section will give the analysis for the extent of blood damage associated with the valve concerned.

Since the PIV experiments measured 2D planes in nature with only axial and transverse velocity components, the blood particles were assumed to traverse within the plane of the laser light sheet. Therefore, only 2D particle trajectories were followed across the image frames. The results of PIV were based on the mean velocity vector fields. Thus, the path of the blood cell particles is the average path that a particle takes across the time interval during the exposure of image to the flow field. As the instantaneous velocity vector field was measured from a 100ms exposure time of the PIV image frames, the mean velocity vector field for HI analysis represents the velocity vectors over a 100ms time interval. The shear stress fields were analyzed based on a 100ms time interval as well.

To determine HI (%) in the flow immediately downstream of the valve, it is essential to trace the path way through the cornered TSS zone for individual particle. In order to calculate HI (%) with equation (1) in each point of the flow field, a previous evaluation of the exposure time of the blood cells, under the respective shear fields, is necessary. To achieve this point, we analyze exposure time and maximum shear stress for the blood cells moving along the longitudinal axis in the measured 2D flow field. A small section ΔL along the longitudinal axis with a constant

velocity of moving blood cells is assumed, as shown in Fig 4.16. The longitudinal axis is divided into N sections.

$$N = \frac{L}{\Delta L} \tag{3}$$

where L is total distance of blood cells transporting along longitudinal axis in measured field.

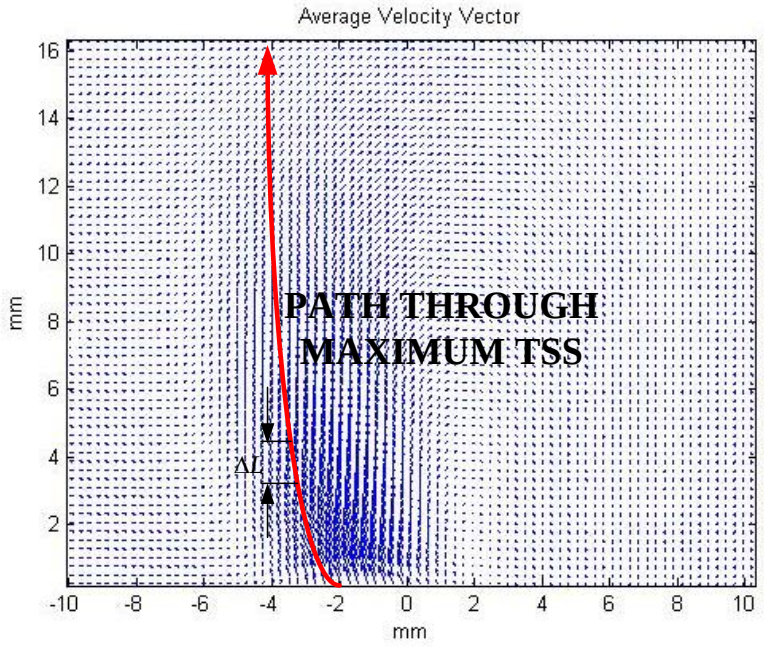

Figure 4.16: Path line for blood flow direction

The exposure time for each point can be estimated as follow:

$$t_{\exp} = \frac{\Delta L}{V \times \cos\theta} \tag{4}$$

where $\tan\theta = v_x / v_y$.

Then hemolysis index (within section) can be calculated as

$$HI_{\sec}(\%) = C * t_{\exp}{}^{\alpha} \tau^{\beta} \tag{5}$$

According to newly published work of Taskin et al [108], $C = 1.21 \times 10^{-5}$, $\alpha = 0.747$, $\beta = 2.004$.

After calculating all section of the flow field, the global hemolysis index [110] can be given as

$$HI_{t\ o}(\%) = \sum_{N} HI_{\sec}(\%) \tag{6}$$

4.4.2 HI ANALYSIS FOR VALVE TYPE 1

To incorporate the effects of shear stress and exposure time to the evaluation of the hemolysis, the local and global HI were solved by equation (5), (6). Figure 4.17 shows HI distributions for each measured plane of tested valve type 1. According to the evaluation, the critical regions for hemolysis were originated from the leakage jets corresponding to four hinge corners. Compared all the measured planes, the plane Z=1mm was found the peak value of HI. Due to relative high speed magnitude, the measured plane Z=2mm with peak shear stress did not give highest HI values. At first glance, non-uniform hemolysis distribution was observed on 2D measured plane. It was pronounced that the leakage jets brought certain damage to blood elements. The highest HI was observed close to the hinge downstream corners, which were certainly influenced by high shear stress. The leakage jets from upstream corner induced relatively lower HI because of short exposure time of blood elements in these regions.

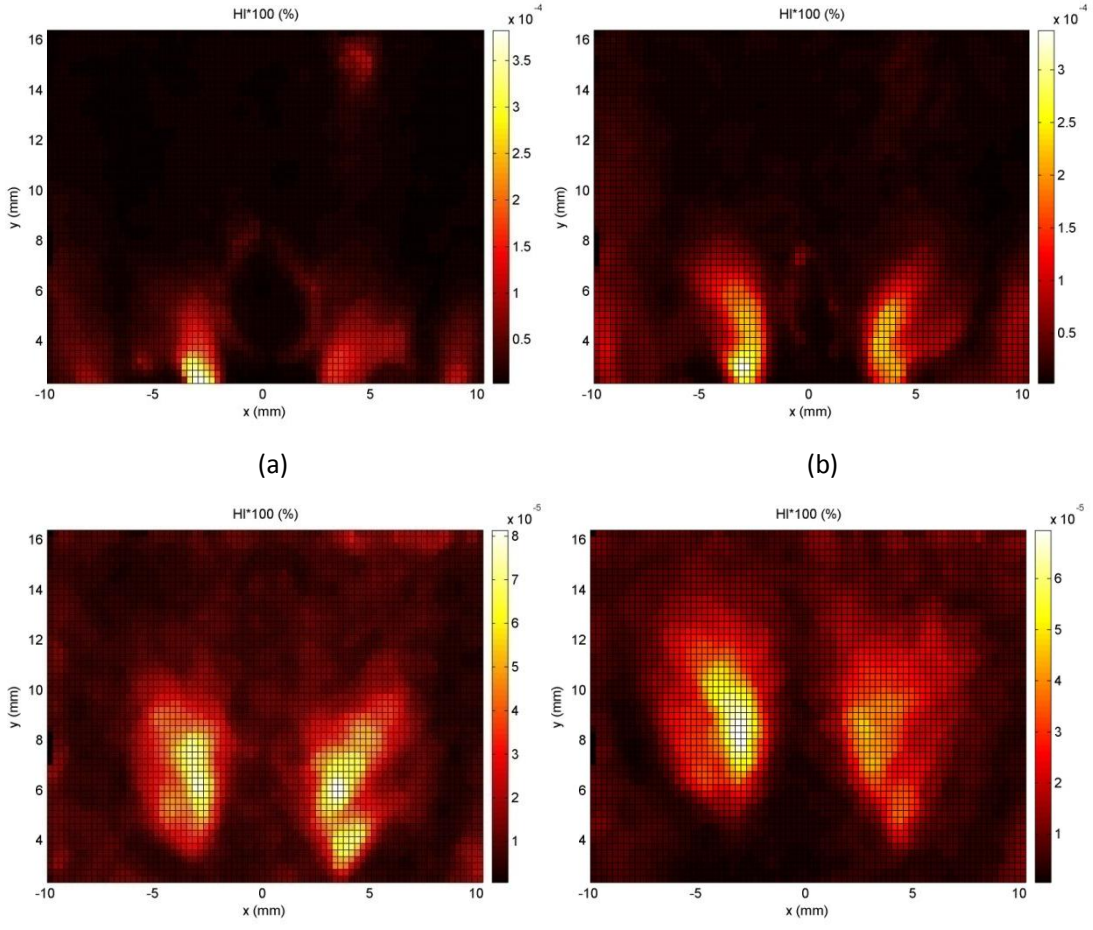

Figure 4.17: HI (%) 2D distributions on serial of measured planes: (a) Z=1mm, (b) Z=2mm, (c) Z=3mm, (d) Z=4mm (valve type 1)

In figure 4.18 (a), the results of local HI were calculated by equation (5) along the path of

maximum shear stress. There parameters have been processed based on PIV multiple experiments with averaged velocity magnitude and local shear stress.

The comparison of the shear stress, velocity and HI with normalized values was illustrated in figure 4.18 (b). From calculated steps 0-10 section, relative low HI was observed with high shear tress and low exposure time. The peak HI values were located from step 10-30 section with high shear stress and relative low velocity. Additionally, the HI dramatically decreased from the step 30 into the section with lowest values due to low shear stress with relative low exposure time.

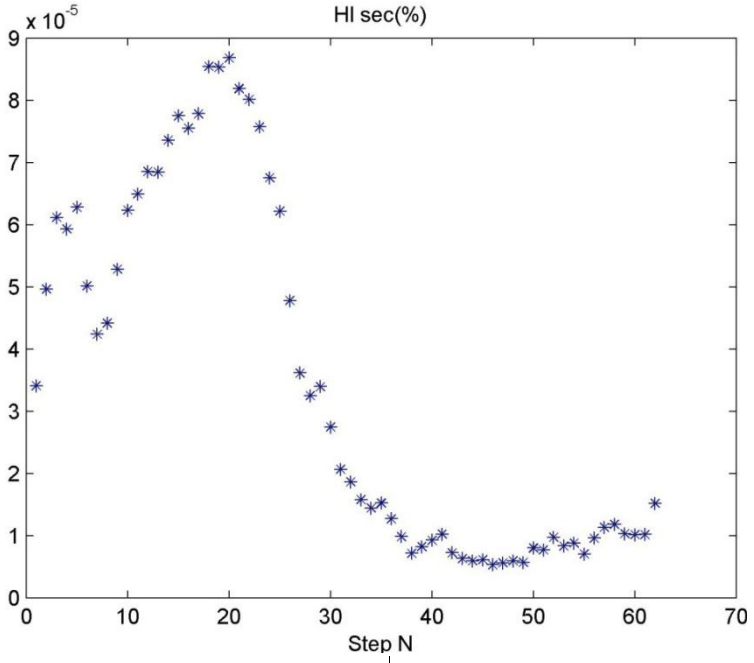

(a)

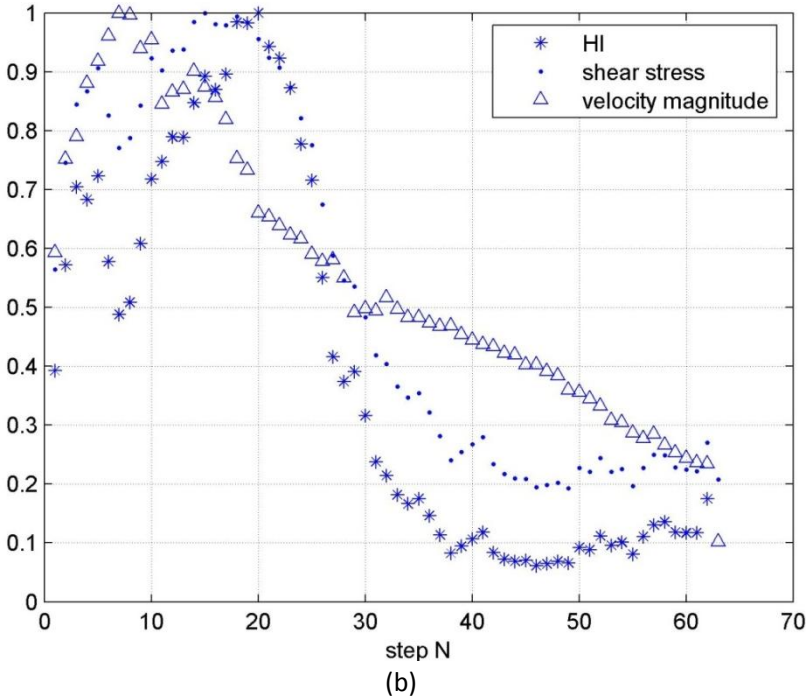

(b)

Figure 4.18: (a) local HI(%) along calculated step N; (b) normalized local HI(%), velocity and TSS (valve type 1)

Table 4.9 shows the global HI values calculated according to equation (6) on 2D measured planes with maximum local HI value and maximum shear stress. The peak value of global HI was observed on plane z=1mm with 2.8×10^{-3}%.

	Maximum shear stress (Pa)	Maximum HI_sec (%)	HI_tot (%)
Measured 2D plane Z=1mm	35	2.4×10^{-4}	2.8×10^{-3}
Measured 2D plane Z=2mm	39	8.7×10^{-5}	2.1×10^{-3}
Measured 2D plane Z=3mm	17	2.3×10^{-5}	6.0×10^{-4}
Measured 2D plane Z=4mm	15	1.8×10^{-4}	2.1×10^{-3}

Table 4.9: peak valves of shear stress, local HI(%) and global HI(%) on different planes (valve type 1)

4.4.3 HI ANALYSIS FOR VALVE TYPE 2

In this section, the values of global HI and local HI for vale type 2 were assessed consistently with scanned slices in regurgitant leakage jet. Flow visualization was achieved by PIV. Measured slices were from 2mm to 5mm away hinge recess plane.

Figure 4.19 shows local HI distributions for each measured plane of tested valve type 2. The critical regions for blood damage were reserved on only one leakage jet on each side of the gap between the housing and leaflet. This observation is corresponding to the shear stress distribution for valve type 2. Additionally, two path ways with high local HI values were presented in figure 4.19 (a) close to the critical regions. This result may be contributed to relatively high shear stress with long exposure time induced by high velocity gradients. Compared all the measured planes, the plane Z=2mm was found with the peak value of local HI.

In figure 4.20 (a), the results of local HI for valve type 2 were calculated by equation (5) along the path of maximum shear stress. There parameters have been processed based on PIV multiple experiments with averaged velocity magnitude and local shear stress. The local values

of HI (%) decreased gradually as evaluated point moving along the longitudinal axis.

The comparison of the shear stress, velocity and HI with normalized values was illustrated in figure 4.20 (b). From calculated steps 0-10 section, relative low HI was observed with high shear tress and low exposure time. As the local HI results presented good agreements with shear stress, the velocity magnitude influences HI results less than that of shear stress. In addition, relative high values of local HI were observed after calculated step 60 with relative low exposure time.

Table 4.10 shows the global HI values calculated according to equation (6) on 2D measured planes with maximum local HI value and maximum shear stress. The peak value of global HI was observed on plane z=2mm with 3.5×10^{-3}%.

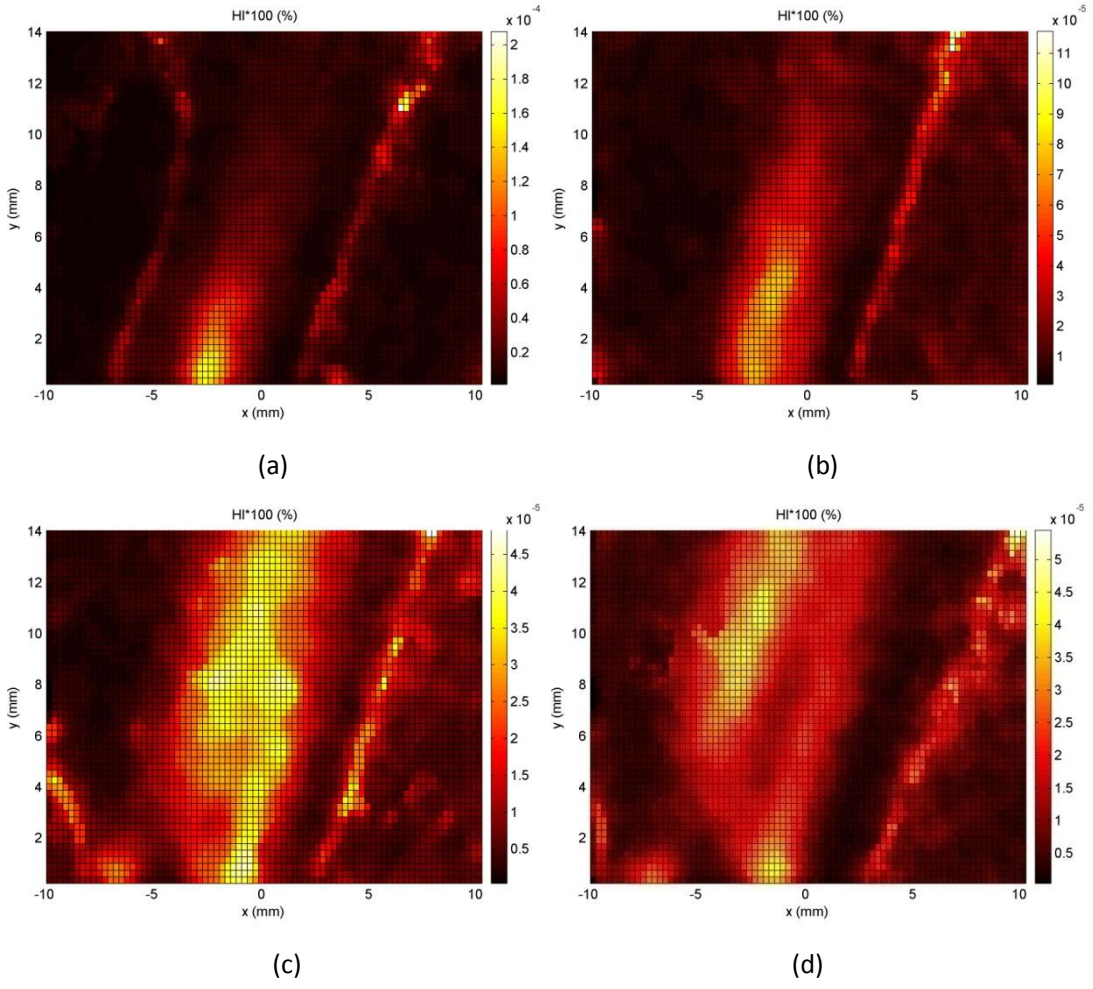

(a) (b)

(c) (d)

Figure 4.19: HI (%) 2D distributions on serial of measured planes: (a) Z=2mm, (b) Z=3mm, (c) Z=4mm, (d) Z=5mm (valve type 2)

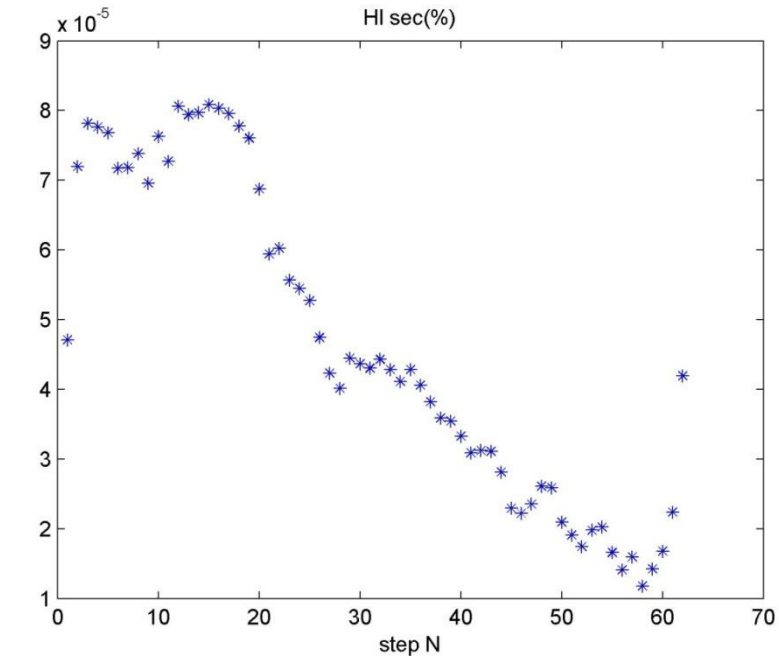

(a)

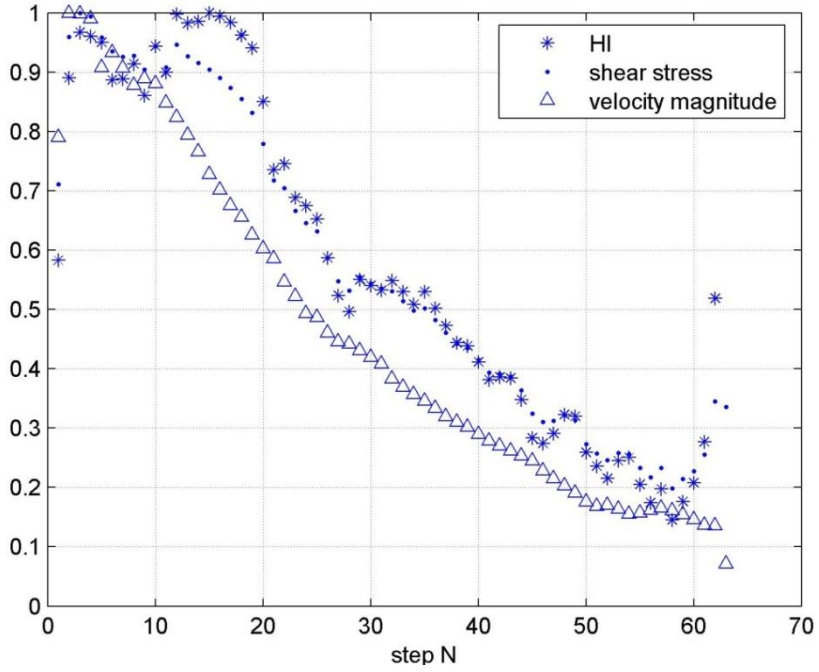

(b)

Figure 4.20: (a) local HI(%) along calculated step N; (b) normalized local HI(%), velocity and TSS (valve type 2)

	Maximum shear stress (Pa)	Maximum HI_sec (%)	HI_tot (%)
Measured 2D plane Z=2mm	18	1.8×10^{-4}	3.5×10^{-3}
Measured 2D plane Z=3mm	20	8.1×10^{-5}	2.9×10^{-3}
Measured 2D plane Z=4mm	14	6.9×10^{-5}	2.4×10^{-3}
Measured 2D plane Z=5mm	12	4.5×10^{-5}	1.7×10^{-3}

Table 4.10: peak valves of shear stress, local HI(%) and global HI(%) on different planes (valve type 2)

4.4.4 DISCUSSIONS

The study offered a comprehensive experimental evaluation of blood injury induced by prosthetic mechanical heart valve. Furthermore, the evaluation of a local and global hemolysis index, by using local shear stresses and velocities values generated by PIV, allows to quantify and to compare the propensity for hemolysis of different mechanical heart valves. The results will be used for comparisons with simulation data.

From the analysis of local and global HI (%), the HI values were not in the highest level for the highly elevated shear stress regions. These observations may interpret the relative significance of the exposure time for HI analysis due to different flow features such as flow vortex, the velocity vector fields and different flow paths. Thus, the conclusion can be easily given that the hemolysis potential can not only be analyzed by the shear stress fields. In order to analyze the hemolysis potential properly, the influence of exposure time should be taken into consideration. In conclusion, the HI distributions were utilized to make specific evaluation for blood damage regarding operating conditions.

Chapter 5
Comparisons of PIV and CFD Simulation

Computational Fluid Dynamics (CFD) has become a promising tool, which can provide insights of unprecedented details into the hemodynamics of prosthetic heart valves. Nowadays new computational methods are applying to investigate levels of hemolysis [132]-[138] and thrombosis [139]-[143] from the local fluid dynamics derived from simulation with a variety of mathematical methods [144]-[148]. Compared to experimental methods, the advantages of numerical solutions are that they can analyze the insight of performances from complex geometry without having to produce costly prototypes, provide data in the regions in which experimental measures may not be easy to obtain, and supplement the data for immeasurable physical quantities [149].

However, the use of CFD has not been adequately or systematically validated in pre-market device applications. In order to gain the confidence of valve designers and medical practitioners, CFD must undergo comprehensive validation with experimental data. To fulfill the validations, the use of high-resolution flow measuring tools and techniques such as PIV and LDA are required.

The aim of this chapter is to investigate the complex flow phenomena with two reliable research techniques: Particle Image Velocimetry (PIV) and Computational Fluid Dynamics (CFD). The PIV experimental methods and results have specifically demonstrated in chapter 3 and chapter 4. The setups of numerical simulation for prosthetic valve type 2 are described in this chapter. The multiple experimental data is applied to validate the numerical solutions including the valve model selection and mesh independence analysis.

5.1 METHODS

5.1.1 GEOMETRY CAD

To be able to compare the results from the different measurement techniques with each other, it had to be ensured that the same geometry was used for both PIV and CFD simulations. The valve type 2 was selected for this study as it is currently one of the most implanted BMHV, was available at TuCN [150]. The CAD model was built in Catia, based on precise measurements taken with mechanical and optical scanners. The advantage of our new CAD model is that, being

fully parametric, it allows for adjusting and/or changing the geometry at any time. The collision test analysis showed that the two leaflets rotate around their individual axes with exactly 53 degrees without any contact between them or with the valve housing, thus allowing for a better closure of the valve.

Figure 5.1 shows a series of views and the design sketch of the hinge area for the valve type 2.

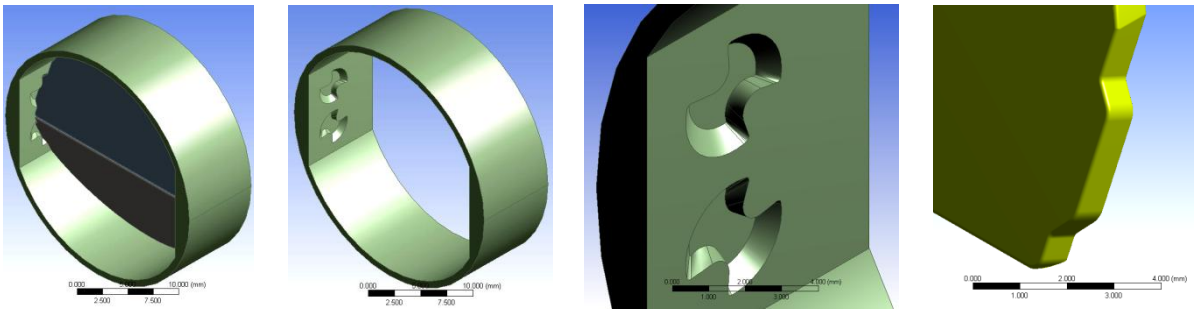

a) b) c) d)

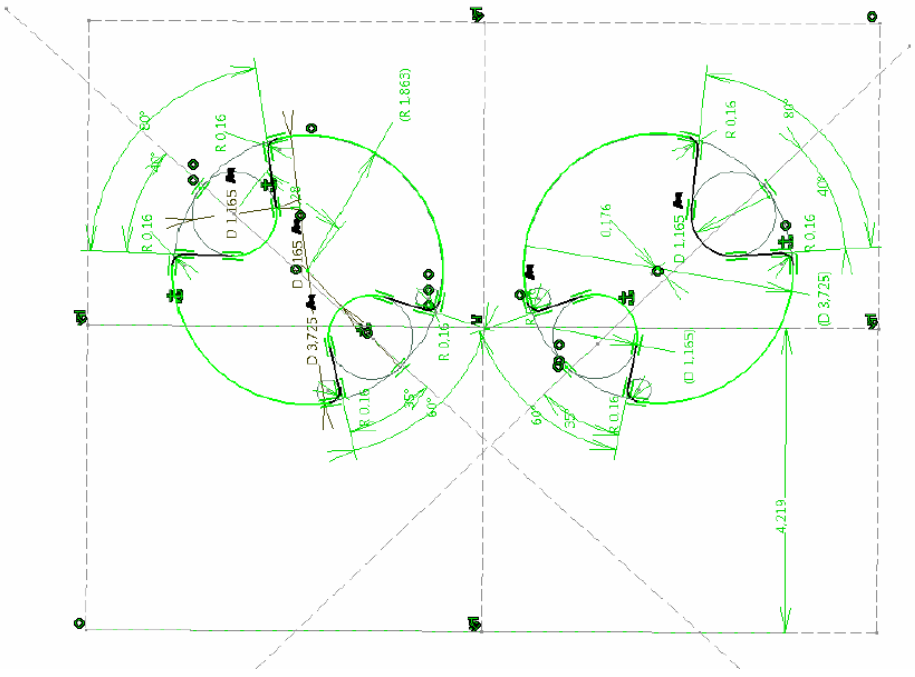

e)

Figure 5.1: Images of CAD model of the CarboMedics valve and the hinge area sketch

Based on an accurate scan of the valve geometry, its 3D model was reconstructed and extended with the upper and lower chambers. The valve model was sealed between upper chamber with diameter 195 mm and 85 mm in height representing aortic region and a small lower chamber with diameter 45 mm representing ventricular region.

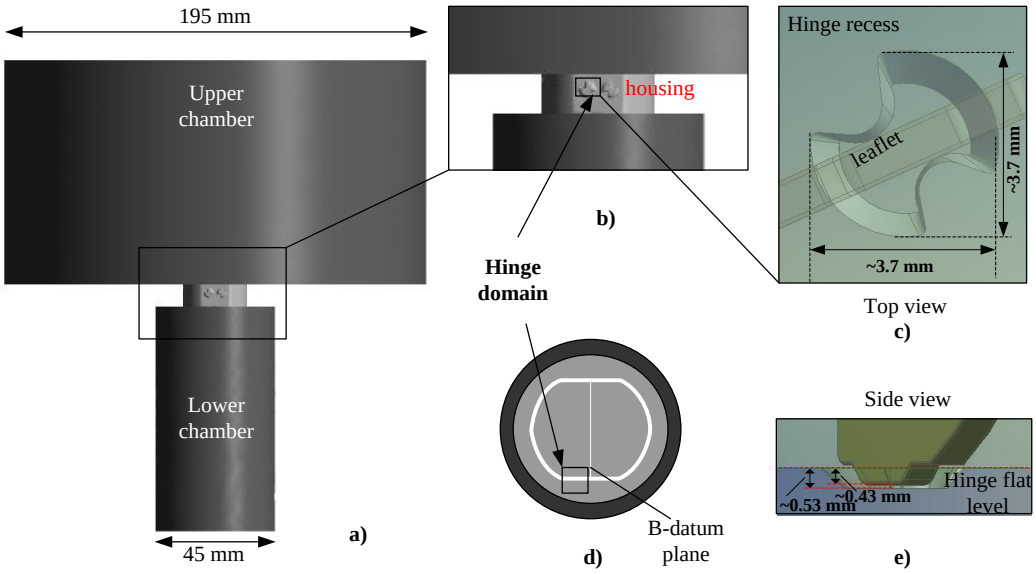

Figure 5.2: Geometry of model

The closure phase of the bileaflet valve in mitral position was modeled in the chapter with a constant pressure drop 75mmHg for regurgitant flow investigation. Figure 5.2 a) shows large-scale numerical model generated corresponding to simulation model. Figure 5.2 b) shows the model of valve housing corresponding to shade area in large scale model. The hinge model was shown in figure 5.2 c) and the hinge recess, characterized by its butterfly shape, was clearly visible. Top view of hinge location with B-datum plane was illustrated in figure 5.2 d). The leaflet ear was positioned within the hinge recess such that the hinge gap width (distance between the bottom of the hinge recess and the tip of the leaflet ear, defined as figure 5.2 e)) was approximately that seen in clinical valves (0.1 mm).

5.1.2 MESH INDEPENDENCE

The mesh independence study was carried out based on the maximum velocity of analysis domain under the same pressure drop condition 75mmHg. The mesh independence analysis for a reasonable solution of this operating condition should be applicable to the future simulation analysis for fluid dynamics of BMHVs.

For mesh independence analysis, ten different models (M_1 to M_10) from coarse to fine mesh density were generated. Ten models contain the total number of cells range from 2.1 to 17.84 million. The overall mesh sizes and details of mesh elements in flow domains are provided in table 5.1. From model M_1 to M_10, the number of total cells was enhanced by a factor of 8.5 and the computational time was increased almost nine times. Exceeding 18 million cells models were tested, but they brought computational burden which would make it difficult to obtain reasonable solutions as a consequence of more computational resources requirements.

The differences of maximum velocity of models were compared with the finest mesh solution. Figure 5.3 provides results of velocity differences from ten mesh models. More specifically, the results of models M_1 to M_4 are around 20% lower than the finest model M_10 and models M_5 to M_7 are in the range 20% to 10% lower than the finest model. Until increasing mesh cells to 11 million, the differences start to be decreased to below 10%.

Model	Mesh density	Total number of cells (M)	Simulation time	Maximum velocity (m/s)	Difference (%)
M_1	0.1	2.1	1:44:33	0.589	14.13
M_2	0.002	3.86	1:51:37	0.595	13.27
M_3	0.0018	4.6	2:24:15	0.568	17.20
M_4	0.0017	5.11	2:39:23	0.546	20.41
M_5	0.0015	6.59	3:17:27	0.601	12.39
M_6	0.0014	7.67	4:09:16	0.582	15.16
M_7	0.0013	9.13	4:55:21	0.595	13.27
M_8	0.0012	11.1	10:27:27	0.617	10.06
M_9	0.0011	13.86	39:33:00	0.643	6.27
M_10	0.001	17.84	96:04:12	0.686	0

Table 5.1: Details for ten mesh models

Based on the above results and discussions, the model M_10 was selected for investigation of fluid dynamics propertied of MBHVs, even though it requires more processing time.

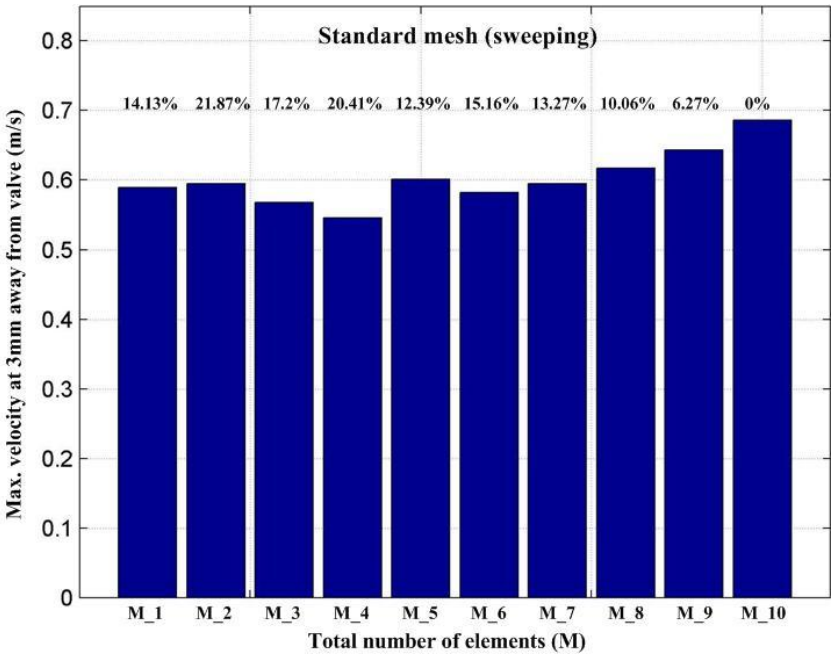

Figure 5.3: Peak velocity differences from different mesh models

5.1.3 BOUNDARY CONDITIONS

The simulations were performed with ANSYS-CFX 13 [151]. Since the jet flow will be turbulent, the Reynolds Averaged Navier-Stokes equations (RANS) have been solved with the standard k-epsilon turbulence model for incompressible flow. To save computational resources, only one quarter of the whole model was initially considered. For the fluid, a Newtonian incompressible liquid model with density the ρ=1.1 kg/ cm^3 and the dynamic viscosity μ=1cP was used. A 75 mmHg of pressure drop was applied to the model. The applied boundary conditions are illustrated in Figure 5.4.

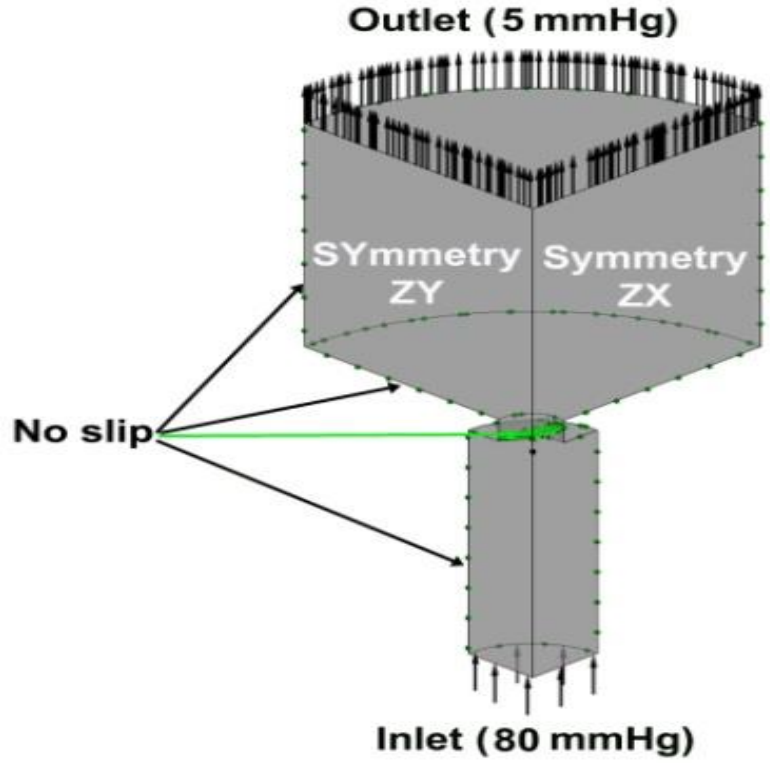

Figure 5.4: Boundary conditions setup

5.1.4 K-EPSILON MODEL

Nowadays turbulent flows may be computed using several different approaches, either by solving the Reynolds-averaged Navier-Stokes equations with suitable models for turbulent quantities or by computing them directly. The main approaches are summarized as below:

Reynolds-Averaged Navier-Stokes (RANS) Models

- Eddy-viscosity models (EVM)

- Non-linear eddy-viscosity models (NLEVM)

Turbulent stress is modeled as a non-linear function of mean velocity gradients. Turbulent scales are determined by solving transport equations (usually k + one other quantity). Model is set to mimic response of turbulence to certain important types of strain.

- Differential stress models (DSM)

This category consists of Reynolds-stress transport models (RSTM) or second-order closure models (SOC). One is required to solve transport equations for all turbulent stresses.

Computation of fluctuating quantities

- Large-eddy simulation (LES)

One computes time-varying flow, but models sub-grid-scale motions.

- Direct numerical simulation (DNS)

No modeling what so ever is applied. One is required to resolve the smallest scales of the flow as well.

The k-epsilon model is one of the most common turbulence models, although it just doesn't perform well in cases of large adverse pressure gradients [152]. It is a two equation model, which means, it includes two extra transport equations to represent the turbulent properties of the flow. This allows a two equation model to account for history effects like convection and diffusion of turbulent energy.

The first transported variable is turbulent kinetic energy, k. The second transported variable in this case is the turbulent dissipation, ϵ. It is the variable that determines the scale of the turbulence, whereas the first variable, k, determines the energy in the turbulence.

There are two major formulations of k-epsilon models [153][154]. That of Launder and Sharma is typically called the "Standard" k-epsilon Model. The original impetus for the k-epsilon model was to improve the mixing-length model, as well as to find an alternative to algebraically prescribing turbulent length scales in moderate to high complexity flows.

As described in Reference 19, the k-epsilon model has been shown to be useful for free-shear layer flows with relatively small pressure gradients. Similarly, for wall-bounded and internal flows, the model gives good results only in cases where mean pressure gradients are small; accuracy has been shown experimentally to be reduced for flows containing large adverse pressure gradients. One might infer then, that the k-epsilon model would be an inappropriate choice for problems such as inlets and compressors.

For general purpose simulations, the k-epsilon model offers a good compromise in terms of accuracy and robustness. Within CFX, the k-epsilon turbulence model uses the scalable wall-function approach to improve robustness and accuracy when the near-wall mesh is very fine. The scalable wall functions allow solution on arbitrarily fine near wall grids, which is a significant improvement over standard wall functions.

To calculate boundary conditions for these models see turbulence free-stream boundary conditions.

The eddy-viscosity used with Boussinesq approximation is calculated as:

Eddy viscosity:

$$\nu_t = C_\mu \frac{k^2}{\varepsilon}$$

Scalar-transport equations (non-conservative form):

$$\rho \frac{D_k}{D_t} = \frac{\partial}{\partial x_i}\left(\Gamma^k \frac{\partial k}{\partial x_i}\right) + \rho(P^k - \varepsilon)$$

$$\rho \frac{D_\varepsilon}{D_t} = \frac{\partial}{\partial x_i}\left(\Gamma^\varepsilon \frac{\partial \varepsilon}{\partial x_i}\right) + \rho(C_{\varepsilon 1} P^k - C_{\varepsilon 2}\varepsilon)\frac{\varepsilon}{k}$$

Diffusivities Γ^k and Γ^ε are related to the eddy viscosity via Prandtl numbers σ:

$$\Gamma^k = \mu + \frac{\mu_t}{\sigma^k}, \qquad \Gamma^\varepsilon = \mu + \frac{\mu_t}{\sigma^\varepsilon}$$

The rate of production of turbulent kinetic energy (per unit nass) is

$$P^k = -\overline{u_i u_j}\frac{\partial U_i}{\partial x_j}$$

In the standard k-epsilon model (Launder and Spalding, 1974) the coefficients take the values

$$C_\mu = 0.09,\ \ C_{\varepsilon 1} = 1.92,\ \ C_{\varepsilon 2} = 1.44,\ \ \sigma^k = 1,\ \ \sigma^\varepsilon = 1.3$$

K-epsilon model leads to stable calculations that converge relatively easily and is relatively simple to implement. It has reasonable prediction for many flows but poor predictions for swirling and rotating flows, flows with strong separation, axisymmetric jets, certain unconfined flows and fully developed flows in non-circular ducts. It is valid only for fully turbulent flows.

5.2 RESULTS

5.2.1 EXPERIMENTAL VALIDATIONS

To quantitatively compare simulation data to experimental data, we defended two parameters for difference evaluations: Difference of Maximum Velocity (DMV) and Difference of Velocity Distribution Map (DVDM). DMV can be calculated as equation (1). In order to calculate DVDM, we extract certain corresponding points from experimental data and simulation data at each downstream location of the velocity maps and take the average of the differences for all extracted corresponding points. DVDM that can be calculated as equation (2) reflects the average variations of velocity distributions obtained by two different methodologies.

$$DMV = \frac{\left| v_{PIV\_\max} - v_{CFD\_\max} \right|}{v_{PIV\_\max}} \times 100\% \quad (1)$$

Where $v_{PIV\_\max}$ and $v_{CFD\_\max}$ are obtained maximum velocities in the whole compared domain separately.

$$DVDM = \frac{\sum_{n} \frac{\left| v_{PIV}(x) - v_{CFD}(x) \right|}{v_{PIV}(x)}}{n} \times 100\% \quad (2)$$

Where $v_{PIV}(x)$, $v_{CFD}(x)$ and n are experimental velocity, simulation velocity at certain points and the number of extracted points.

In order to save computational sources, we divided the whole valve geometry into a 1/4 model for the first simulation works, which was based on the hypothesis that flow field was symmetrical. However, the simulation works were under turbulent flow conditions and suspicions were raised to the symmetrical hypothesis. Therefore, the entire valve model was adopted for the next simulation works. To achieve the highest mesh density, the entire valve model required 96 hours for a simulation circle and 1/4 model only needed 8 hours under same computational conditions.

In this section, two valve models were compared to each other and verified by the experimental data. Figure 5.5-5.8 show the compared velocity profiles for different scanned planes at different downstream locations. In figure 5.5, the apparent disagreements can be observed between data from 1/4 model and multiple experimental data at downstream location y= 4 and 6 mm. The comparison results can be dramatically improved by taking use the whole valve mode. In figure 5.6-5.7, the comparison results give consistent good agreements with multiple experimental data for both 1/4 model and whole valve model. In figure 5.7, slight

disagreements can be observed between experimental data and numerical data at downstream locations y= 4 and 6mm. This might be due to the fact that the used k-epsilon turbulence model for incompressible flow applies the standard settings.

Table 5.2 shows calculated DMV and DVDM for two models separately. DMV obtained by 1/4 model range from 4.5% to 18.9% for all scanned 2D planes and the averaged DMV in 1/4 model is 12.75%. In contrast with 1/4 model, the whole valve model has only 9.8% averaged DMV with experimental data. In some evaluated locations, the DMV in the whole model are even less than 1% such as the jets leaving the 8mm orifice on scanned planes Z=3mm Z=4mm. For the DVDM analysis, 1/4 model gives around 70% and the value from whole model is around 50%. According to quantitatively analysis, the whole valve model show better agreements with experimental data. The symmetrical hypothesis may not be a good solution for turbulent flow simulations. For the continuous simulation works, we will insist on taking use of the whole valve model.

		1/4 model		***Whole model***	
		DMV	***DVDM***	***DMV***	***DVDM***
Plane Z=2mm	y=4mm	15.7%	96.6%	2.1%	65.8%
	y=6mm	27.0%	58.4%	11.9%	47.3%
	y=8mm	16.2%	64.1%	24.0%	52.8%
	y=10mm	16.7%	78.4%	40.6%	59.0%
	Average	**18.9%**	**74.4%**	**19.6%**	**56.2%**
Plane Z=3mm	y=4mm	4.9%	80.0%	3.5%	62.6%
	y=6mm	10.3%	54.5%	1.8%	43.1%
	y=8mm	21.2%	53.4%	0.1%	37.3%
	y=10mm	17.5%	53.4%	1.4%	36.1%
	Average	**13.5%**	**60.3%**	**1.7%**	**44.8%**
Plane Z=4mm	y=4mm	3.8%	78.1%	2.9%	57.9%
	y=6mm	2.5%	61.6%	2.8%	43.5%
	y=8mm	3.0%	58.9%	0.6%	42.0%
	y=10mm	8.8%	58.9%	2.7%	43.4%
	Average	**4.5%**	**64.3%**	**2.2%**	**46.7%**
Plane Z=5mm	y=4mm	25.0%	76.5%	15.9%	54.1%
	y=6mm	16.8%	72.4%	22.5%	48.2%
	y=8mm	11.3%	66.1%	11.1%	48.2%
	y=10mm	3.3%	64.1%	1.5%	50.8%
	Average	**14.1%**	**69.8%**	**12.8%**	**50.3%**

Table 5.2: DMV and DVDM results of two valve models

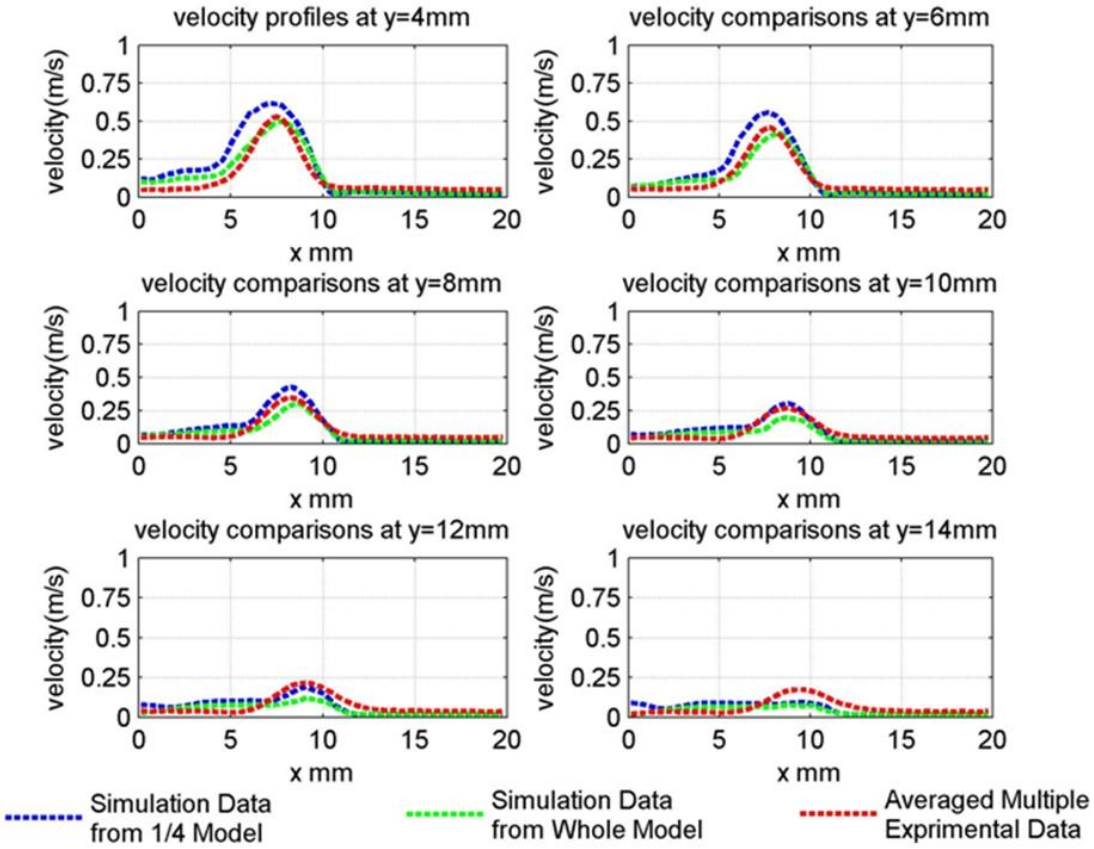

Fig. 5.5 velocity profiles at different downstream locations from two models and PIV on Z=2mm

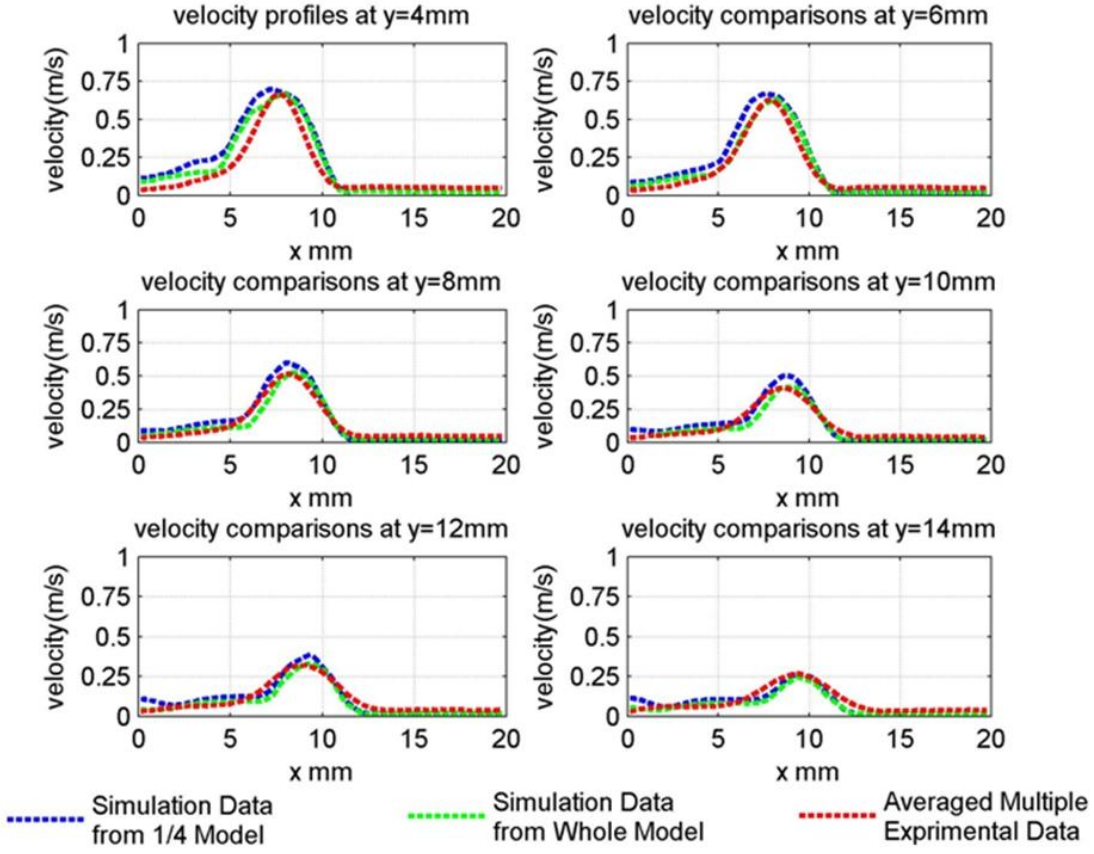

Fig. 5.6 velocity profiles at different downstream locations from two models and PIV on Z=3mm

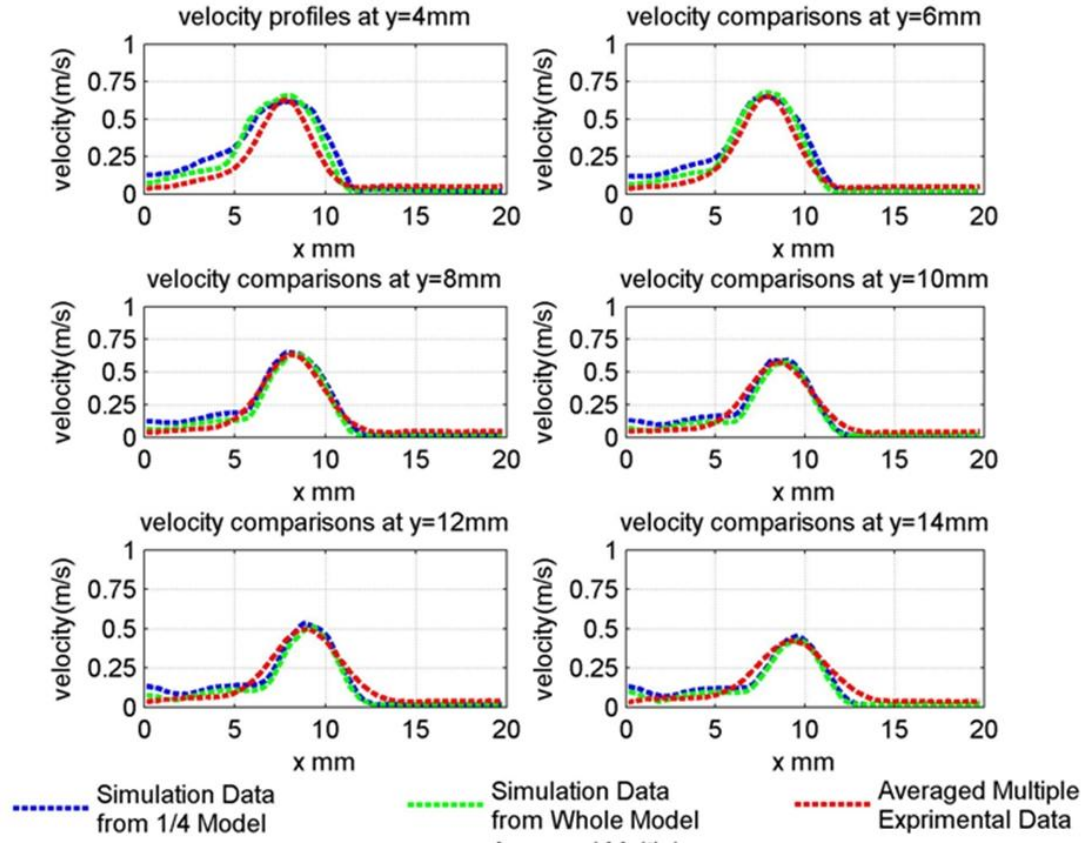

Fig. 5.7 velocity profiles at different downstream locations from two models and PIV on Z=4mm

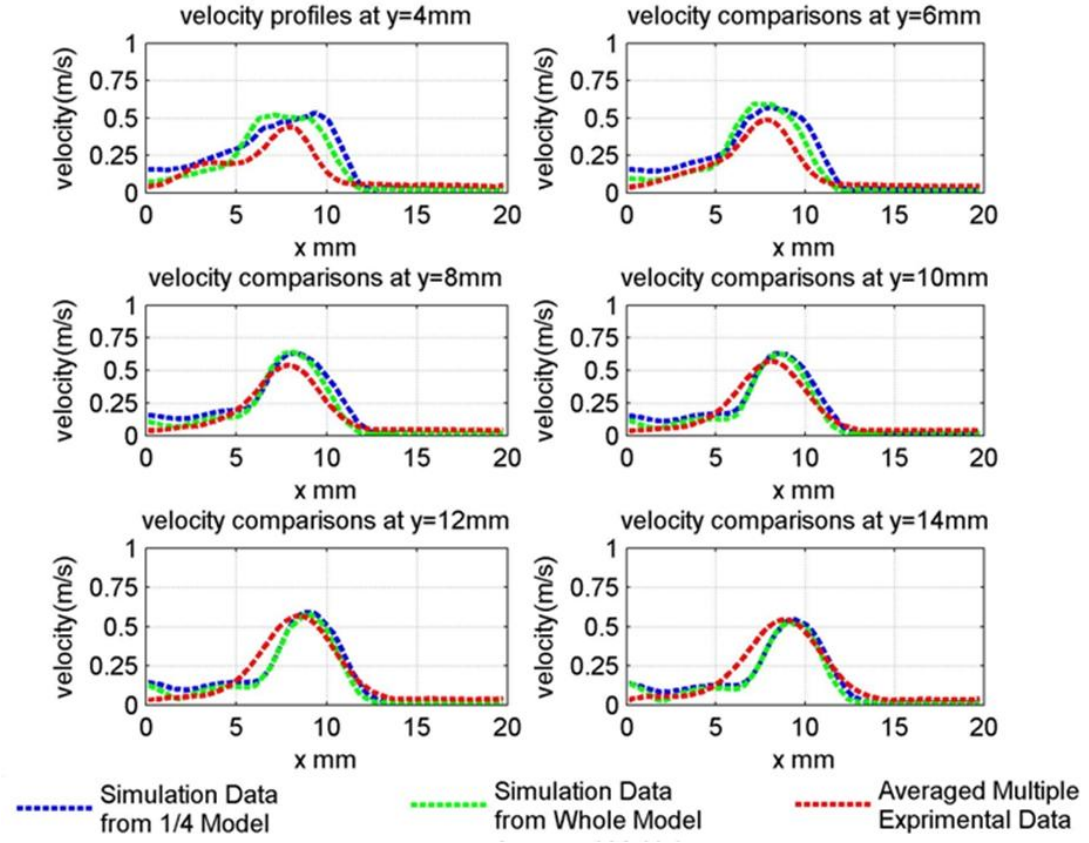

Fig. 5.8 velocity profiles at different downstream locations from two models and PIV on Z=5mm

As an additional evaluation, velocity profiles of ten models were verified with averaged multiple experimental data as illustrated in Figure. 5.9. It was observed that profile disagreements with experimental data through model M_1 to M_9 were more visible and pronounced. On the contrary, an improved correlation between experiment and simulation was obtained by selecting model M_10.

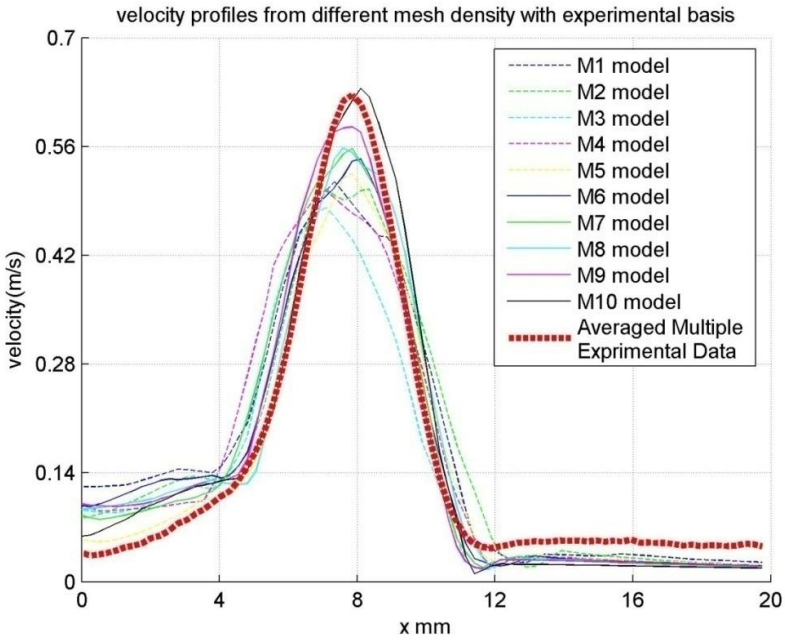

Figure: 5.9 velocity profiles from ten models validating with averaged multiple experimental data

Based on the above results and discussions, the model M_10 was selected for investigation of fluid dynamics propertied of MBHVs, even though it requires more processing time. After determination of the proper simulation model, the final results of comparisons were demonstrated in Figure 5.10-Figure 5.13. It was observed that a good quantitative agreement in velocity distribution maps was achieved between PIV and CFD. Table 5.3 shows the difference of peak velocity between PIV and CFD.

	Peak velocity from PIV	Peak velocity from CFD	Difference (%)
On measured plane Z=2mm	0.579 m/s	0.649 m/s	12.1%
On measured plane Z=3mm	0.702 m/s	0.697 m/s	0.7%
On measured plane Z=4mm	0.652 m/s	0.664 m/s	1.8%
On measured plane Z=5mm	0.584 m/s	0.638 m/s	9.3%

Table 5.3: differences of peak velocity between PIV and CFD

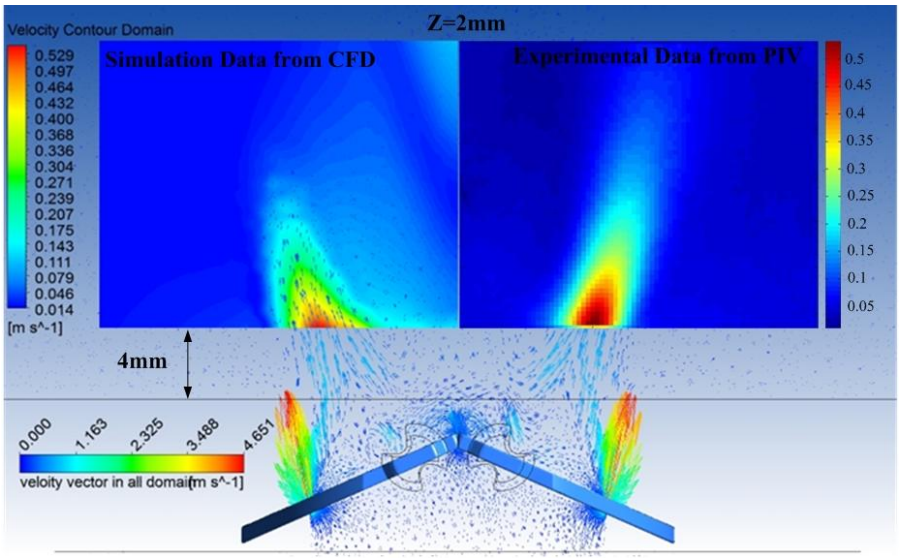

Figure 5.10: comparisons of velocity distribution maps from PIV and CFD on plane Z=2mm

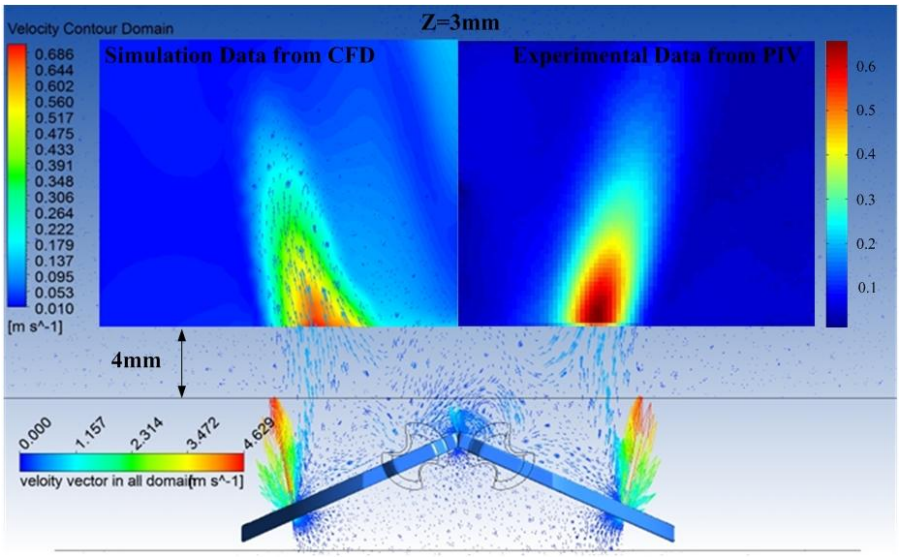

Figure 5.11: comparisons of velocity distribution maps from PIV and CFD on plane Z=3mm

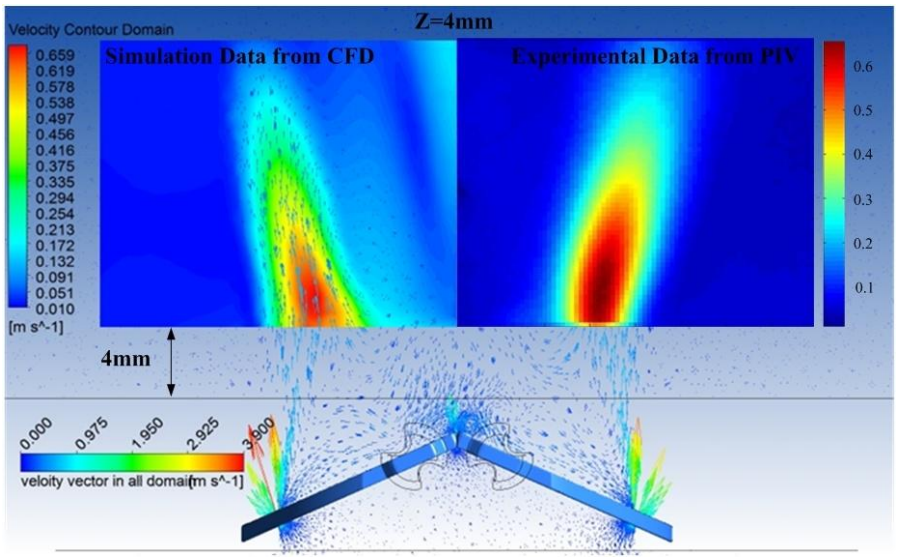

Figure 5.12: comparisons of velocity distribution maps from PIV and CFD on plane Z=4mm

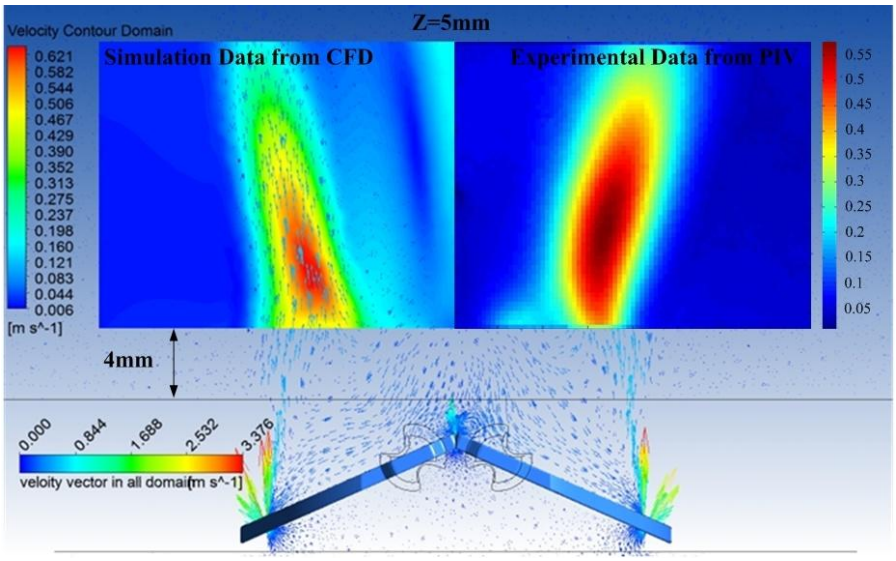

Figure 5.13: comparisons of velocity distribution maps from PIV and CFD on plane Z=5mm

5.2.2 INVESTIGATION HINGE REGIONS WITH CFD

Since the experimental model of valve is not transparent for PIV laser beams, the investigations from PIV experiments cannot be done insight of hinge regions. In this section, the validated numerical data provide the velocity distribution insight hinge.

CFD investigated regions insight of hinge where PIV cannot measure on four following planes, as shown in Figure 5.14:

- 1mm below the primary flat
- Level with primary flat
- 190 μm depth into the hinge socket
- 390 μm depth into the hinge socket

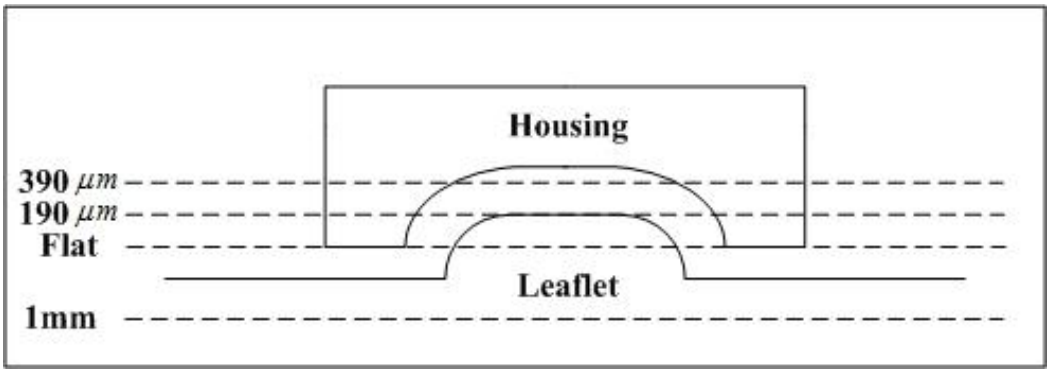

Figure 5.14: measurement sites at four different levels within the hinge

Figure 5.15 (b) shows an onset of leakage flow at flat level when the strong leakage jet was observed in the atrial corner of the hinge. Considering the motion of leaflet during closure, flow was drawn toward the adjacent corner of the hinge with a maximum velocity magnitude of

4.96m/s at this region and a corresponding TSS of 150 Pa. In the lateral corner of hinge, relative high velocity was observed with the magnitude of 4.5m/s. The velocity in the adjacent corner was relative low in the range of 2m/s to 3m/s. The TSS values in the lateral corner reached a maximum value of approximately 320 Pa. The TSS values in the adjacent and atrial corners were observed relatively low in the range of 30 Pa to 50 Pa. Figure 5.15 (c) shows the velocity distributions at 190 μm level. The flow patterns at this level were similar to those at flat level. Two distinct leakage jets could be observed in the adjacent and lateral corners with the magnitude of approximately 5.5m/s. Maximum TSS of 240 Pa were captured in the lateral corner, whereas a peak TSS of 50 Pa was attained in the regions of the other corners. For the remaining regions of hinge, the velocity of relatively low magnitude was obtained at approximately 1m/s. The flow patterns at level 390 μm were illustrated in figure 5.15 (d). The peak leakage velocity magnitudes of around 4.9m/s were obtained in the atrial corner of the hinge with corresponding TSS of 230 Pa. The other parts of hinge region were observed with low velocity magnitude of 2.5m/s and TSS of 40 Pa. The existence of such a high-flow distributions located in the gap between the leaflet and housing could be explained by the fact that the leakage flow was directed over the top of the leaflet pivot.

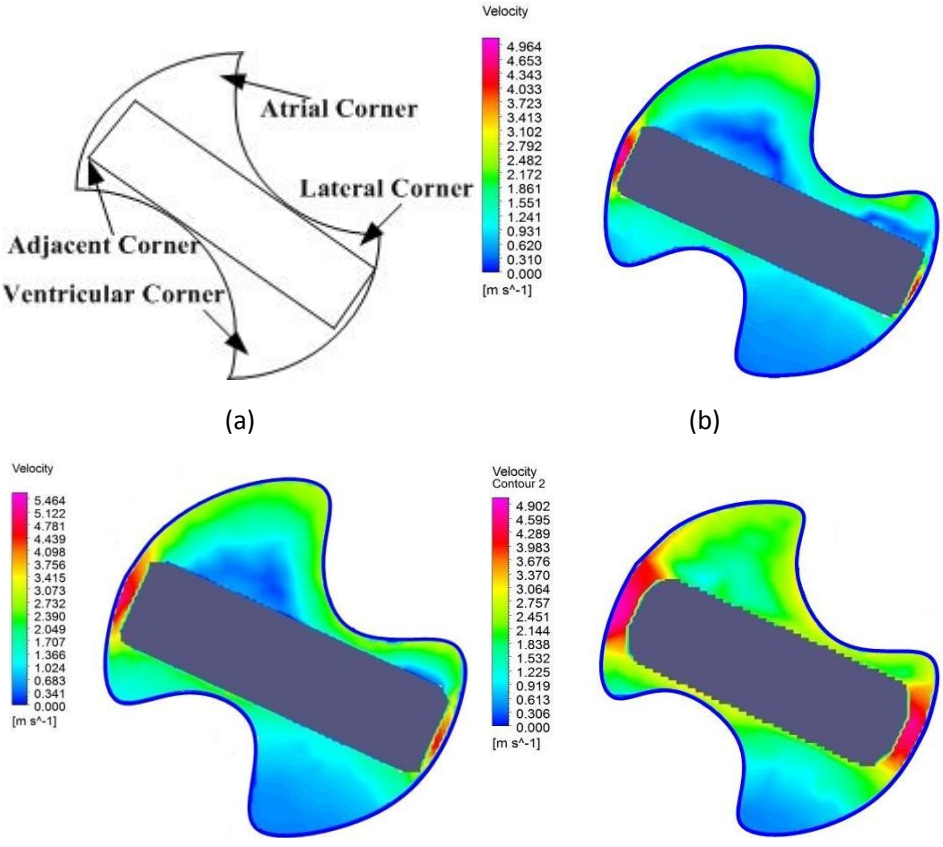

Figure 5.15: flow patterns (velocity magnitude) on different levels: (a) denotation of hinge corners, (b) flat level, (c) 190 μm level, (d) 390 μm level.

Figure 5.16 shows the flow patterns with velocity vectors on the plane 1mm below the primary flat level. It was demonstrated that the magnitude and direction of the flow vectors were the results of the position of the hinge location rather than that of the leaflets. The peak velocity magnitude of jets was observed in the atrial corner with the magnitude of approximately 1.6m/s, whereas two lateral jets of around 0.8m/s were captured directed over to the sides of the hinge. A slight central leakage jet was seen between the gaps of two leaflets.

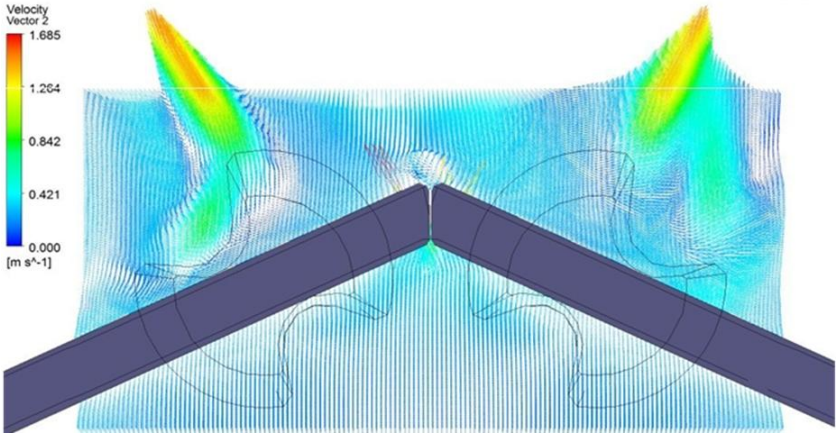

Figure 5.16: flow pattern with velocity vectors on the 1mm level below the flat plane

5.3 CONCLUSION

In this chapter, CFD was used to study PIV leakage jets for BMHV in a simple straight chamber. The setups for simulation strictly followed the experimental parameters. The PIV data from multiple experiments were used as simulation research basis for validations. Two denotes DMV and DVDM were defined to compare results of PIV and CFD quantitatively. Through experimental validations for the selection of simulation model and mesh solutions, the peak value of DMV was controlled below 10%.

Through validation of numerical data, the reliable results from simulation were applied to investigate fluid dynamics of the hinge regions where PIV experiments cannot measure. The peak velocity magnitude of approximately 5m/s was observed through four measured levels with corresponding of maximum TSS 320 Pa.

The results show a good quantitative agreement of the velocity of the leaking jet. However the velocity of the PIV jets is maintained longer than in the CFD simulations. An explanation could be that the used turbulence model and its parameters are suboptimal for this model. Recommendations to future work will exist of trying to optimize the used CFD turbulence model and a comparison of the obtained velocity jet data with the data of Reichardt [155].

Chapter 6
Conclusions and future works

The aim of this thesis was to investigate fluid dynamics characterization of biomedical implantable devices using experimental measurements and numerical simulation.

PIV was applied as experimental tool for 2D visualization of regurgitant flow jets generated by measured targets. The measured targets were including a standard nozzle with typical characteristics for testing mechanical heart valves in regurgitant phase, and two types of BMHVs: valve type 1 with diameter of 21 mm and valve type 2 with diameter of 24mm. In order to improve the knowledge about flow patterns of regurgitation, a custom-built physical model of the regurgitant phase was designed to standardize the test. The design of the model aimed at obtaining a free optical access to the regurgitant jets, in order to apply several 2D and 3D anemometric techniques (LDA, PIV). In the setup of PIV system the standard rules of PIV optimization were strictly followed.

The simulation works were cooperated by ISS and TuCN. The geometries of nozzle and valve models were generates through precise laser scanner. The boundary conditions were set according to the physical parameters from PIV experiment. The selection of models and mesh solutions were achieved with the help of multiple experimental validations.

The standard nozzle was used to evaluate the limitations of the validation for computational fluid dynamics (CFD) as the first phase of our project in assessing blood flow parameters related to medical device safety. The performances of flow condition are conducted over a range of nozzle throat Reynolds number (Re_{throat}) from 1800 to 8000, covering the laminar, transitional, and turbulent flow regimes. The Reynolds numbers for PIV experiments were calculated by measured flow rates, whereas the estimation of Reynolds numbers for CFD was based on the peak velocity existing in the throat region of the nozzle. The results in nozzle tests had good correlations between two methodologies. Through the analysis of nozzle, the combination of PIV and CFD was proved as a reliable tool for further analysis of complicated regurgitant flow jets generated by BMHVs.

PIV was applied to investigate leakage flow fields associated with two typical BMHVs. In the

near-hinge region, the measured peak velocity magnitude for valve type 1 was 0.67m/s with corresponding maximum TSS of 42Pa, whereas the peak velocity for valve type 2 was 0.68m/s with corresponding maximum TSS of 22Pa. The values are reasonably low, especially with regard to the threshold for RBC membrane lysis proposed in the literature (TSS_max, threshold > 600 Pa [122]). However, the TSS may bring risks to platelet activation and blood clotting events because the sensitive value for platelet lysis is 10 Pa [113]-[124]. Repeatability tests were conducted for leakage jets of BMHVs as well. The coefficient of variation was approximately 5%, which proved PIV measurement as a reliable experimental basis for CFD validations. In order to quantitatively define the blood damage due to the artificial implantation, local and global HI (%) were calculated based on local shear stresses and velocities values generated by PIV. The hemolysis potential evaluation requires the exposure time and TSS, based on the comparison of local HI (%) distribution and TSS distribution.

The numerical simulation was analyzed for the valve type 2. The multiple experimental data were used for the validations of the procedure for simulation including the selection of suitable valve models and mesh solutions. The results from experimental model and numerical model have a good agreement to each other (the averaged DMV is less than 10 %). Through validation of numerical data, the reliable results from simulation were applied to investigate fluid dynamics of the hinge regions where PIV experiments cannot be carried out. The peak velocity magnitude of approximately 5m/s was observed through four measured levels with corresponding of maximum TSS 320 Pa.

6.1 FUTURE WORKS

Since PIV and CFD achieved a good quantitative agreement of velocity field distribution of near-hinge regions of valve type 2. Reynolds stress will be calculated according to the same flow field and validated with PIV data to assess the thrombogenic potential of the valve. To obtain a suitable turbulence model in simulation, a comparative examination of velocity field and TSS will be carried out. Different two-equation models and Reynolds stress based models will be considered to compare fluid dynamics of near-hinge regions with PIV. Therefore, the subsequent investigations will use the selected suitable turbulence model. The study of HI of the near-hinge regions and hinge inner regions which is inaccessible to the PIV measurements will also be put into practice.

Further, because the movement of each leaflet during opening and closure was considered to

be purely rotational, about its own predefined axis. 3 Degree of Freedom method will be applied to the leaflet. Hence, the leaflet will be rotated, as well as shifted horizontally or vertically to obtain better results. Since a good solution requires a good quality mesh, mesh independence study will be a challenge work as well.

In the future, the same program will be implemented to valve type 1 to define a standard procedure for sufficient confidence in risk evaluation and mitigation of BMHVs.

REFERENCES

[1] Sutera SP. Flow-Induced Trauma to Blood Cells. Circ Res. 1977 Jul;41(1):2-8.
[2] Grigioni M., D'Avenio G., Morbiducci U., Del Gaudio C., Daniele C. Fluid dynamics studies of cardiovascular medical devices and blood damage prediction. Conf Proc IEEE Eng Med Biol Soc. 2008;2008:1419-22.
[3] Murphy D.W. (2009). The application of passive flow control to bileaflet mechanical heart valve leakage jets (Master's thesis). Georgia Institute of Technology
[4] Marsh, G. W. 1964. Lancet. 2:986.
[5] Saye, H. M., J. V. Dace, D. A. Hundley, S. M. Lewi, W. P. Clelan. 1961. Thorax. 16: 356.
[6] Bacher, R., M. Williams (1970). "Hemolysis in capillary flow." J Lab Clin Med. 79(3): 485-96.
[7] Leverett, L. B., J. D. Hellums, et al. (1972). "Red Blood Cell Damage by Shear Stress." Biophys. J. 12(3): 257-273.
[8] Rooney, J. A. (1970). "Hemolysis Near an Ultrasonically Pulsating Gas Bubble." Science 169(3948): 869-871.
[9] Williams, A. R., D. E. Hughes, et al. (1970). "Hemolysis Near a Transversely Oscillating Wire." Science 169(3948): 871-873.
[10] Sutera, S. P., M. H. Mehrjardi (1975). "Deformation and fragmentation of human red blood cells in turbulent shear flow." Biophys. J. 15(1): 1-10.
[11] Sallam A.M., Hwang N.H. Human red blood cell hemolysis in a turbulent shear flow: contribution of Reynolds shear stresses. Biorheology. 1984; 21(6):783-97.
[12] Grigioni M., Daniele C., D'Avenio G., Barbaro V. A discussion on the threshold limit for hemolysis related to Reynolds shear stress, Journal of Biomechanics 32 (1999) 1107-1112.
[13] Lu P.C., Lai H.C., Liu J.S. A reevaluation and discussion on the threshold limit for hemolysis in a turbulent shear flow. J Biomech. 2001 Oct;34(10):1361-4.
[14] Conti V.R., Nishimura A., Coughlin T.R., Farrell R.W.. Indications for replacement of the Beall-103 and Beall-104 disk valves. Ann Thorac Surg. 1986 Sep; 42(3):315-20.
[15] Skoularigis, J., M. R. Essop, D. Skudicky, S. J. Middlemost, and P. Sareli. Frequency and severity of intravascular hemolysis after left-sided cardiac valve replacement with Medtronic Hall and St. Jude Medical prostheses, and influence of prosthetic type, position, size and number. Am. J. Cardiol. 71:587–591, 1993.
[16] Garcia M.J., Vandervoort P., Stewart W.J., Lytle B.W., Cosgrove D.M., Thomas J,D., Griffin B.P. Mechanisms of Hemolysis With Mitral Prosthetic Regurgitation: study Using Transesophageal Echocardiography and Fluid Dynamic Simulation. J Am Coll Cardiol. 1996 Feb;27(2):399-406.
[17] Mecozzi G., Milano A.D., Carlo M.D., Sorrentino F., Pratali S., Nardi C., Bortolotti U.. Intravascular hemolysis in patients with new-generation prosthetic heart valves: A prospective study. J Thorac Cardiovasc Surg 2002;123:550-556
[18] Suedkamp M., Lercher A.J., Mueller-Riemenschneider F., LaRosee K., Tossios P., Mehlhorn U. Hemolysis parameters of St. Jude Medical: Hemodynamic Plus and Regent valves in aortic position. Int J Cardiol. 2004 May;95(1):89-93.
[19] George J.N. Platelets. Lancet 2000; 355: 1531–9.
[20] Bautista A.P., Buckler P.W., Towler H.M., Dawson A.A., Bennett B. Measurement of

platelet life span in normal subjects and patients with myeloproliferative disease with indium oxine labelled-platelets. Br J Haematol 1984; 58: 679–87.
[21] Felder R., Banton V., Sayre D., Costa J., Baldini M., Kim B. Direct imaging of live human platelets by flash X-ray microscopy. Science 1985; 227: 63–4.
[22] Kamath S., Blann A.D., Lip G.Y.H. Platelet activation: assessment and quantification. Eur Heart J (2001) 22 (17): 1561-1571.
[23] Kaushansky K. Thrombopoietin and hematopoietic stem cell development. Ann NY Acad Sci 1999; 872: 314–19.
[24] Hoak J.C. Platelet and atherosclerosis. Semin Thromb Hemost 1988; 14: 202–5.
[25] Rabbani L.E., Loscalzo J. Recent observations on the role of hemostatic determinants in the development of the atherothrombotic plaque. Atherosclerosis 1994; 105: 1–7.
[26] Yoganathan A.P., Chandran K.B., Sotiropoulos F. Flow in Prosthetic Heart Valves: State-of-the-Art and Future Directions. Ann Biomed Eng. 2005 Dec;33(12):1689-94.
[27] Harker LA, Slichter SJ. Studies of platelet and fibrinogen kinetics in patients with prosthetic heart valves. N Engl J Med. 1970 Dec 10;283(24):1302-5.
[28] Steele P, Weily H, Davies H, Ppppas G, Genton E. Platelet survival time following aortic valve replacement. Circulation. 1975 Feb;51(2):358-62.
[29] Neal WS, Peter PS, Bruce CP. Thromboembolism After Beall Valve Replacement of the Mitral Valve. Ann Thorac Surg 1975;19:33-39
[30] Dale J. Arterial thromboembolic complications in patients with Starr-Edwards aortic ball valve prostheses. Am Heart J. 1976 May;91(5):653-9.
[31] Dale J.Arterial thromboembolic complications in patients with Björk-Shiley and Lillehei-Kaster aortic disc valve prostheses.Am Heart J. 1977 Jun;93(6):715-22.
[32] Pumphrey CW, Dawes J. Elevation of plasma β-thromboglobulin in patients with prosthetic cardiac valves. Thromb Res. 1981 Apr 1-15;22(1-2):147-55.
[33] Czer LS, Matloff JM, Chaux A, De Robertis M, Stewart ME, Gray RJ. The St. Jude valve: Analysis of thromboembolism, warfarin-related hemorrhage, and survival. Am Heart J. 1987 Aug;114(2):389-97.
[34] Bourguignon T, Bergœnd E, Mirza A, Ayegnon G, Neville P, Aupart MR, Marchand M. Risk Factors for Valve-Related Complications after Mechanical Heart Valve Replacement in 505 Patients with Long-Term Follow Up. J Heart Valve Dis. 2011 Nov;20(6):673-80.
[35] Brown CH, Leverett LB, Lewis CW, Alfrey CP Jr, Hellums JD. Morphological, biochemical, and functional changes in human platelets subjected to shear stress. J Lab Clin Med. 1975 Sep;86(3):462-71.
[36] Bernstein EF, Marzec U, Johnston GG. Structural correlates of platelet functional damage by physical forces. Trans Am Soc Artif Intern Organs. 1977;23:617-25.
[37] Anderson GH, Hellums JD, Moake JL, Alfrey CP Jr. Platelet lysis and aggregation in shear fields. Blood Cells. 1978;4(3):499-511.
[38] Ramstacka JM, Zuckermana L, Mockros LF. Shear-induced activation of platelets. Journal of Biomechanics 1979:12(2):113–125
[39] Moake JL, Turner NA, Stathopoulos NA, Nolasco LH, Hellums JD. Involvement of large plasma von Willebrand factor (vWF) multimers and unusually large vWF forms derived from endothelial cells in shear stress-induced platelet aggregation. J Clin Invest 78:1456, 1986
[40] Travis BR, Marzec UM, Ellis JT, Davoodi P, Momin T, Hanson SR, Harker LA, Yoganathan

AP. The sensitivity of indicators of thrombosis initiation to a bileaflet prosthesis leakage stimulus. J Heart Valve Dis. 2001 Mar;10(2):228-38.
[41] Brown CH, Leverett LB, Lewis CW, Alfrey CP Jr, Hellums JD. Morphological, biochemical, and functional changes in human platelets subjected to shear stress. J Lab Clin Med. 1975 Sep;86(3):462-71.
[42] D. Bluestein. Research approaches for studying flow induced thromboembolic complications in blood recirculating devices. Expert Rev Med Devices. 2004 Sep; 1 (1):65-80
[43] L.J. Wurzinger, P. Blasberg and H. Schmid-Schönbein. Towards a concept of thrombosis in accelerated flow: Rheology, fluid dynamics, and biochemistry. Biorheology. 1985;22(5):437-50
[44] Yoganathan AP, Corcoran WH, Harrison EC. In vitro velocity measurements in the vicinity of aortic prostheses. Journal of Biomechanics. 1979:12(2):135–152
[45] Chandran KB, Cabell GN, Khalighi B, Chen CJ. Pulsatile flow past aortic valve bioprostheses in a model human aorta. J Biomech. 1984;17(8):609-19.
[46] Chandran KB, Khalighi B, Chen CJ.Experimental study of physiological pulsatile flow past valve prostheses in a model of human aorta—I. Caged ball valves. J Biomech. 1985;18(10):763-72.
[47] Chandran KB, Khalighi B, Chen CJ.Experimental study of physiological pulsatile flow past valve prostheses in a model of human aorta—II. Tilting disc valves and the effect of orientation. J Biomech. 1985;18(10):773-80.
[48] Yoganathan AP, Woo Y, H. Sung. Turbulent shear stress measurements in the vicinity of aortic heart valve prostheses. J. Biomech. 19:433–442, 1986
[49] Hanle DD, Harrison EC, Yoganathan AP, Allen DT, Corcoran WH. In vitro flow dynamics of four prosthetic aortic valves: A comparative analysis. J Biomech. 1989;22(6-7):597-607.
[50] Schoephoerster RT, Chandran KB.Velocity and turbulence measurements past mitrial valve prostheses in a model left ventricle. J Biomech. 1991;24(7):549-62.
[51] Hans N, Peter KP, Michael HJ, Erik MP, Poul ER. TURBULENT STRESSES DOWNSTREAM OF 3 MECHANICAL AORTIC-VALVE PROSTHESES IN HUMAN-BEINGS. J Thorac Cardiovasc Surg 1994;107:438-0446
[52] Maymir JC, Deutsch S, Meyer RS, Geselowitz DB, Tarbell JM. Effects of tilting disk heart valve gap width on regurgitant flow through an artificial heart mitral valve. Artif Organs. 1997 Sep;21(9):1014-25.
[53] Travis, BR, Ellis, JT, Saxena, R, Yoganathan, AP. Differences in local hemodynamics of bileaflet prosthetic heart valves: The effect of increased orifice area. Proceedings of the 20th Annual International Conference of the IEEE 1998. vol.1:371 - 374
[54] J.T. Ellis, B.R. Travis and A.P. Yoganathan. An in vitro study of the hinge and near-field forward flow dynamics of the St. Jude Medical® Regent™ bileaflet mechanical heart valve. Annals of Biomedical Engineering. vol.28, no. 5 (2000), 524-532
[55] J.T. Ellis and A.P. Yoganathan. A comparison of the hinge and near-hinge flow fields of the St Jude Medical Hemodynamic Plus and Regent bileaflet mechanical heart valves. J Thorac Cardiovasc Surg. 2000;119:83-93.
[56] H.L. Leo, Z.M. He, J.T. Ellis and A.P. Yoganathan. Microflow fields in the hinge region of the CarboMedics bileaflet mechanical heart valve design. J Thorac Cardiovasc Surg. 2002 Sep;124(3):561-74.
[57] H.A. Simon, H.L. Leo, J. Carberry and A.P. Yoganathan. Comparison of the hinge flow

fields of two bileaflet mechanical heart valves under aortic and mitral conditions. Ann Biomed Eng. 2004 Dec;32(12):1607-17.
[58] H.A. Simon (2004). Influence of the implant location on the hinge and leakage flow fields through bileaflet mechanical heart valves (Master's thesis). Georgia Institute of Technology
[59] Manning KB, Herbertson LH, Fontaine AA, Deutsch S.A detailed fluid mechanics study of tilting disk mechanical heart valve closure and the implications to blood damage. J Biomech Eng. 2008 Aug;130(4):041001.
[60] Lim WL, Chew YT, Chew TC, Low HT.Steady flow dynamics of prosthetic aortic heart valves: a comparative evaluation with PIV techniques. J Biomech. 1998 May;31(5):411-21.
[61] Lim WL, Chew YT, Chew TC, Low HT. Pulsatile flow studies of a porcine bioprosthetic aortic valve in vitro: PIV measurements and shear-induced blood damage. J Biomech. 2001 Nov;34(11):1417-27.
[62] K.B. Manning, V. Kini, A.A. Fontaine, S. Deutsch and J.M. Tarbell. Regurgitant flow field characteristics of the St.Jude bilealet mechanical heart valve under physiologic pulsatile flow using particle image velocimetry. Artif Organs. 2003 Sep;27(9):840-6.
[63] Lu PC, Liu JS, Huang RH, Lo CW, Lai HC, Hwang NH.The closing behavior of mechanical aortic heart valve prostheses. ASAIO J. 2004 Jul-Aug;50(4):294-300.
[64] T. Akutsu and T. Fukuda. Time-resolved particle image velocimetry and laser doppler anemometry study of the turbulent flow field of bileaflet mechanical mitral prostheses. J Artif Organs. 2005;8(3):171-83.
[65] Y.B. Shi, J.H. Yeo, Y. Zhao and H.C. Hwang. Particle image velocimetry study of pulsatile flow in bileaflet mechanical heart valves with image compensation method. J Biol Phys. 2006 December; 32(6): 531–551.
[66] Kaminsky R, Morbiducci U, Rossi M, Scalise L, Verdonck P, Grigioni M.Time-resolved PIV technique for high temporal resolution measurement of mechanical prosthetic aortic valve fluid dynamics. Int J Artif Organs. 2007 Feb;30(2):153-62.
[67] D.W. Murphy (2009). The application of passive flow control to bileaflet mechanical heart valve leakage jets (Master's thesis). Georgia Institute of Technology
[68] D. Amatya, D.R. Troolin and E.K. Longmire. 3D3C velocity measurements downstream of artificial heart valves. 8TH INTERNATIONAL SYMPOSIUM ON PARTICLE IMAGE VELOCIMETRY - PIV09. Melbourne, Victoria, Australia, August 25-28, 2009
[69] Li CP, Lo CW, Lu PC. Estimation of Viscous Dissipative Stresses Induced by a Mechanical Heart Valve Using PIV Data. Ann Biomed Eng. 2010 Mar; 38 (3):903-16. Epub 2009 Dec 18.
[70] Akutsu T, Matsumoto A.Influence of three mechanical bileaflet prosthetic valve designs on the three-dimensional flow field inside a simulated aorta. J Artif Organs. 2010 Dec;13(4):207-17.
[71] Hutchison C, Sullivan P, Ethier CR. Measurements of steady flow through a bileaflet mechanical heart valve using stereoscopic PIV. Med Biol Eng Comput. 2011 Mar;49(3):325-35.
[72] Li CP, Chen SF, Lo CW, Lu PC. Turbulence Characteristics Downstream of a New Trileaflet Mechanical Heart Valve. ASAIO J. 2011 May-Jun;57(3):188-96.
[73] C. Hutchison, P. Sullivan and C.R. Ethier. Measurements of steady flow through a bileaflet mechanical heart valve using stereoscopic PIV. Med Biol Eng Comput. 2011 Mar;49(3):325-35
[74] Stühle S, Wendt D, Houl G, Wendt H, Schlamann M, Thielmann M, Jakob H, Kowalczyk W.In-Vitro Investigation of the Hemodynamics of the Edwards Sapien (TM) Transcatheter Heart Valve. J Heart Valve Dis. 2011 Jan;20(1):53-63.

[75] Alessandro Bellofiore, Eilis M. Donohue and Nathan J. Quinlan. Scale-up of an unsteady flow field for enhanced spatial and temporal resolution of PIV measurements: application to leaflet wake flow in a mechanical heart valve. Exp. Fluids (2011) 51:161-176
[76] Williams GA, Labovitz AJ. Doppler hemodynamic evaluation of prosthetic (Starr-Edwards and Björk-Shiley) and Bioprosthetic (Hancock and Carpentier-Edwards) cardiac valves. Am J Cardiol. 1985 Aug 1;56(4):325-32.
[77] Reimold SC, Yoganathan AP, Sung HW, Cohn LH, Sutton MG, Lee RT.Doppler echocardiographic study of porcine bioprosthetic heart valves in the aortic valve position in patients without evidence of cardiac dysfunction. Am J Cardiol. 1991 Mar 15;67(7):611-5.
[78] Chambers J, Cross J, Deverall P, Sowton E.Echocardiographic Description of the CarboMedics Bileaflet Prosthetic Heart Valve. J Am Coll Cardiol. 1993 Feb;21(2):398-405.
[79] Cape EG, Sung HW, Yoganathan AP.HEMODYNAMIC ASSESSMENT OF CARBOMEDICS BILEAFLET HEART VALVES BY ULTRASOUND: STUDIES IN THE AORTIC AND MITRAL POSITIONS. Ultrasound Med Biol. 1996;22(4):421-30.
[80] Otto CM, Pearlman AS, Comess KA, Reamer RP, Janko CL, Huntsman LL.Determination of the Stenotic Aortic Valve Area in Adults Using Doppler Echocardiography. J Am Coll Cardiol. 1986 Mar;7(3):509-17.
[81] Flachskampf FA, O'Shea JP, Griffin BP, Guerrero L, Weyman AE, Thomas JD. Patterns of Normal Transvalvular Regurgitant in Mechanical Valve Prostheses. J Am Coll Cardiol. 1991 Nov 15;18(6):1493-8.
[82] Baumgartner H, Khan S, DeRobertis M, Czer L, Maurer G. Effect of Prosthetic Aortic Valve Design on the Doppler-Catheter Gradient Correlation: An In Vitro Study of Normal St, Jude, Medtronic-Hall, Starr-Edwards and Hancock Valves. J Am Coll Cardiol. 1992 Feb;19(2):324-32.
[83] Bitar JN, Lechin ME, Salazar G, Zoghbi WA.Doppler Echocardiographic Assessment with the Continuity Equation of St. Jude Medical Mechanical Prostheses in the Mitral Valve Position. Am J Cardiol. 1995 Aug 1;76(4):287-93.
[84] Bech-Hanssen O, Caidahl K, Wallentin I, Ask P, Wranne B.Assessment of effective orifice area of prosthetic aortic valves with Doppler echocardiography: An in vivo and in vitro study. J Thorac Cardiovasc Surg. 2001 Aug;122(2):287-95.
[85] Hasenkam JM, Giersiepen M, Reul H.Three-dimensional visualization of velocity fields downstream of six mechanical aortic valves in a pulsatile flow model. J Biomech. 1988;21(8):647-61.
[86] Nygaard H, Giersiepen M, Hasenkam JM, Reul H, Paulsen PK, Rovsing PE, Westphal D.Two-dimensional color-mapping of turbulent shear stress distribution downstream of two aortic bioprosthetic valves in vitro. J Biomech. 1992 Apr;25(4):429-40.
[87] Fontaine AA, Heinrich RS, Walker PG, Pedersen EM, Scheidegger MB, Boesiger P, Walton SP, Yoganathan AP. Comparison of magnetic resonance imaging and laser Doppler anemometry velocity measurements downstream of replacement heart valves: Implications for in vivo assessment of prosthetic valve function. J Heart Valve Dis. 1996 Jan;5(1):66-73.
[88] Ringgaard S, Botnar RM, Djurhuus C, Stodkilde-Jorgensen H, Hasenkam JM, Boesiger P, Pedersen EM.High-resolution assessment of velocity fields and shear stresses distal to prosthetic heart valves using high-field magnetic resonance imaging. J Heart Valve Dis. 1999 Jan;8(1):96-103.
[89] Houlind K, Eschen O, Pedersen EM, Jensen T, Hasenkam JM, Paulsen PK. Magnetic

resonance imaging of blood velocity distribution around St Jude Medical aortic valves in patients. J Heart Valve Dis. 1996 Sep;5(5):511-7.
[90] Kvitting JP, Dyverfeldt P, Sigfridsson A, Franzén S, Wigström L, Bolger AF, Ebbers T.In Vitro Assessment of Flow Patterns and Turbulence Intensity in Prosthetic Heart Valves Using Generalized Phase-Contrast MRI. J Magn Reson Imaging. 2010 May;31(5):1075-80.
[91] T.M. Healy, A.A. Fontaine, J.T. Ellis, S.P. Walton and A.P. Yoganathan. Visualization of the hinge flow in a 5:1 scaled model of the Medtronic parallel bileaflet heart valve prosthesis. Experiments in Fluids. vol. 25, no. 5-6 (1998), 512-518
[92] Kleine P, Scherer M, Abdel-Rahman U, Klesius AA, Ackermann H, Moritz A.Effect of mechanical aortic valve orientation on coronary artery flow: Comparison of tilting disc versus bileaflet prostheses in pigs. J Thorac Cardiovasc Surg. 2002 Nov;124(5):925-32.
[93] Nyboe C, Funder JA, Smerup MH, Nygaard H, Hasenkam JM.Turbulent stress measurements downstream of threebileaflet heart valve designs in pigs. Eur J Cardiothorac Surg. 2006 Jun;29(6):1008-13.
[94] M. Grigioni, C. Daniele, U. Morbiducci, C. Del Gaudio, G. D'Avenio, A. Balducci, D. Di Meo and V. Barbaro. Laser Vibrometry as investigational tool for mechanical heart valves kinematics: preliminary investigation, 2003
[95] Malvern, L E. Introduction to the mechnics of a continous medium. Transport Research Laboratory. 1969
[96] RD Keane, RJ Adrian. The PIV rules of thumb were developed by Keane and Adrian in Optimization of particle image velocimeters. Part 1: Double pulsed systems Measurement Science and Technology 1.Measurement Science and Technology, 1999
[97] Batchelor, G. (2000). *Introduction to Fluid Mechanics*.
[98] Geankoplis, Christie John (2003). Transport Processes and Separation Process Principles. *Prentice Hall Professional Technical Reference. ISBN 0-13-101367-X*.
[99] Turbulence theory gets a bit choppy. *USA Today*. September 10, 2006.
[100] Multilaboratory Particle Image Velocimetry Analysis of the FDA Benchmark Nozzle Model to Support Validation of Computational Fluid Dynamics Simulations
[101] Glauert, M.B., 1956. The wall jet. J. Fluid Mech. 1, 625–643.
[102] Reddy, Gorla, R.S., Jeng, D.R., 1971. Laminar plane wall jet. In: Proceedings of the 12th Midwestern Mechanics Conference, Paris, France, pp. 137–151.
[103] Schwarz, W.H., Cosart, W.P., 1961. The two-dimensional turbulent wall jet. J. Fluid Mech. 10, 481–495.
[104] Rajaratnam, N., 1976. Turbulent Jets. Elsevier, Amsterdam, The Netherlands. pp. 214–216.
[105] Grigioni, M., C. Daniele, G. D'Avenio, and V. Barbaro. Evaluation of the surface-averaged load exerted on a blood element by the Reynolds shear stress field provided by artificial cardiovascular devices. J. Biomech. 35(12): 1613–1622, 2002.
[106] Travis, B. R., H. L. Leo, P. A. Shah, D. H. Frakes, and A. P. Yoganathan. An analysis of turbulent shear stresses in leakage flow through a bileaflet mechanical prostheses. J. Biomech. Eng. 124:155, 2002.
[107] Hellums, J. D., and C. H. Brown. Blood cell damage by mechanical forces. In: Cardiovascular Flow Dynamics and Measurements, edited by N. H. C. Hwang and N. A. Normann. Baltimore: University Park Press, 1977, pp. 799–823.
[108] Manning KB, Kini V, Fontaine AA, Deutsch S, Tarbell JM. Regurgitant Flow Field

Characteristics of the St. Jude Bileaflet Mechanical Heart Valve under Physiologic Pulsatile Flow Using Particle Image Velocimetry. Artificial Organs, 2003;27(9):840-846.
[109] Leo HL, Simon HA, Dasi LP, Yoganathan AP. Effect of hinge gap width on the microflow structures in 27-mm bileaflet mechanical heart valves. J Heart Valve Dis. 2006 Nov; 15(6):800-8.
[110] Nallamothu R. K., Li Y., Rafiroiu D., Diaz V., Narracott A., Lawford P. et al. Multi-physics and multi-scale computational evaluation of the thrombogenic and cavitational potential of a bileaflet mechanical heart valve. 2011 IFMBE Proc. 36(4)/298-305.
[111] Morse D, Steiner RM, Fernandez J. Cardiac valve identification atlas and guide. In: Dryden Morse RM, Sa JF, editors. Guide to prosthetic cardiac valves. New York: Springer-Verlag, 1985. pp. 257– 346.
[112] St. Jude Medical Products. St. Jude Medical. 2002. Ref type: Electronic Citation
[113] Rashtian MY, Stevenson DM, Allen DT, Yoganathan AP, Harrison EC, Edmiston WA, Faughan P, Rahimtoola SH. Flow characteristics of four commonly used mechanical heart valves. Am J Cardiol 58: 743– 52.
[114] Akins CW. Results with mechanical cardiac valvular prostheses. Ann Thorac Surg 60:1836– 44.
[115] Butany J, Ahluwalia MS, Munroe C, Fayet C, Ahn C, Blit P, Kepron C, Cusimano RJ, Leask RL. "Mechanical heart valve prostheses: identification and evaluation". Cardiovasc Pathol. 2003 Nov-Dec; 12(6):322-44.
[116] Rizzoli G, Guglielmi C, Toscano G, Pistorio V, Vendramin I, Bottio T, Thiene G, Casarotto D. Reoperations for acute prosthetic thrombosis and pannus: an assessment of rates, relationship and risk. Eur J Cardiothorac Surg 16:74– 80.
[117] de Brux JL, Subayi JB, Binuani P, Laporte J. Doppler-echocardio- graphic assessment of the carbomedics supra-annular ''Top-Hat'' prosthetic heart valve in the aortic position. J Heart Valve Dis 5(Suppl 3): S336–8.
[118] cts.net website. Cardiothoracic Surgery website. 2002. Ref type: Electronic Citation.
[119] Fiane AE, Geiran OR, Svennevig JL. Up to eight years' follow-up of 997 patients receiving the CarboMedics prosthetic heart valve. Ann Thorac Surg 66:443– 8
[120] Jamieson WR, Fradet GJ, Miyagishima RT, Henderson C, Brownlee RT, Zhang J, Germann E. CarboMedics mechanical prosthesis: performance at eight years. J Heart Valve Dis 96:78-87.
[121] Dalrymple-Hay MJ, Pearce RK, Dawkins S, Alexiou C, Haw MP, Livesey SA, Monro JL. Mid-term results with 1,503 CarboMedics mechanical valve implants. J Heart Valve Dis 9:389-95.
[122] M. Grigioni, C. Daniele, G. D'Avenio, V. Barbaro, A discussion on the threshold limit for hemolysis related to Reynolds shear stress. Journal of Biomechanics, 1999; 32; 1107-1112.
[123] J. D. Hellums. 1993 Whitaker lecture: Biorheology in thrombosis research. Ann. Biomed. Eng. 22(5):445–455, 1994.
[124] S. P Sutera. Flow-induced trauma to blood cells. Circ. Res. 41(1):2–8, 1977.
[125] K. Fraser, M. Taskin, T. Zhang, B. Griffths, and Z. Wu. Comparison of shear stress, residence time and lagrangian estimates of hemolysis in different ventricular assist devices. In 26th Southern Biomedical Engineering Conference, SBEC 2010, April 30 - May 2, volume 32, pages 548-551, 2010.

[126] M. Lieber and T. Steck. A description of the holes in human erythrocyte membrane ghosts. The Journal of Biological Chemistry, 257(19):11651-11659, 1982
[127] S. S. Lee, K. Ahn, S. J. Lee, K. Sun, P. Goedhart, and M. Hardeman. Shear induced damage of red blood cells monitored by the decrease of their deformability. Korea-Australia Rheology Journal, 16(3):141-146, 2004.
[128] P. Blackshear, F. Dorman, and J. Steinbach. Some mechanical effects that influence haemolysis. Transactions of the American Society of Artificial Internal Organs, 11(112), 1965.
[129] Giersiepen M, Wurzinger L.J, Opitz R, Reul H. Estimation of shear stress related blood damage in heart valve prostheses: in vitro comparision of 25 aortic valves. Int J Artif Org, 1990; 13(5): 300-306.
[130] G. Heuser and R. Opitz. A couette viscometer for short time shearing in blood. Biorheology, 17:17-24, 1980.
[131] M. Taskin, K. Fraser, T. Zhang, B. Gellman, A. Fleischli, K. Dasse, B. Grifth, and Z. Wu. Computational characterization of flow and hemolytic performance of the UltraMag blood pump for circulatory support. Artificial Organs, 34(12):1099-1113, 2010.
[132] Pinotti, M., and Rosa, E. S., 1995, "Computational Prediction of Hemolysis in a Centrifugal Ventricular Assist Device," Artif. Organs, 19(3), pp. 267–273.
[133] Grigioni, M., Daniele, C., D'Avenio, G., and Barbaro, V. A., 1999, "Discussion on the Threshold Limit for Hemolysis Related to Reynolds Shear Stress," J. Biomech., 32, pp. 1107–1112.
[134] Burgreen, G. W., Antaki, J. F., Wu, Z. J., and Holmes, A. J., 2001, "Computational Fluid Dynamics as a Development Tool for Rotary Blood Pumps," Artif. Organs, 255, pp. 336–340.
[135] De Wachter, D., and Verdonck, P., 2002, "Numerical Calculation of Hemolysis Levels in Peripheral Hemodialysis Cannulas," Artif. Organs, 26(7), pp. 576-582.
[136] Yano, T., Sekine, K., Mitoh, A., Mitamura, Y., Okamoto, E., Kim, D. W., Nishimura, I., Murabayashi, S., and Yozu, R., 2003, "An Estimation Method of Hemolysis Within an Axial Flow Blood Pump by Computational Fluid Dynamics Analysis," Artif. Organs, 27(10), pp. 920–925.
[137] Arvand, A., Hormes, M., and Reul, H., 2005, "A Validated Computational Fluid Dynamics Model to Estimate Hemolysis in a Rotary Blood Pump," Artif. Organs, 29(7), pp. 531–540.
[138] Behbahani, M., Behr, M., Hormes, M., Steinseifer, U., Arora, D., Coronado, O., and Pasquali, M., 2009, "A Review of Computational Fluid Dynamics Analysis of Blood Pumps," Eur. J. Appl. Math., 20(04), pp. 363–397.
[139] Wootton, D. M., Markou, C. P., Hanson, S. R., and Ku, D. N., 2001, "A Mechanistic Model of Acute Platelet Accumulation in Thrombogenic Stenoses," Ann. Biomed. Eng., 29(4), pp. 321–329.
[140] Goodman, P. D., Barlow, E. T., Crapo, P. M., Mohammad, S. F., and Solen, K. A., 2005, "Computational Model of Device-Induced Thrombosis and Thromboembolism," Ann. Biomed. Eng., 33(6), pp. 780–797.
[141] Sorensen, E. N., Burgreen, G. W., Wagner, W. R., and Antaki, J. F., 1999,"Computational Simulation of Platelet Deposition and Activation: I. Model Development and Properties," Ann. Biomed. Eng., 27, pp. 436–448.
[142] Fallon, A. M., Dasi, L. P., Marzec, U. M., Hanson, S. R., and Yoganathan, A. P., 2008, "Procoagulant Properties of Flow Fields in Stenotic and Expansive Orifices," Ann. Biomed. Eng.,

36(1), pp. 1–13.
[143] Tamagawa, M., Kaneda, H., Hiramoto, M., and Nagahama, S., 2009, “Simulation of Thrombus Formation in Shear Flows Using Lattice Boltzmann Method,” Artif. Organs, 33(8), pp. 604–610.
[144] Richardson, E., 1975, “Applications of a Theoretical Model for Haemolysis in Shear Flow,” Biorheology, 12(1), pp. 27–37.
[145] Giersiepen, M., Wurzinger, L. J., Opitz, R., and Reul, H., 1990, “Estimation of Shear Stress-Related Blood Damage in Heart Valve Prostheses—In Vitro Comparison of 25 Aortic Valves,” Int. J. Artif. Organs, 13(5), pp. 300–306.
[146] Bludszuweit, C., 1995, “Model for a General Mechanical Blood Damage Prediction,” Artif. Organs, 19(7), pp. 583–589.
[147] Gu, L., and Smith, W., 2005, “Evaluation of Computational Models for Hemolysis Estimation,” ASAIO J., 51(3), pp. 202–207.
[148] Hentschel, B., Tedjo, I., Probst, M., Wolter, M., Behr, M., Bischof, C., and Kuhlen, T., 2008, “Interactive Blood Damage Analysis for Ventricular Assist Devices,” IEEE Trans. Vis. Comput. Graph., 14(6), pp. 1515–1522.
[149] Hariharan P, Giarra M, Reddy V, Day SW, Manning KB, Deutsch S, Stewart SF, Myers MR, Berman MR, Burgreen GW, Paterson EG, Malinauskas RA. Multilaboratory particle image velocimetry analysis of the FDA benchmark nozzle model to support validation of computational fluid dynamics simulations. J Biomech Eng. 2011 Apr; 133(4):041002. doi: 10.1115/1.4003440.
[150] Rafiroiu D, Ciupa R (2009) Medical devices design in cardiovascular applications. Current and future trends at Cluj Napoca Technical University. Journal of Nonlinear Optics, Quantum Optics, 39 (2-3) 101-115.
[151] www.ansys.com
[152] Wilcox, David C (1998). "Turbulence Modeling for CFD". Second edition. Anaheim: DCW Industries, 1998. pp. 174.
[153] Jones, W. P., and Launder, B. E. (1972), "The Prediction of Laminarization with a Two-Equation Model of Turbulence", International Journal of Heat and Mass Transfer, vol. 15, 1972, pp. 301-314.
[154] Launder, B. E., and Sharma, B. I. (1974), "Application of the Energy Dissipation Model of Turbulence to the Calculation of Flow Near a Spinning Disc", Letters in Heat and Mass Transfer, vol. 1, no. 2, pp. 131-138.
[155] Reichardt H., Gesetzmassigkeiten der freien Turbulenz, VDI-Forschungsheft 414 (1942), 2nd ed. 1951

APPENDIX

A 1. VALVE TYPE 1

A 1.1 MULTIPLE EXPERIMENTAL RESULTS ON PLANE Z=1MM

A 1.1.1 VELOCITY DISTRIBUTION

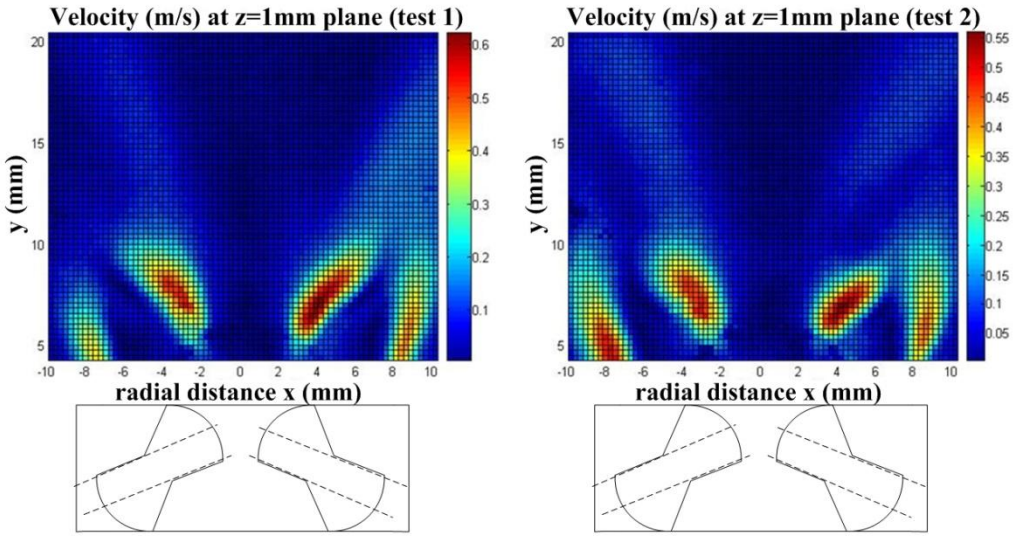

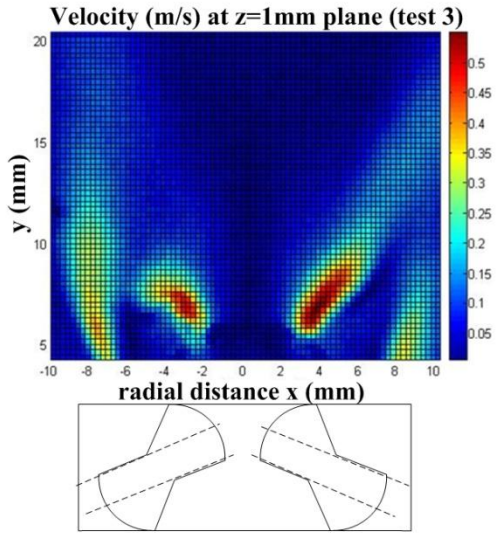

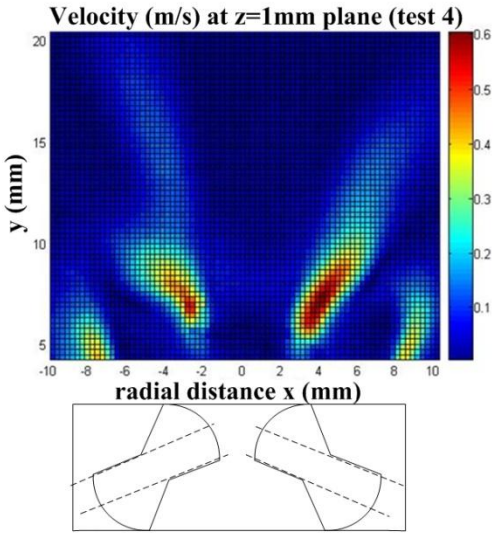

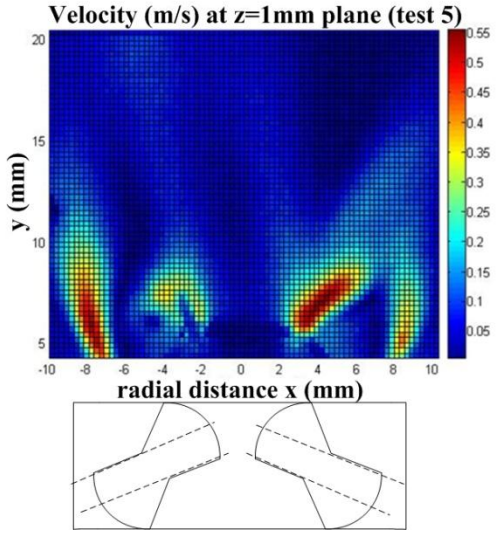

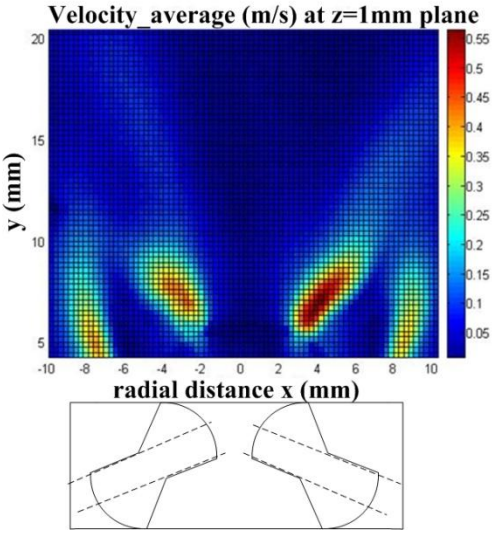

A 1.1.2 VELOCITY PROFILES AT DIFFERENT DOWNSTREAM LOCATIONS

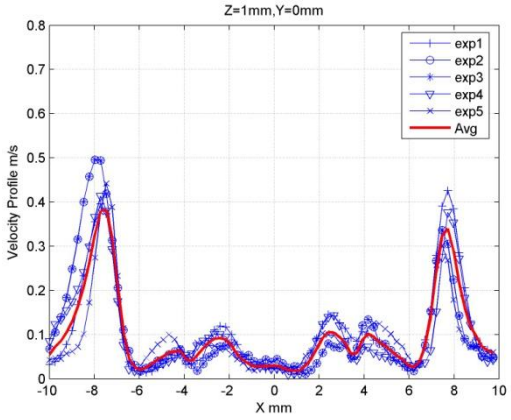

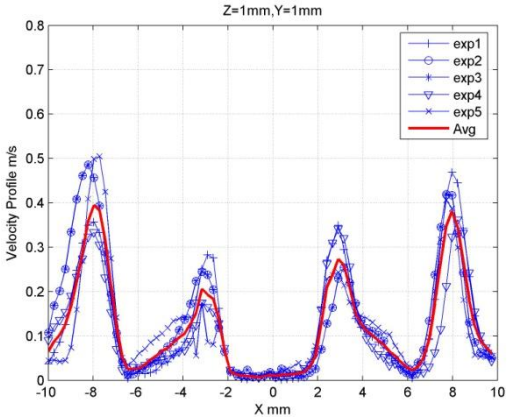

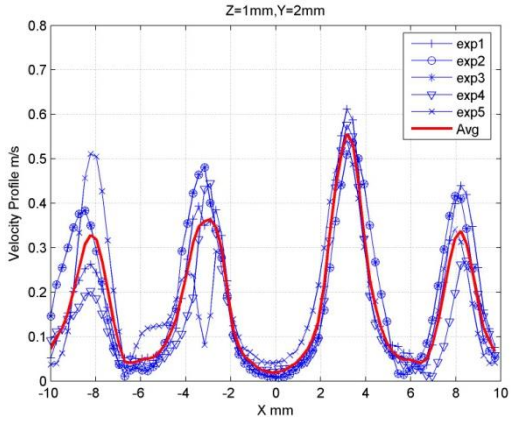

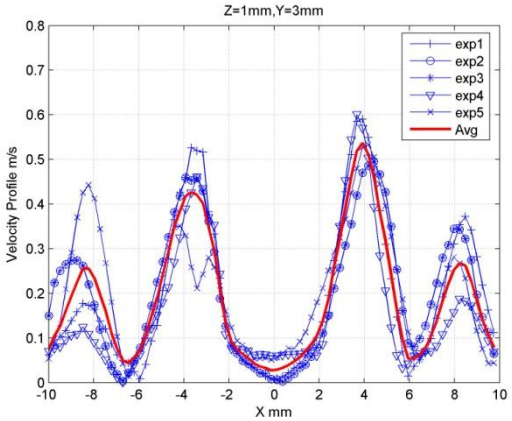

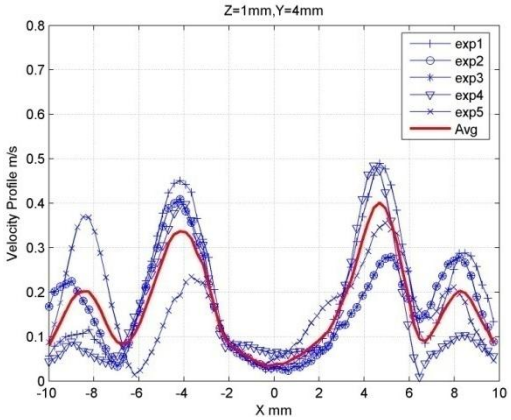

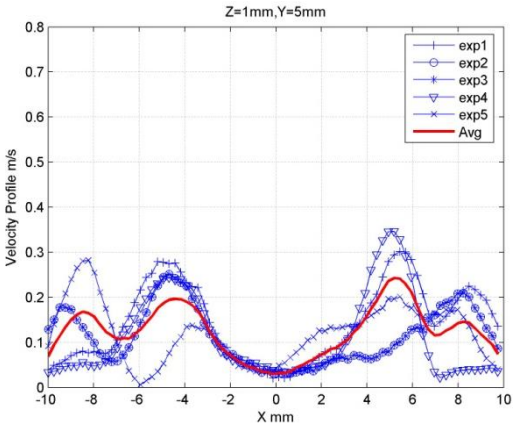

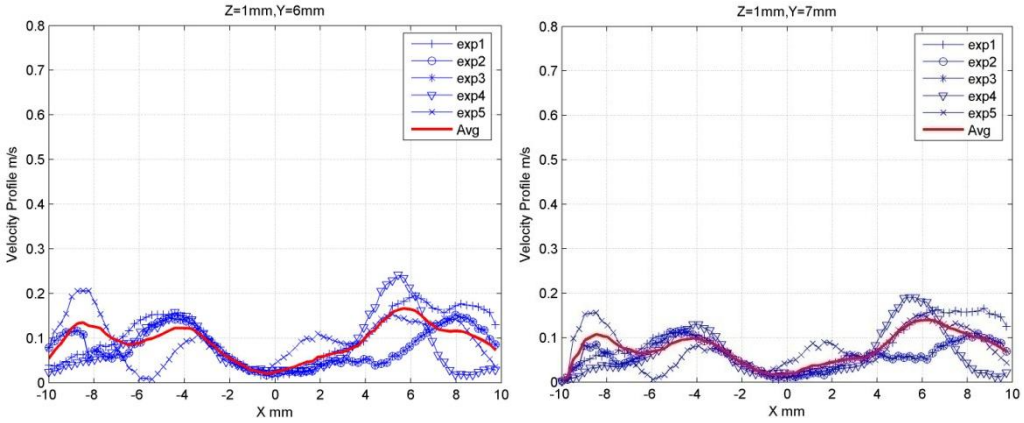
Z=1mm,Y=6mm
Velocity Profile m/s
X mm
exp1
exp2
exp3
exp4
exp5
Avg
Z=1mm,Y=7mm
Velocity Profile m/s
X mm
exp1
exp2
exp3
exp4
exp5
Avg

A 1.1.3 TSS DISTRIBUTION

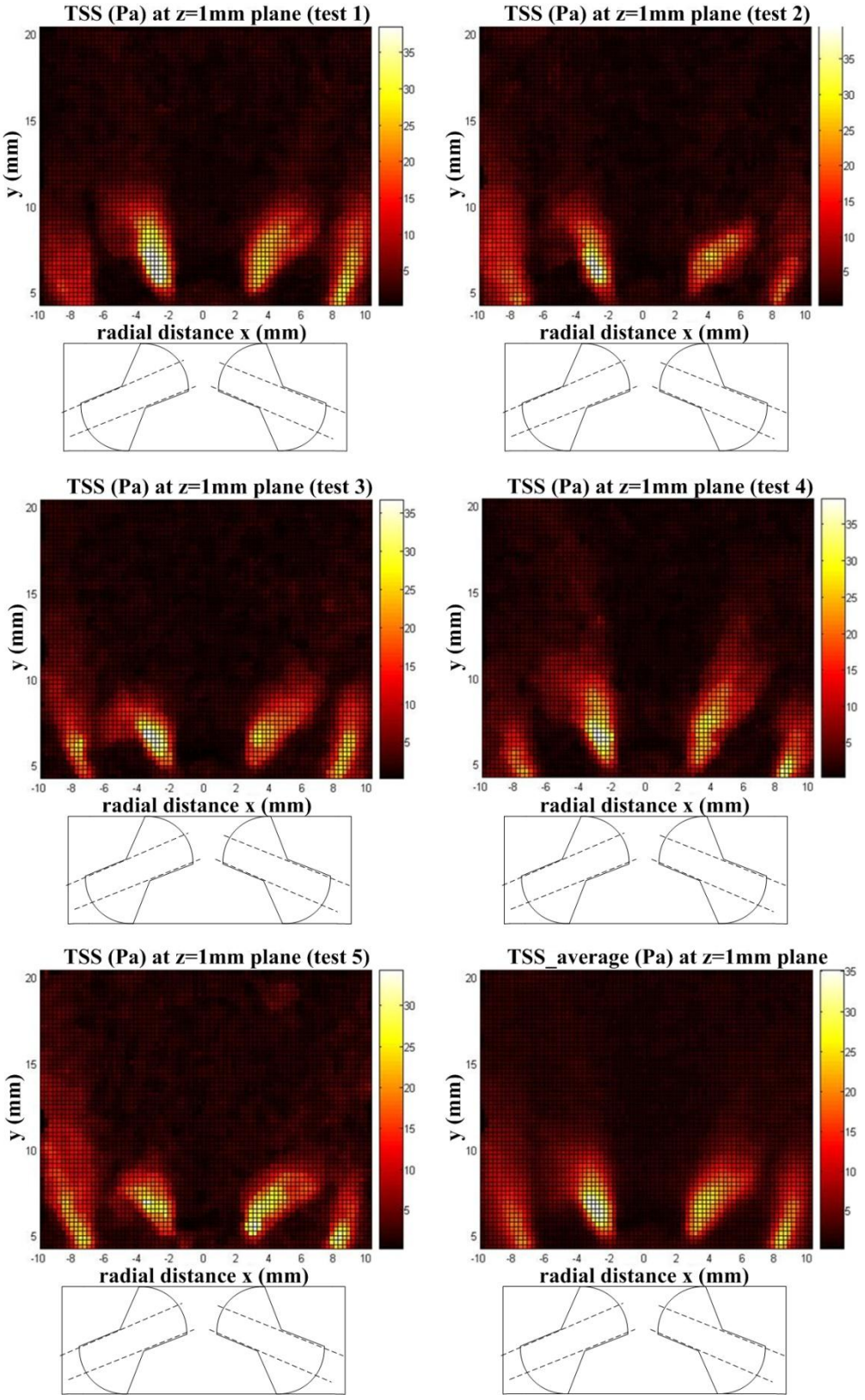

A 1.2 MULTIPLE EXPERIMENTAL RESULTS ON PLANE Z=2MM

A 1.2.1 VELOCITY DISTRIBUTION

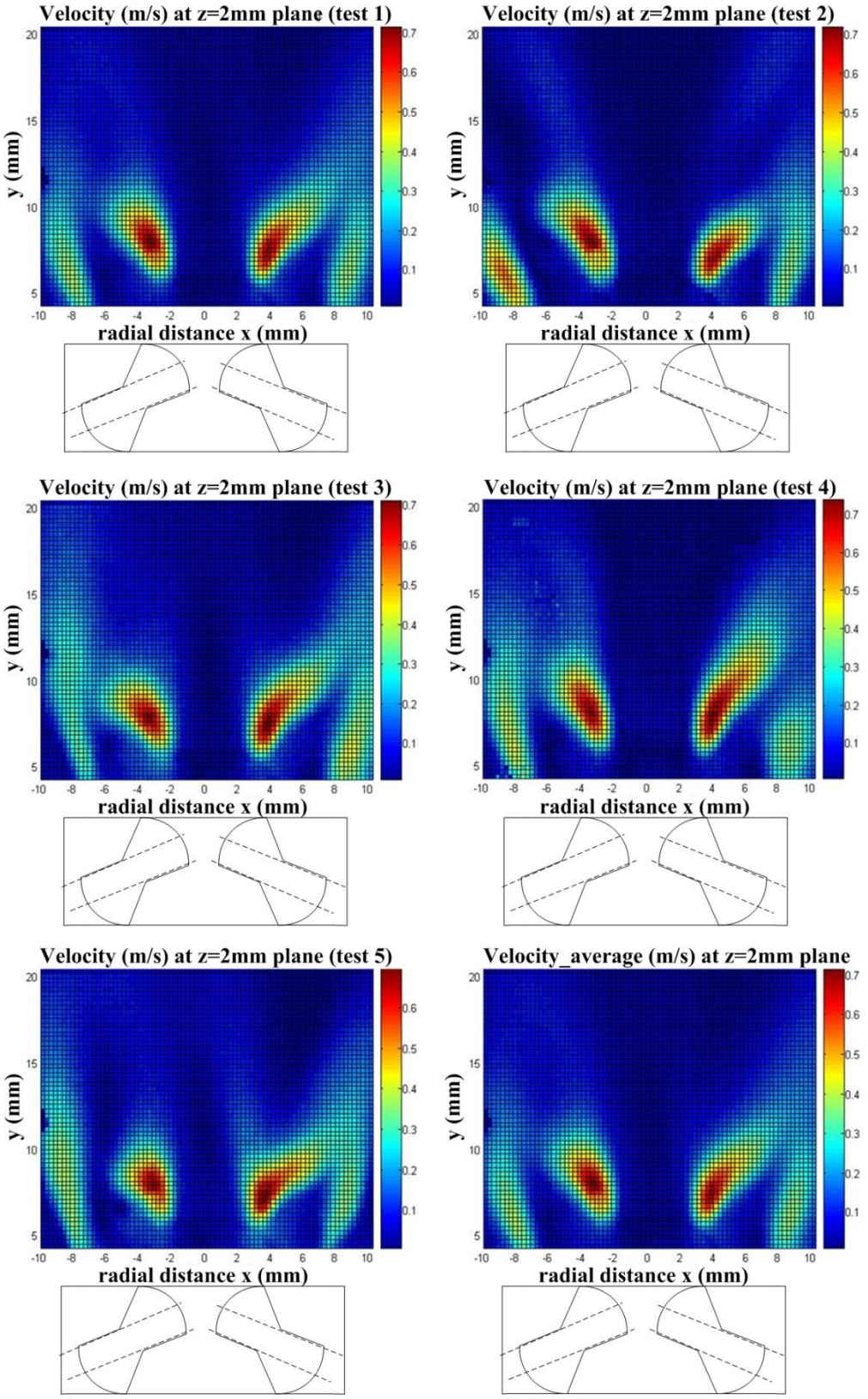

A 1.2.2 VELOCITY PROFILES AT DIFFERENT DOWNSTREAM LOCATIONS

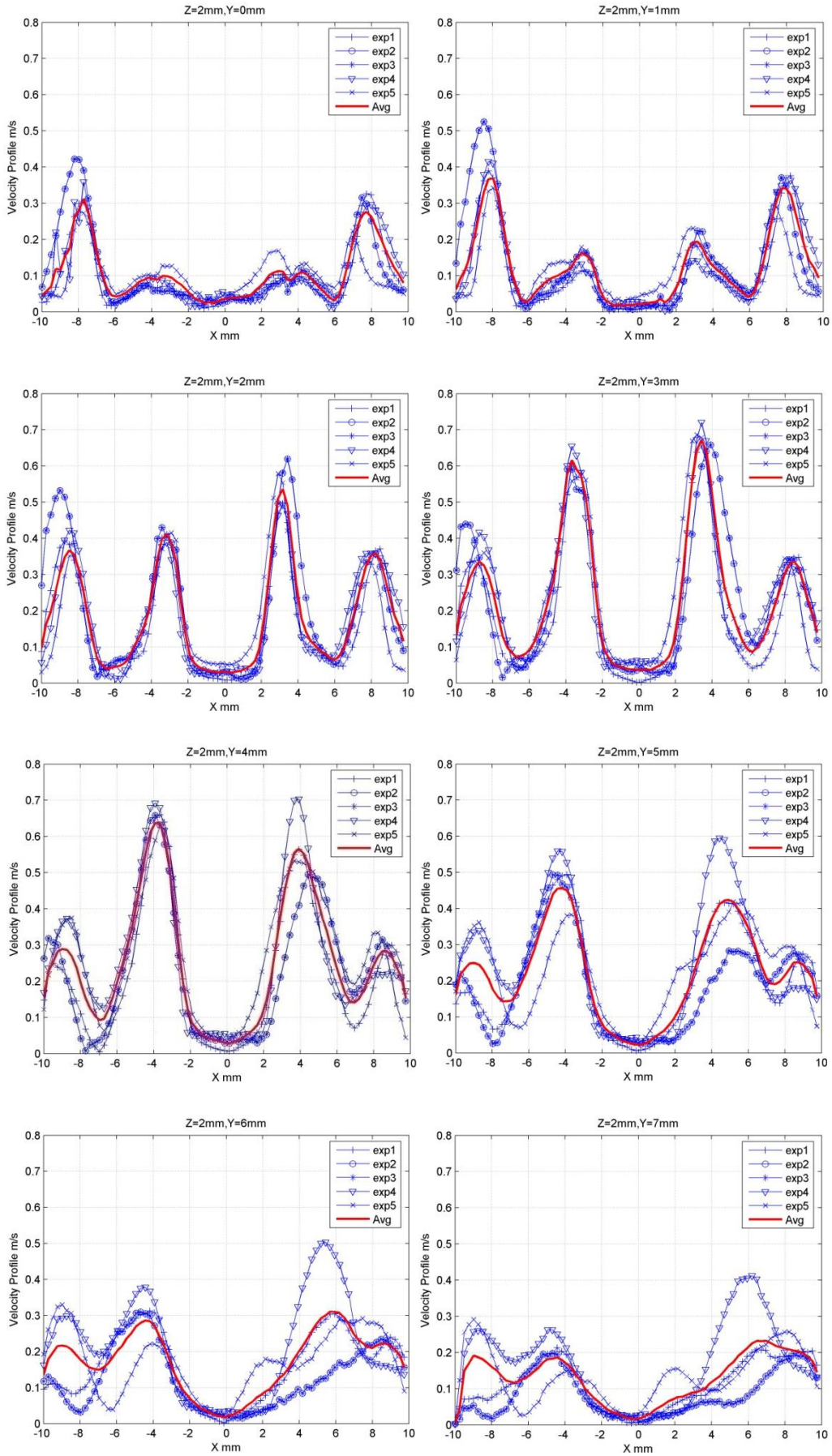

A 1.2.3 TSS DISTRIBUTION

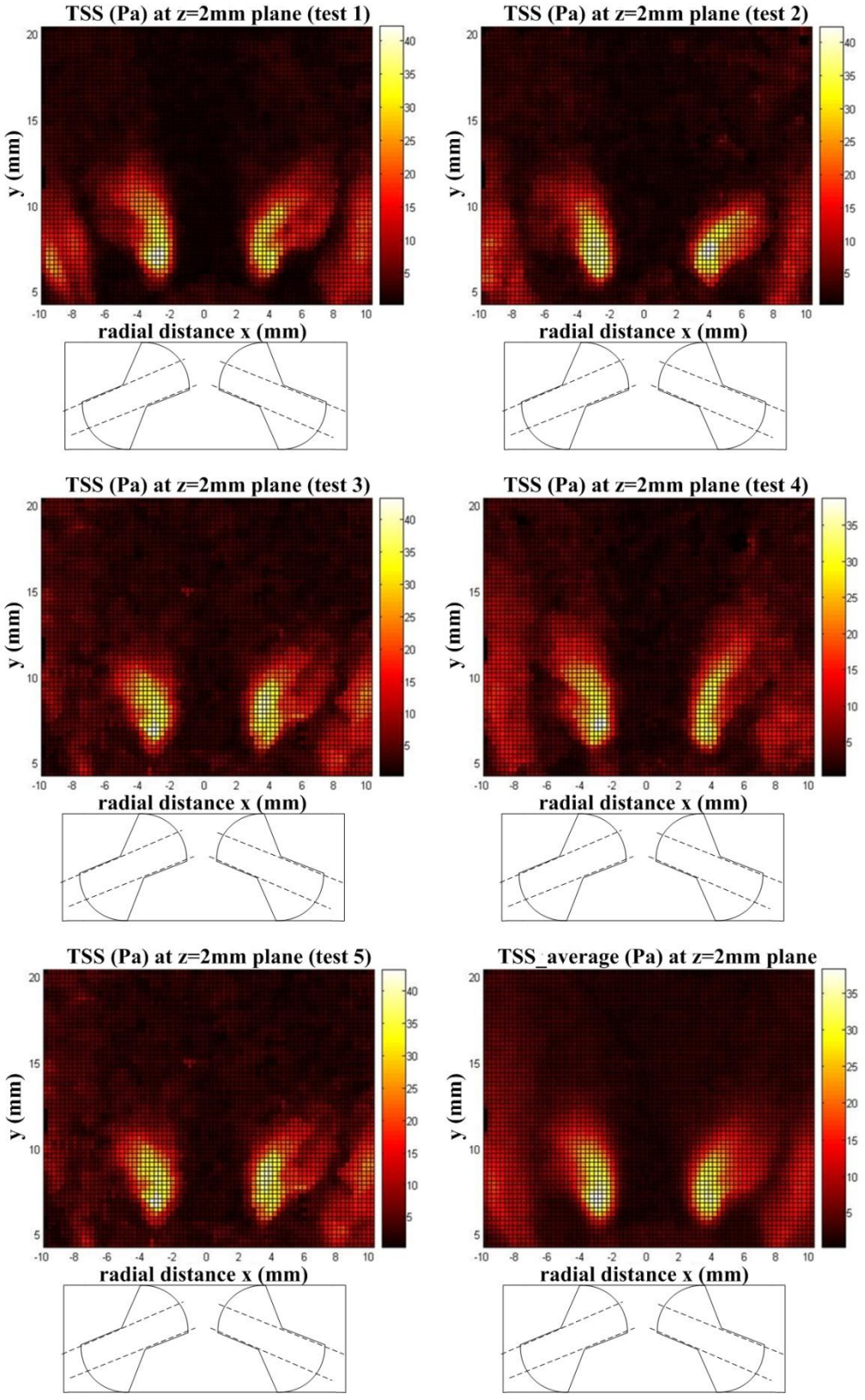

A 1.3 MULTIPLE EXPERIMENTAL RESULTS ON PLANE Z=3MM

A 1.3.1 VELOCITY DISTRIBUTION

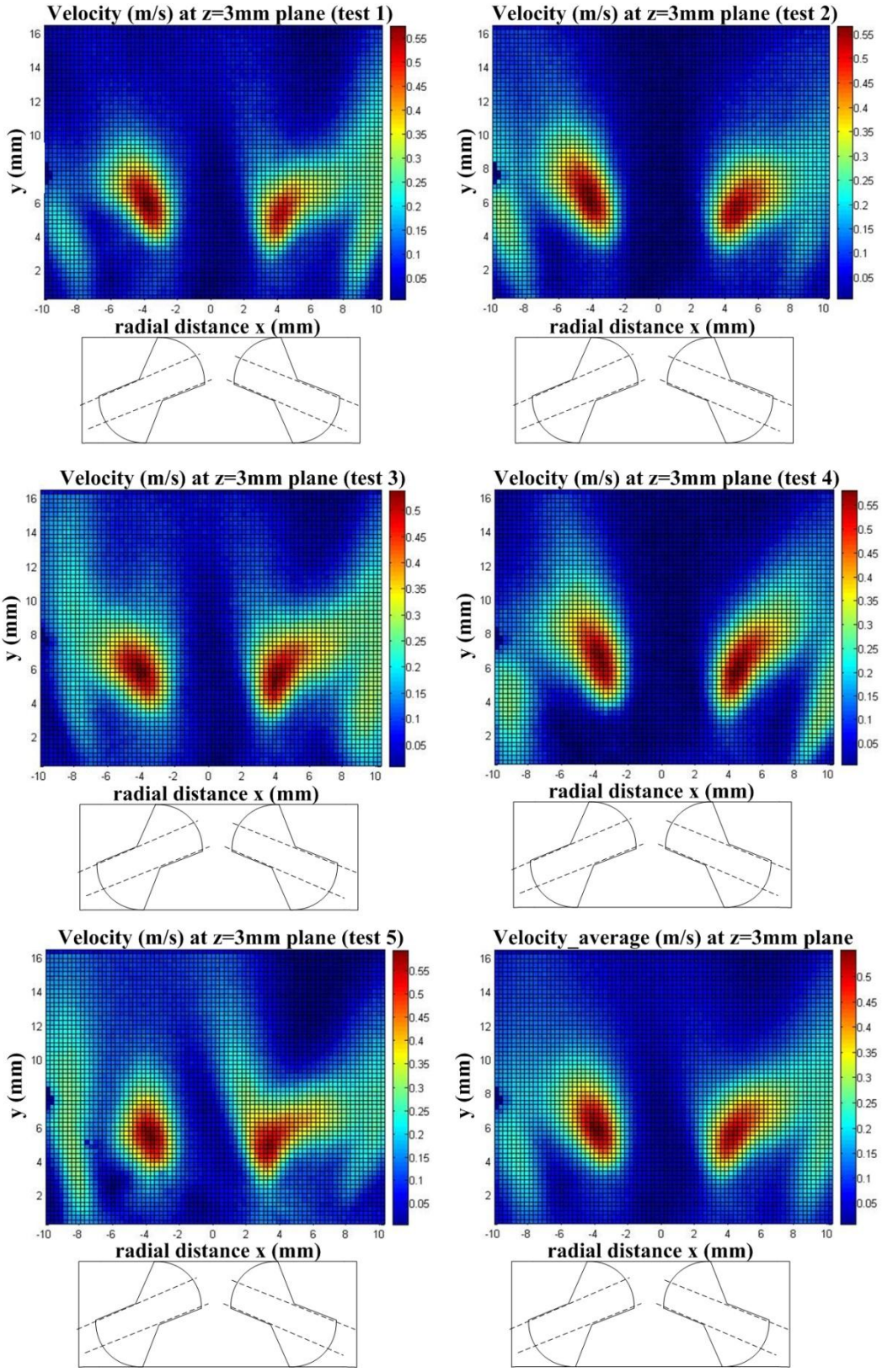

A 1.3.2 VELOCITY PROFILES AT DIFFERENT DOWNSTREAM LOCATIONS

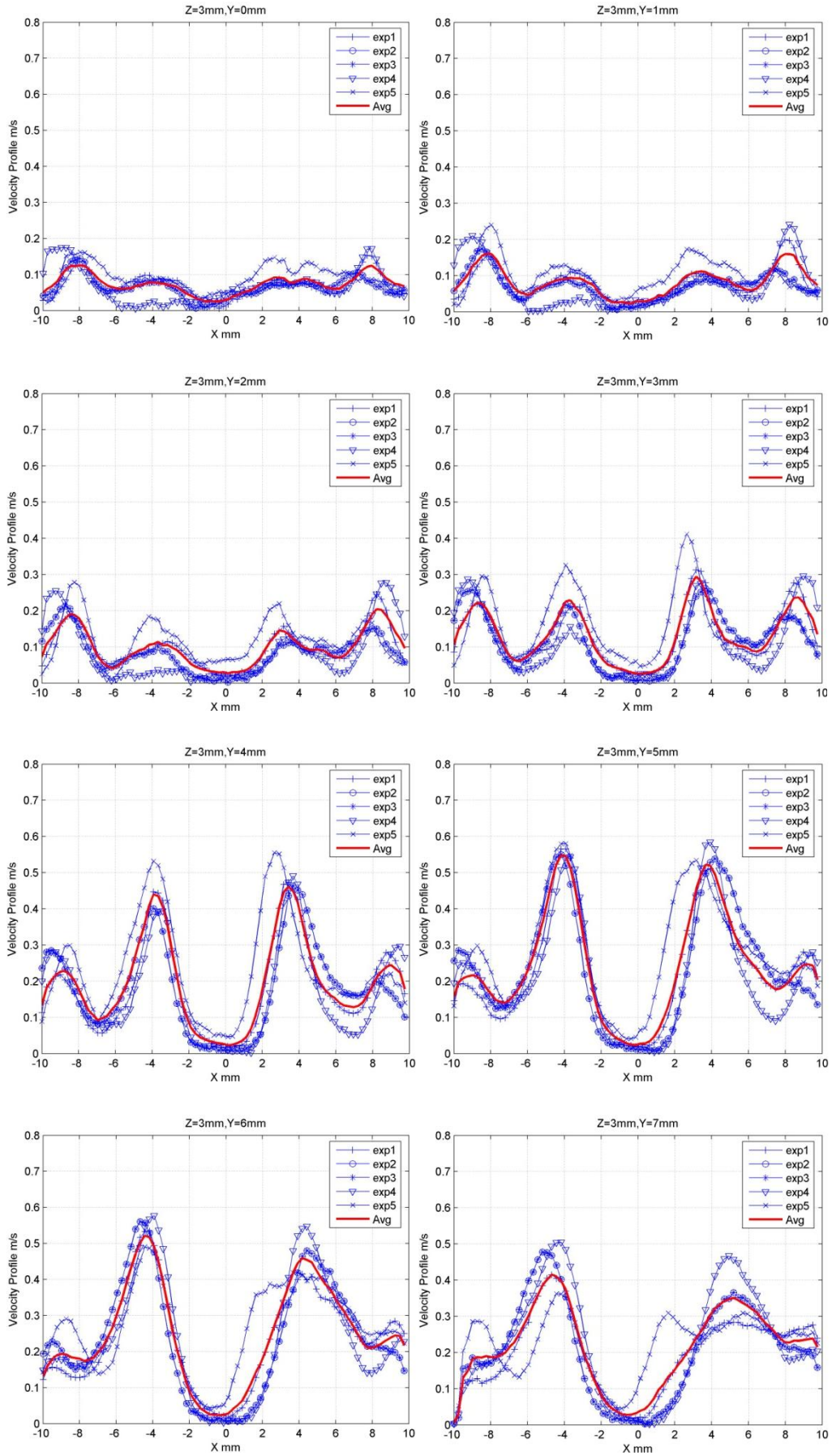

A 1.3.3 TSS DISTRIBUTION

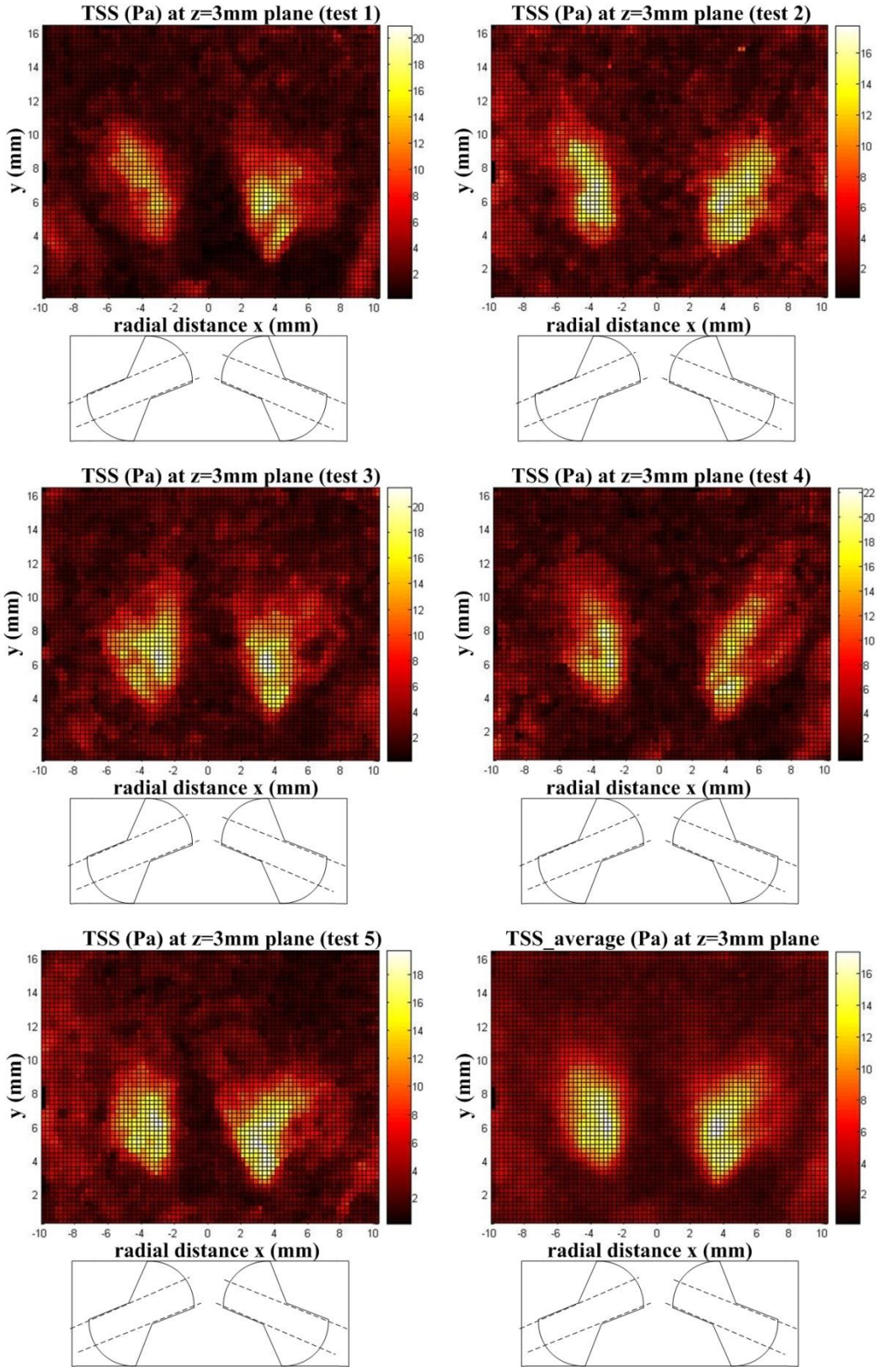

A 1.4 MULTIPLE EXPERIMENTAL RESULTS ON PLANE Z=4MM

A1.4.1 VELOCITY DISTRIBUTION

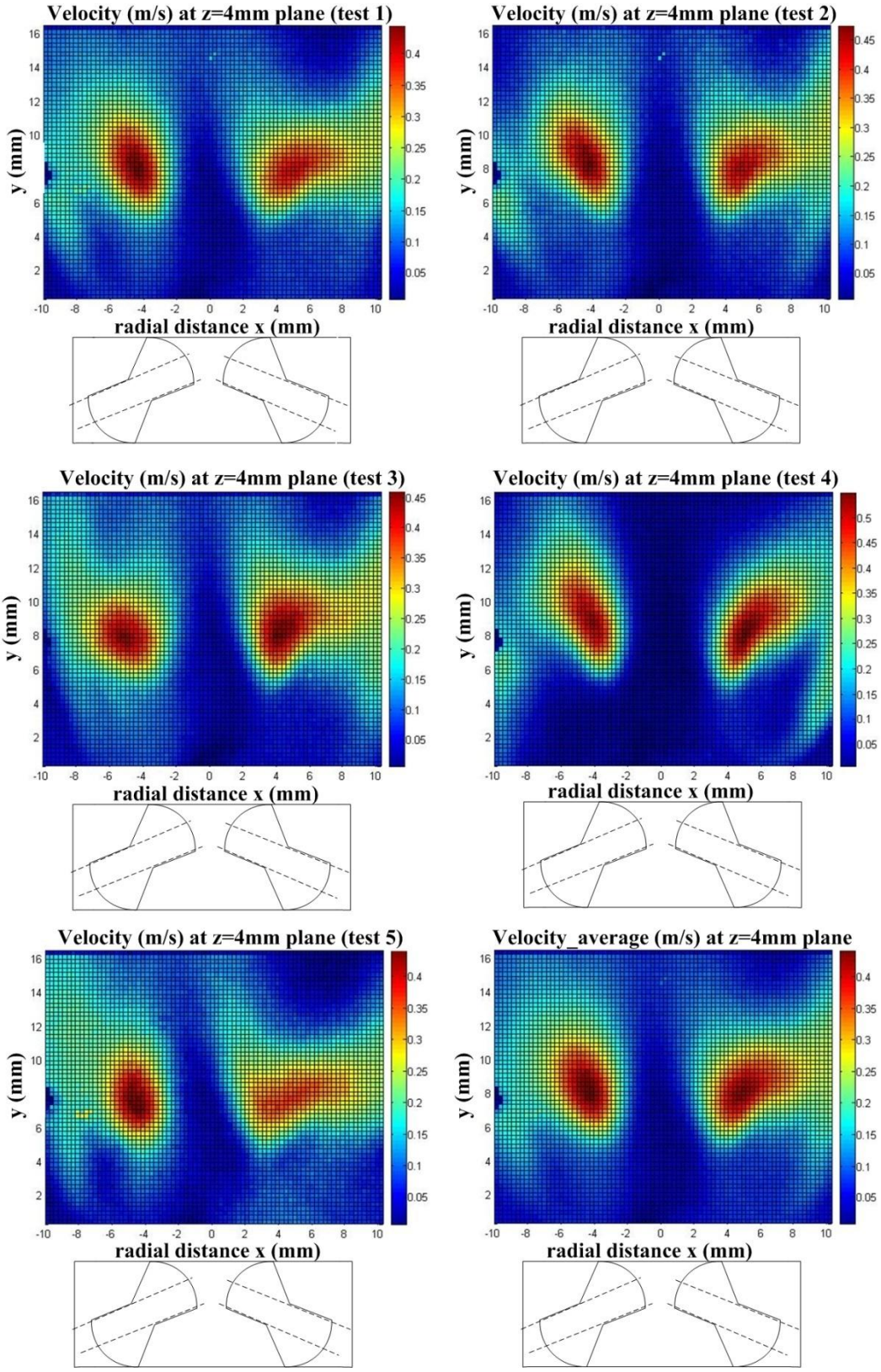

A 1.4.2 VELOCITY PROFILES AT DIFFERENT DOWNSTREAM LOCATIONS

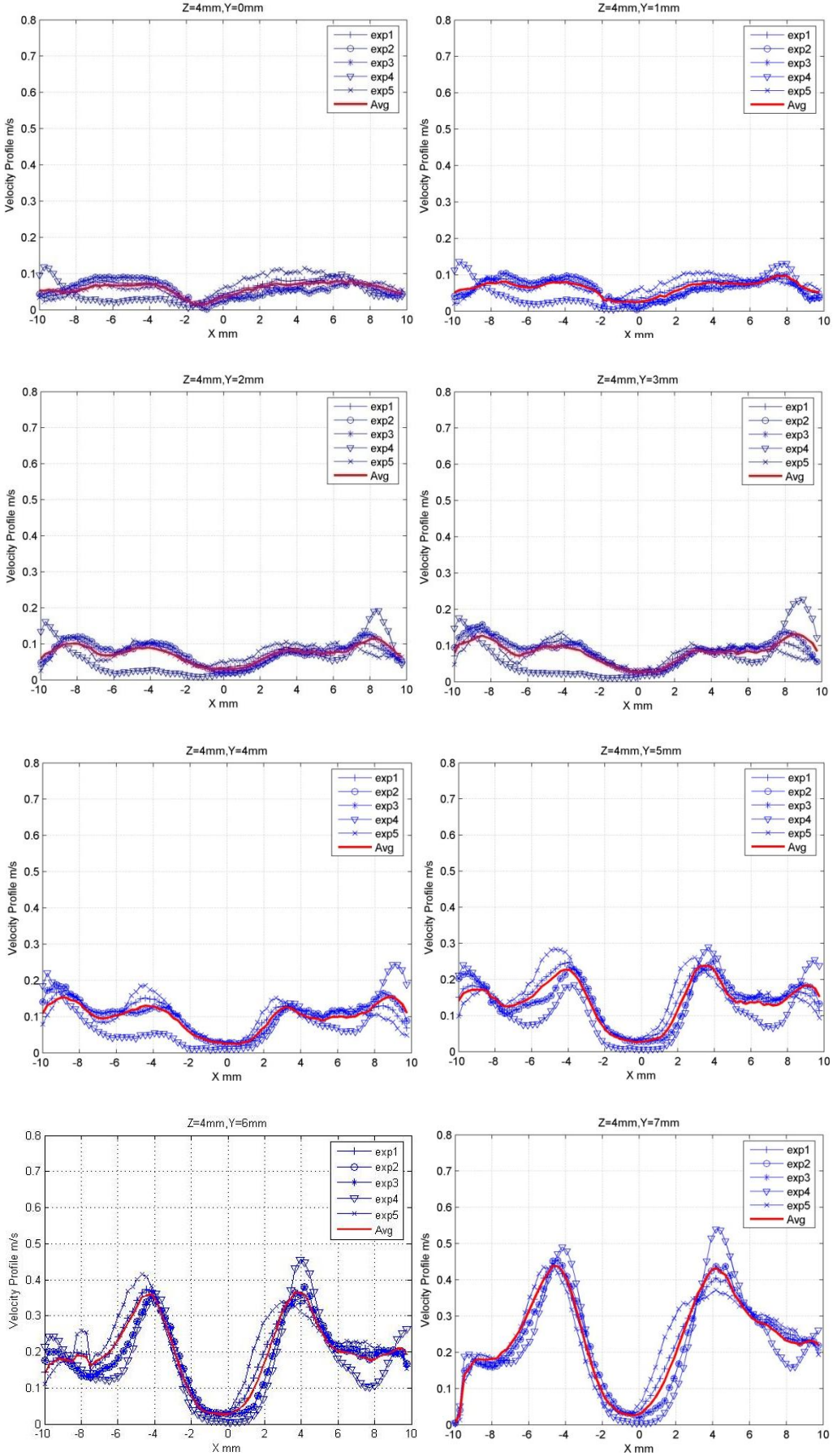

A 1.4.3 TSS DISTRIBUTION

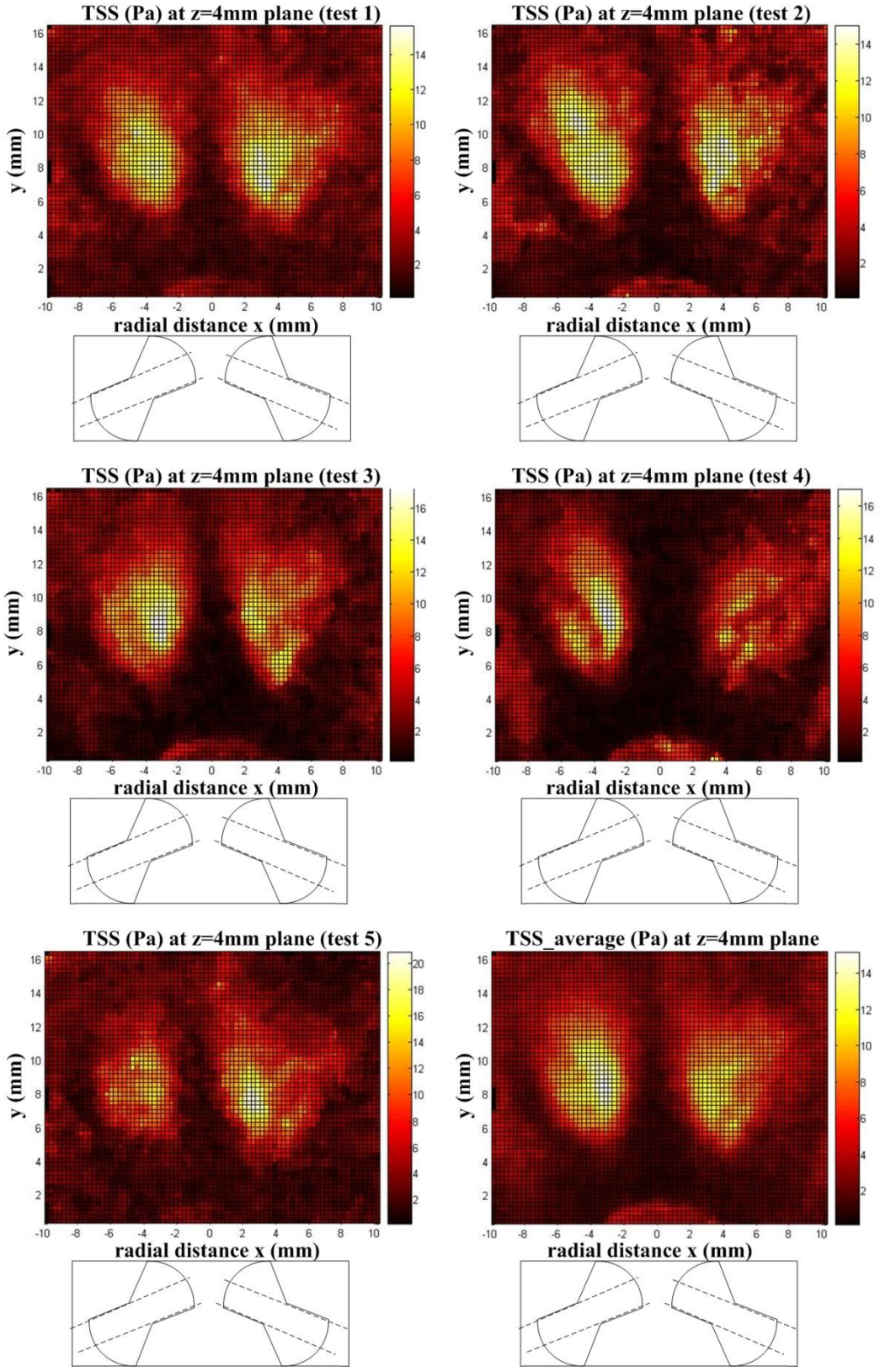

A 2. MULTIPLE EXPERIMENTAL RESULTS FOR VALVE TYPE 2
A 2.1 MULTIPLE EXPERIMENTAL RESULTS ON PLANE Z=2MM
A 2.1.1 VELOCITY DISTRIBUTION

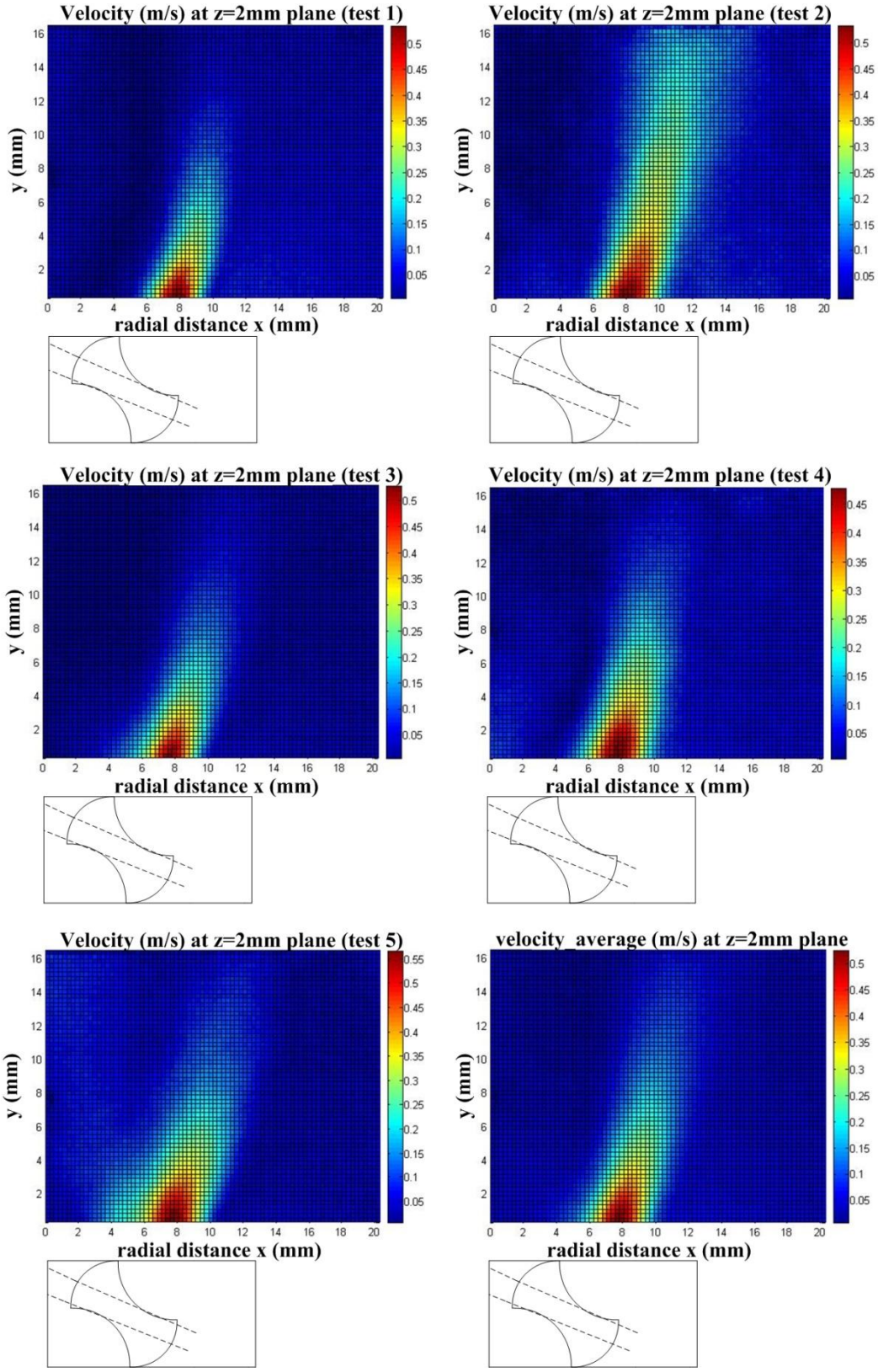

A 2.1.2 VELOCITY PROFILES AT DIFFERENT DOWNSTREAM LOCATIONS

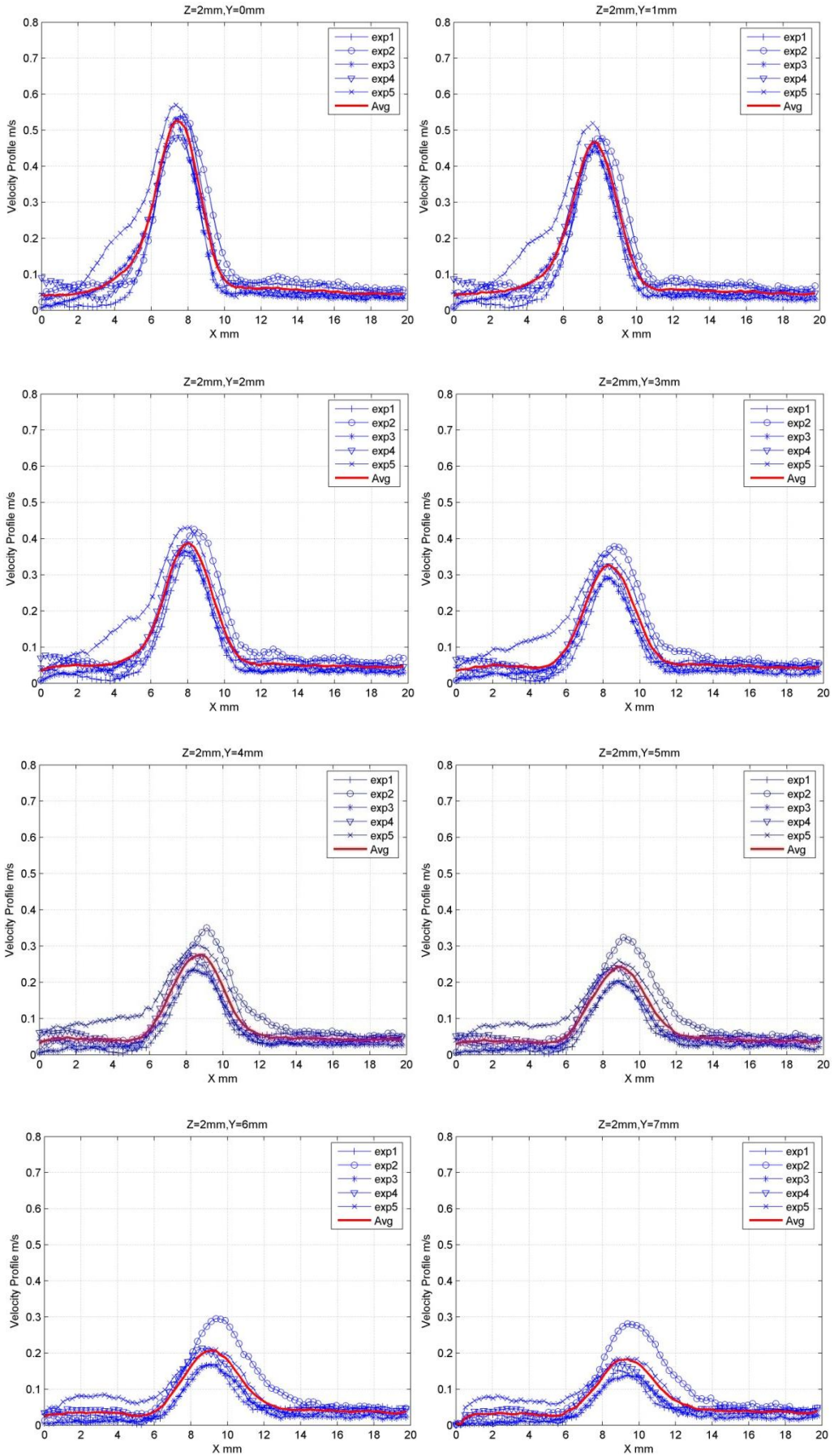

A 2.1.3 TSS DISTRIBUTION

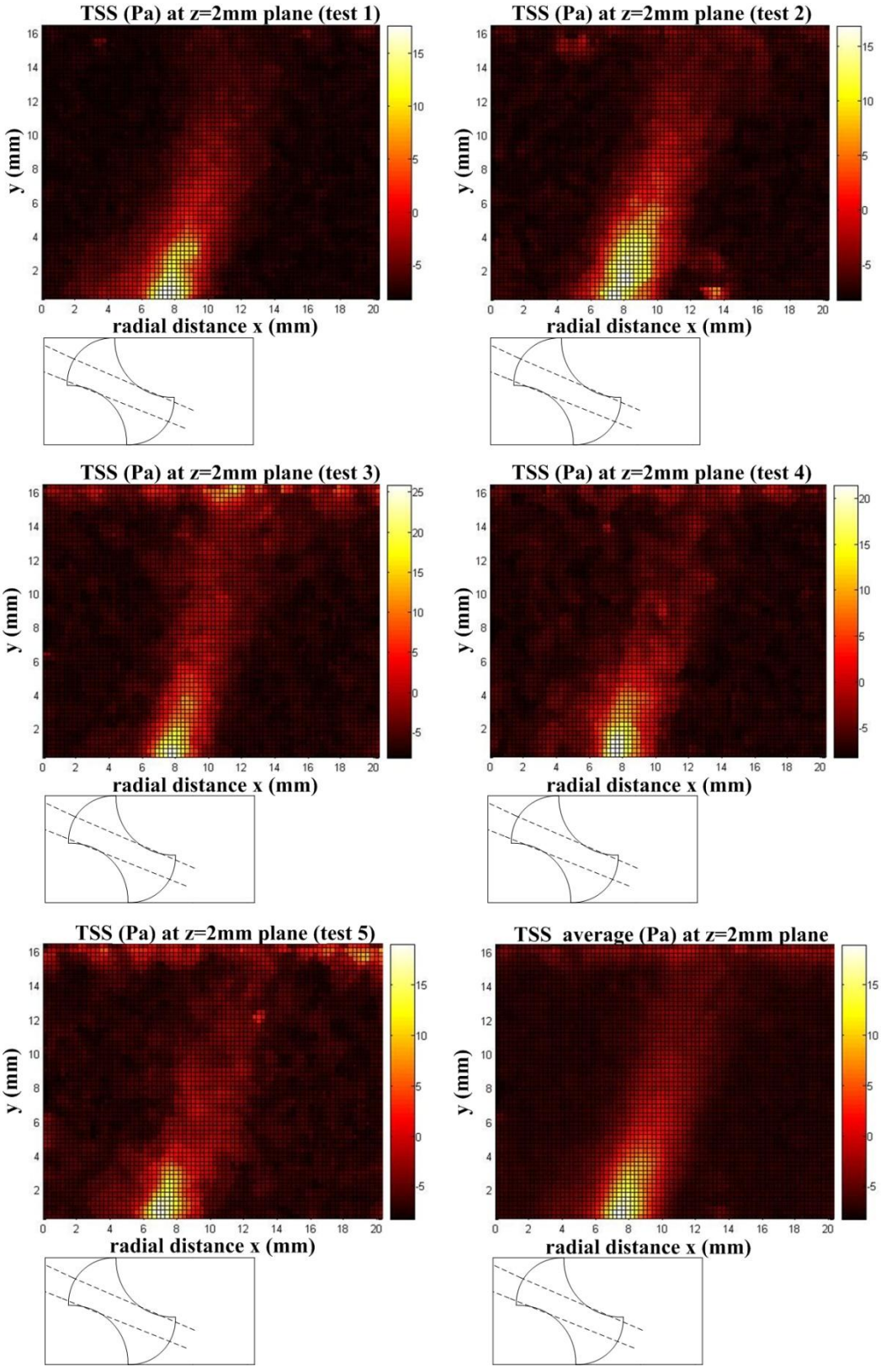

A 2.2 MULTIPLE EXPERIMENTAL RESULTS ON PLANE Z=3MM

A 2.2.1 VELOCITY DISTRIBUTION

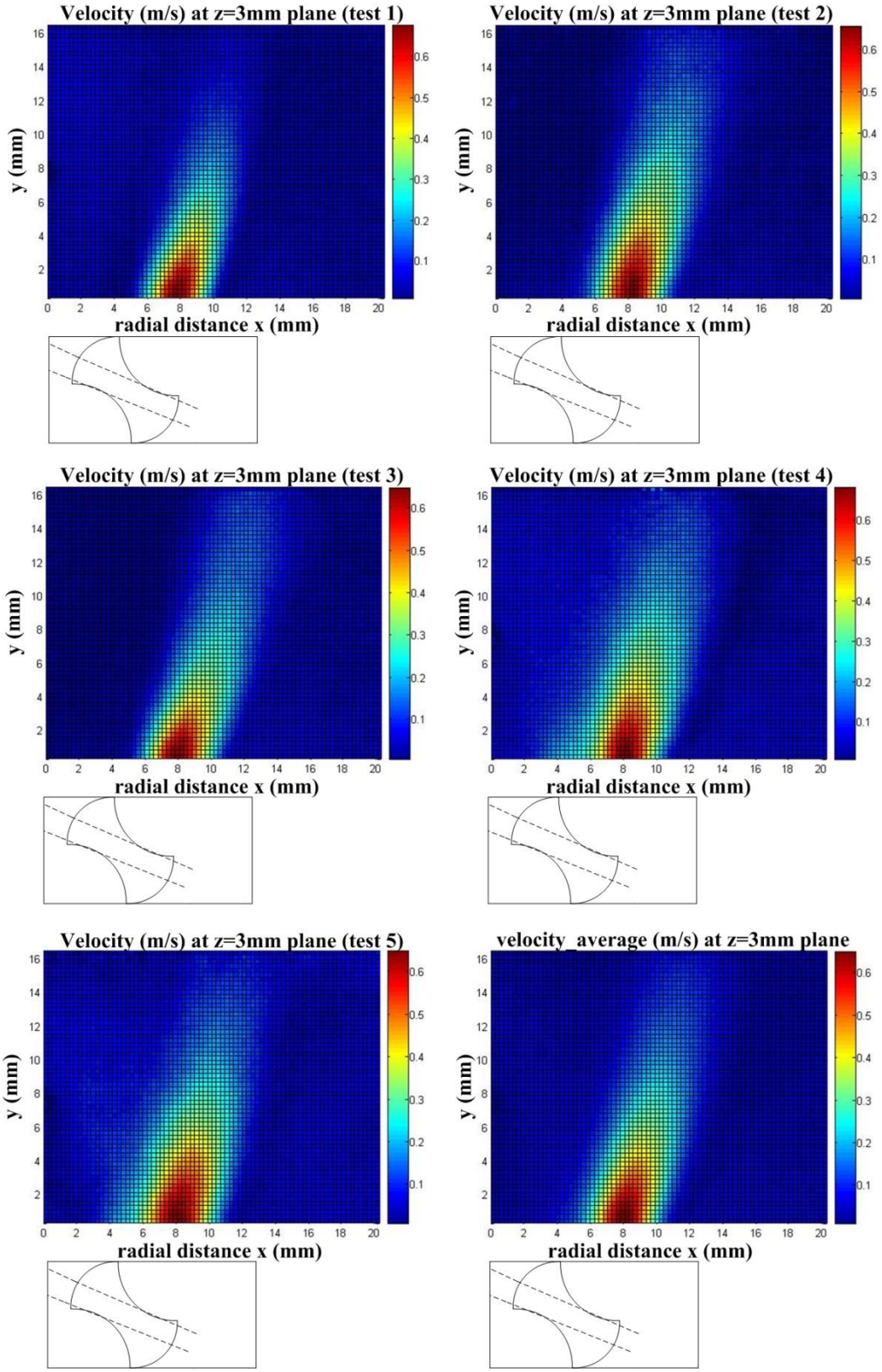

A 2.2.2 VELOCITY PROFILES AT DIFFERENT DOWNSTREAM LOCATIONS

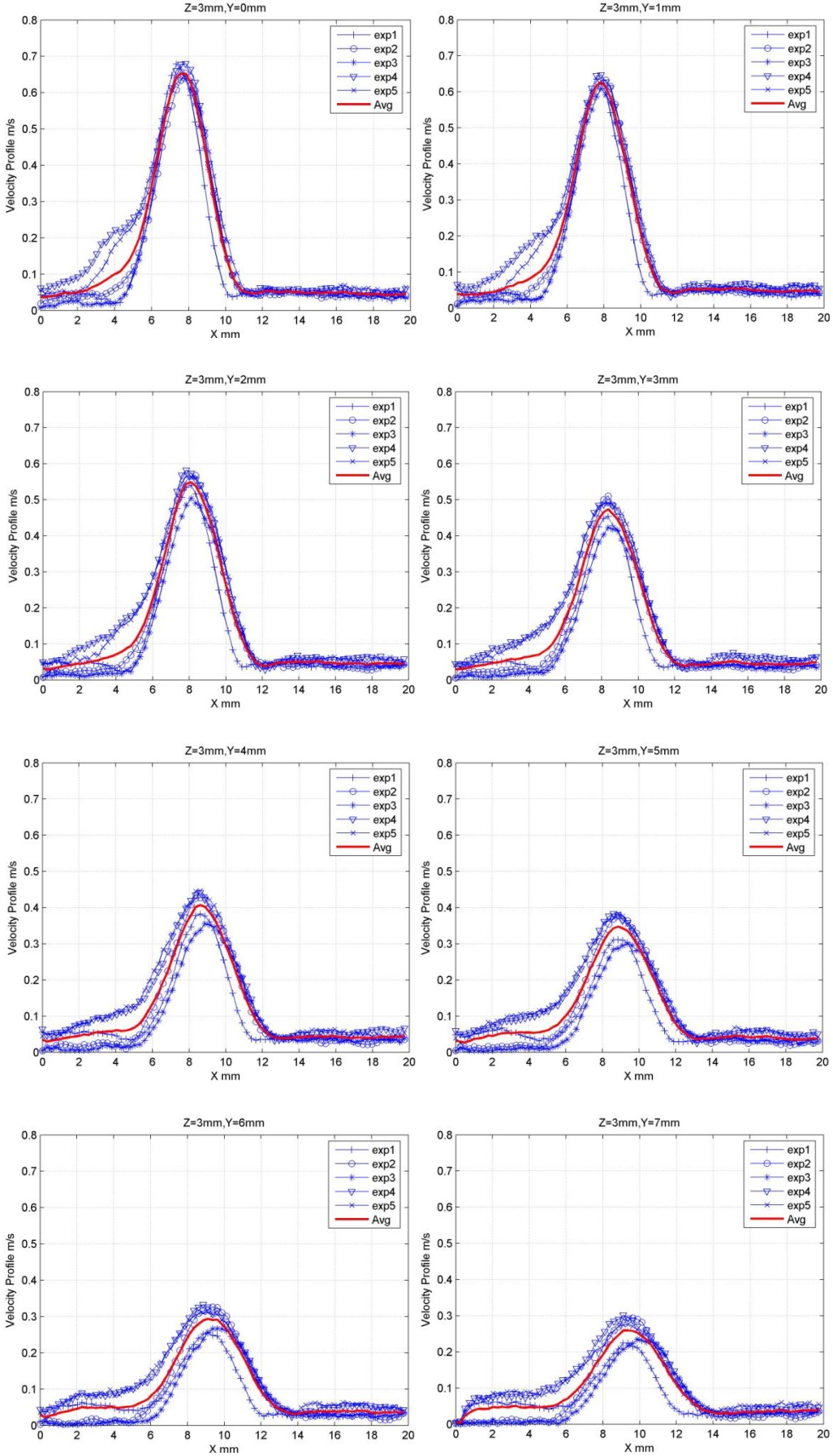

A 2.2.3 TSS DISTRIBUTION

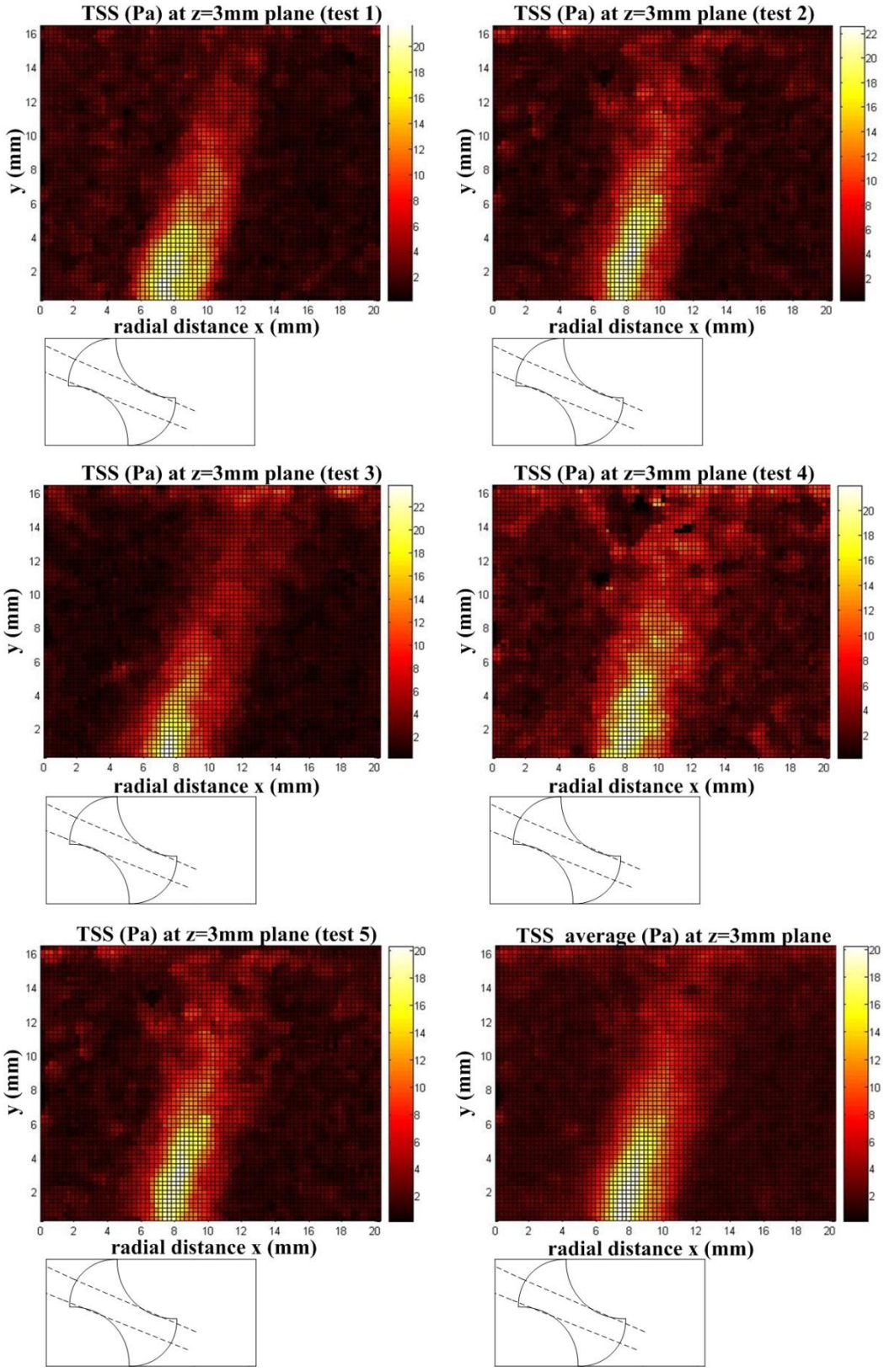

A 2.3 MULTIPLE EXPERIMENTAL RESULTS ON PLANE Z=4MM
A 2.3.1 VELOCITY DISTRIBUTION

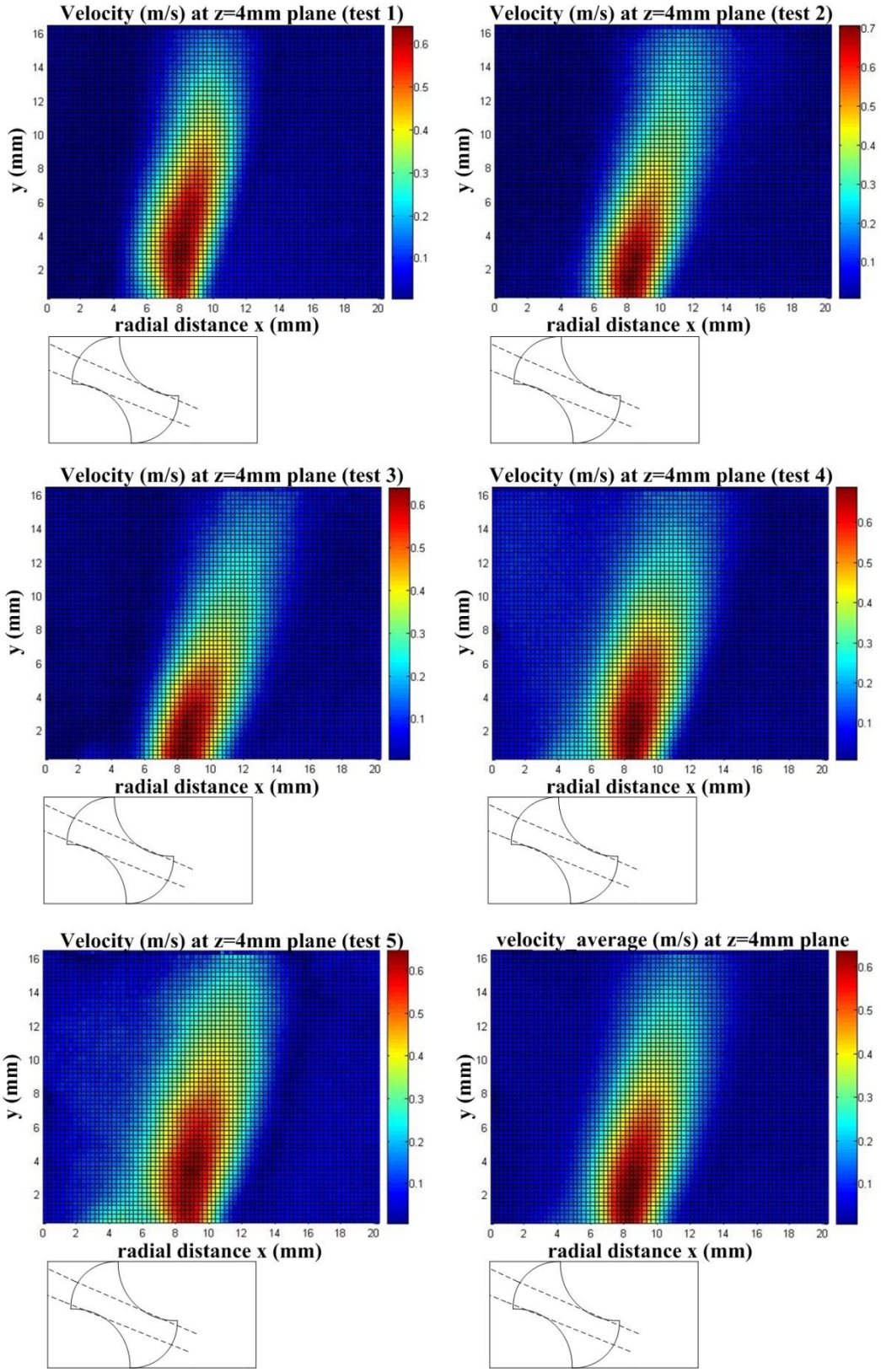

A 2.3.2 VELOCITY PROFILES AT DIFFERENT DOWNSTREAM LOCATIONS

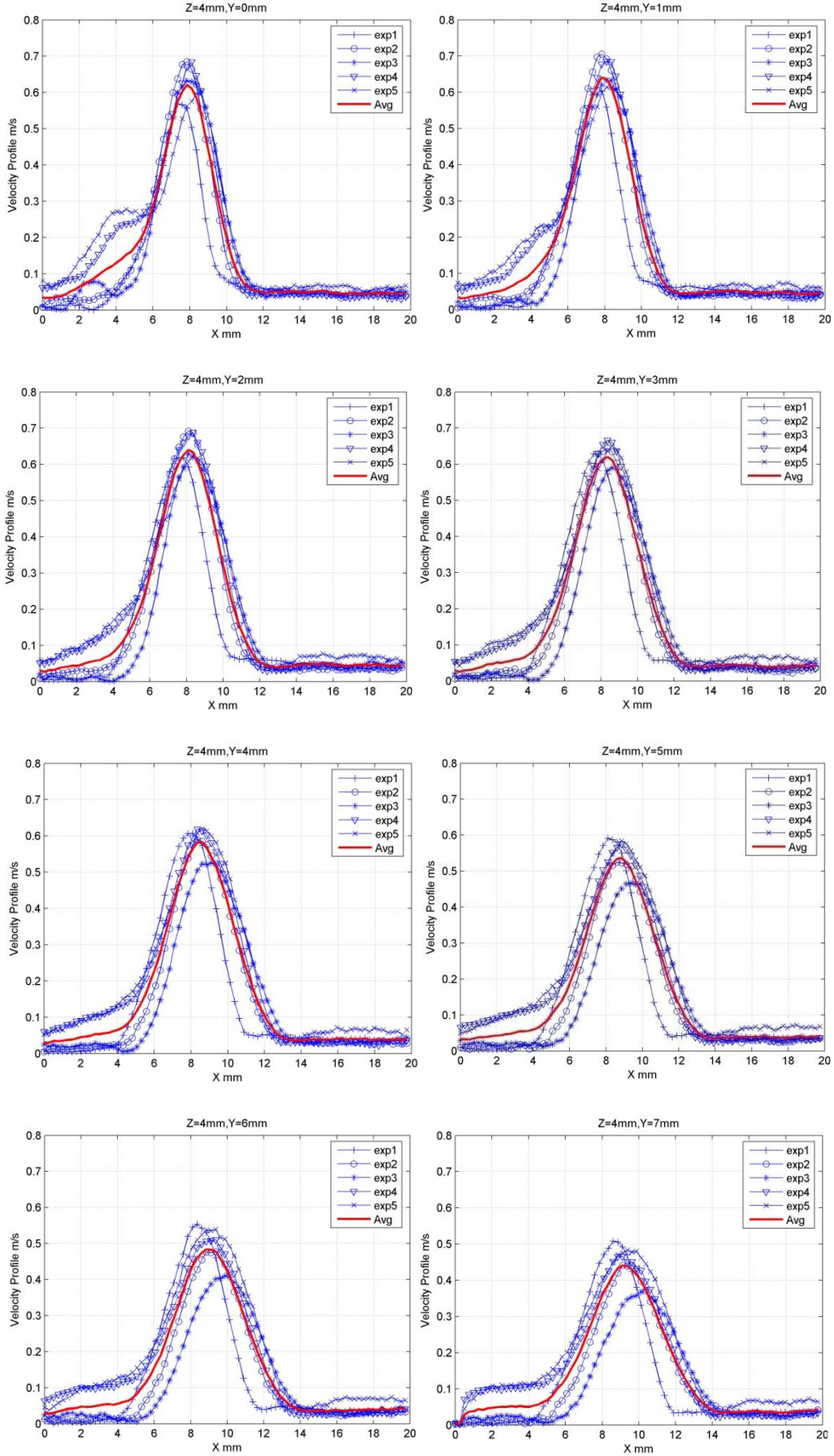

A 2.3.3 TSS DISTRIBUTION

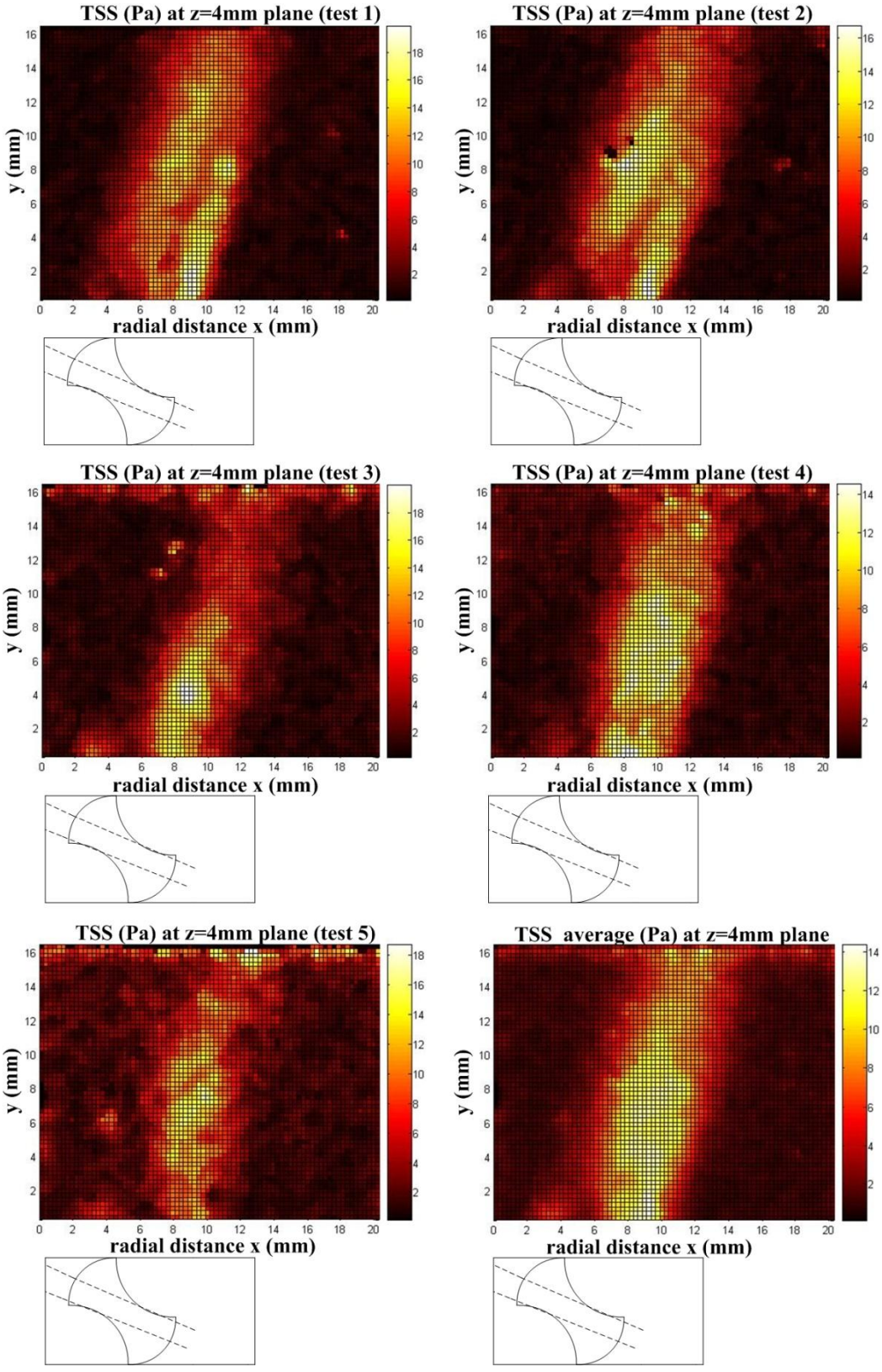

A 2.4 MULTIPLE EXPERIMENTAL RESULTS ON PLANE Z=5MM

A 2.4.1 VELOCITY DISTRIBUTION

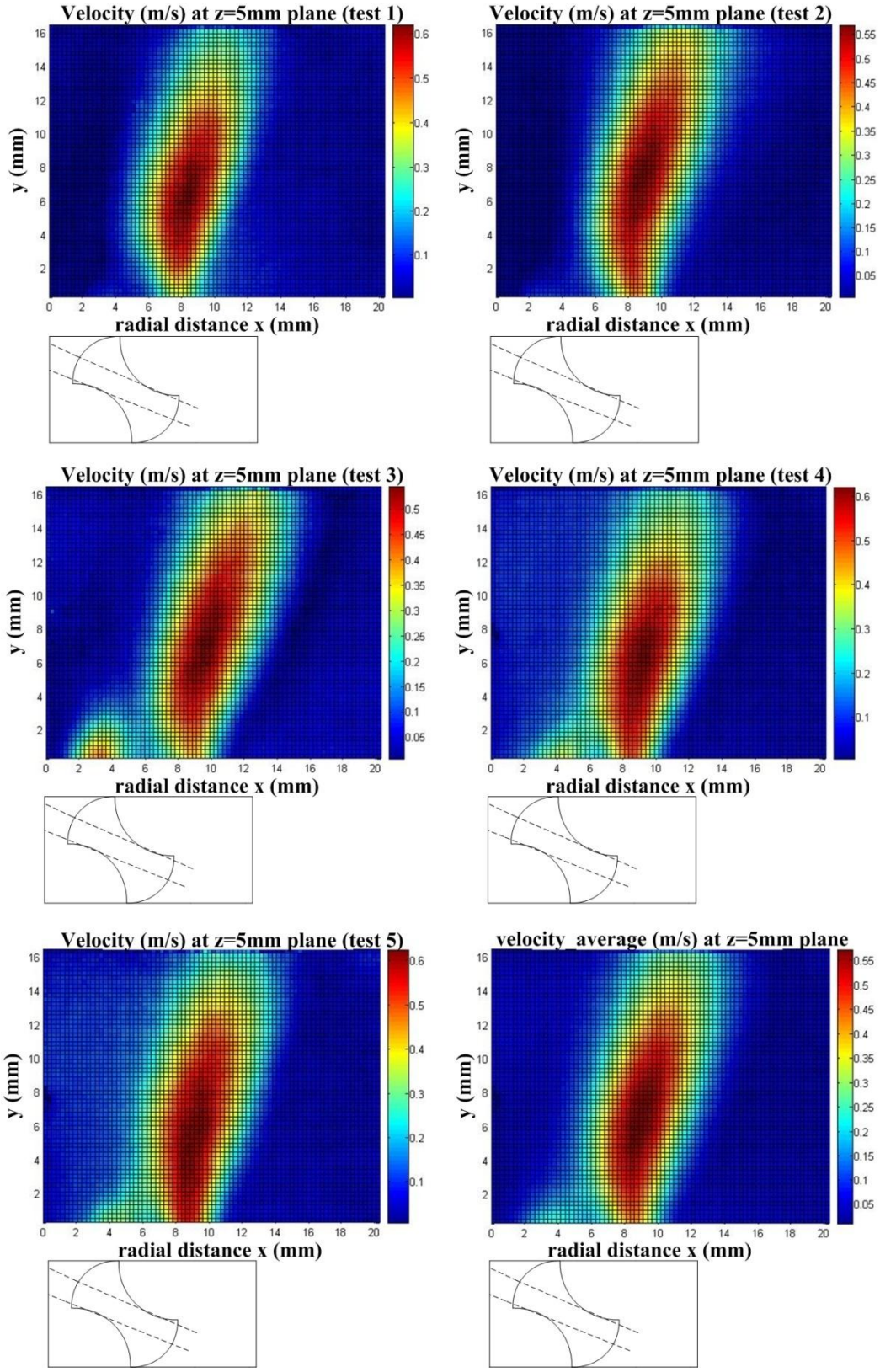

A 2.4.2 VELOCITY PROFILES AT DIFFERENT DOWNSTREAM LOCATIONS

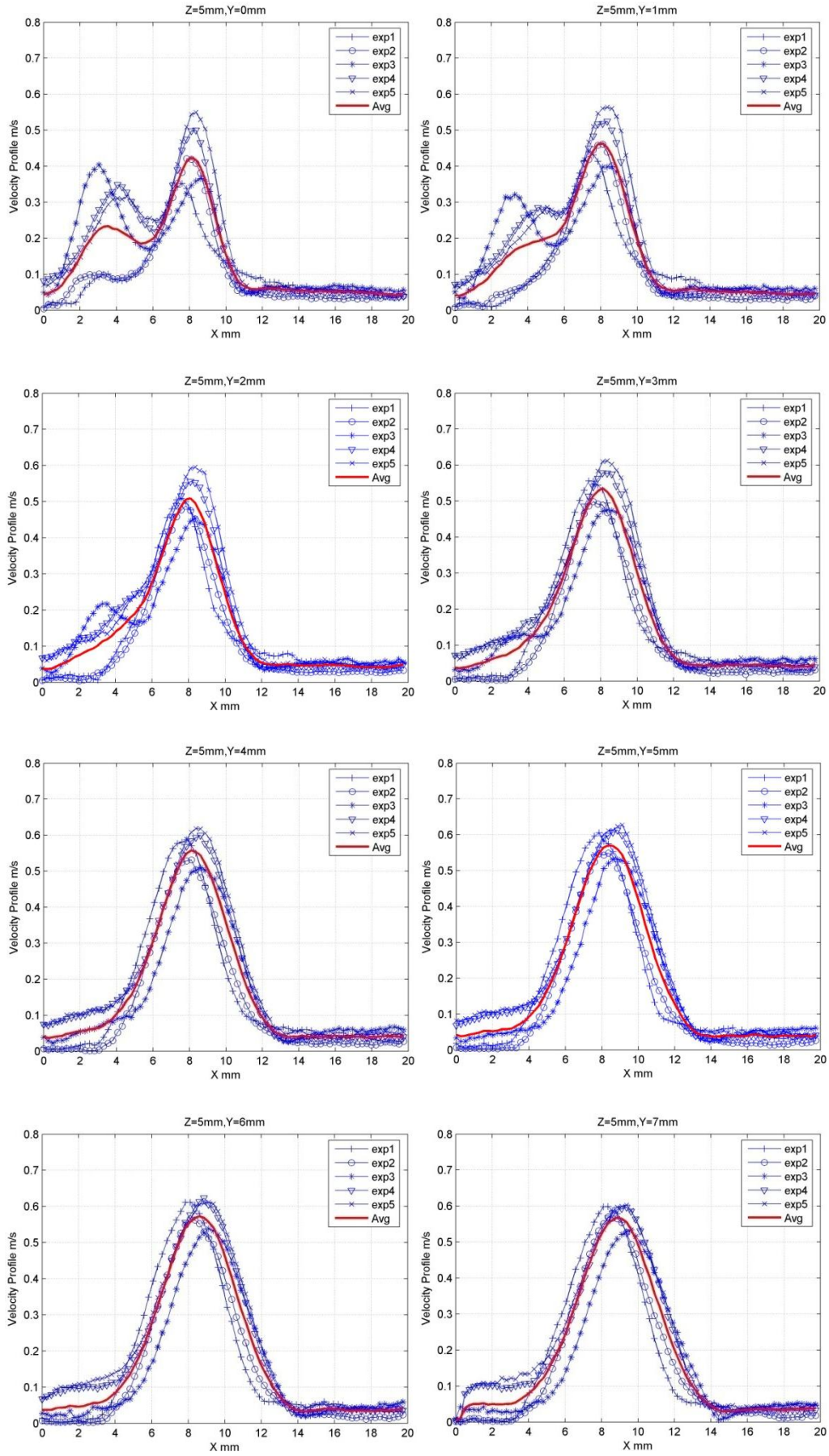

A 2.4.3 TSS DISTRIBUTION